HadGEM1 – Model description and analysis of preliminary experiments for the IPCC Fourth Assessment Report

Hadley Centre technical note 55

Tim Johns, Chris Durman, Helene Banks, Malcolm Roberts, Alison McLaren, Jeff Ridley Catherine Senior, Keith Williams, Andy Jones, Ann Keen, Graham Rickard, Stephen Cusack, Manoj Joshi, Mark Ringer, Buwen Dong, Hilary Spencer, Richard Hill, Jonathan Gregory, Anne Pardaens, Jason Lowe, Alejandro Bodas-Salcedo, Sheila Stark, Yvonne Searl

5 October 2004 (updated 23 February 2005)

Met Office

HadGEM1 – Model description and analysis of preliminary experiments for the IPCC Fourth Assessment Report

Tim Johns[1], Chris Durman[1], Helene Banks[1], Malcolm Roberts[1], Alison McLaren[1], Jeff Ridley[1], Catherine Senior[1], Keith Williams[1], Andy Jones[1], Ann Keen[1], Graham Rickard[3], Stephen Cusack[1], Manoj Joshi[1], Mark Ringer[1], Buwen Dong[1], Hilary Spencer[2], Richard Hill[1], Jonathan Gregory[1], Anne Pardaens[1], Jason Lowe[1], Alejandro Bodas-Salcedo[1], Sheila Stark[1], Yvonne Searl[1]

[1] Met Office, FitzRoy Road, Exeter EX1 3PB, UK
[2] CGAM, University of Reading, Earley Gate, Reading, UK
[3] NIWA, Wellington, New Zealand

Hadley Centre Technical Note No. 55

5 October 2004 (updated 23 February 2005)

Abstract

HadGEM1 is a new coupled climate model developed at the Met Office's Hadley Centre. It represents a significant advance on HadCM3 in terms of its science and provides an enhanced capability for carrying out new climate experiments. HadGEM1 also provides a foundation for further modelling advances across a range of applications, particularly involving enhanced resolution and full Earth System modelling. In this technical note we describe the main features of the HadGEM1 model design, outlining its component dynamics and physics and highlighting differences in its formulation and performance compared with HadCM3. The model can be run in three main configurations, namely: HadGAM1 - atmosphere-only with specified ocean surface boundary conditions; HadGSM1 - HadGAM1 interactively coupled to a simple mixed layer slab ocean; and HadGEM1 – HadGAM1 coupled to the full ocean model HadGOM1. The latter two configurations incorporate a similar sea ice component, considerably more advanced than that used in HadCM3, which we document in some detail. We present key results from a first set of experiments using the above configurations which are designed to address scientific problems of interest to the Intergovernmental Panel on Climate Change Fourth Assessment Report (IPCC AR4) and the EU ENSEMBLES project. HadGEM1 simulates the mean global climate more accurately than HadCM3 (also aspects of atmospheric variability, as shown in an accompanying paper), although there are also some deficiencies, particularly in the representation of the tropical climate and related phenomena including El Nino variability which are the subject of further work. Early indications are that HadGEM1's climate sensitivity (its mean surface global warming under a doubling of atmospheric CO_2) will be about 4.3 K, a somewhat higher sensitivity than HadCM3 displayed in an equivalent equilibrium slab experiment. However when both HadGEM1 and HadCM3 are run in idealised forcing experiments in which CO_2 increases at 1% per year, both the rate of surface global mean climate warming and its geographical pattern are quite similar apart from a reduced land-sea contrast in HadGEM1. On the other hand, the respective patterns of anomalous heat uptake by the ocean and the response of the global thermohaline circulation show some significant differences that are also the subject of further study.

Contents

1 Introduction

HadGEM1 is the latest in a series of climate models developed at the Hadley Centre. It incorporates major scientific changes to the atmosphere and the sea ice components relative to HadCM3 (Pope et al. 2000, Gordon et al., 2000), but fewer changes have been made to the ocean component of the model. The name HadGEM1 stands for "Hadley Centre Global Environmental Model version 1", which is intended to indicate that the model will (in time) encompass other components of the environmental system other than just the physical climate.

In planning the timescale for development of HadGEM1, which started in 2000, delivering initial results for the IPCC AR4 was seen as the initial goal. This technical note is a milestone towards that goal.

In this note, we first describe the overall design philosophy for the model and the methodology by which it was developed and tuned. Next we provide an outline technical description of the model components. It is beyond the scope of this paper to provide a full scientific description – the reader is referred to other papers for more details. We then present some analysis from, and discuss, HadGEM1's control simulation, focussing on evaluation in comparison to climatological fields and to HadCM3. We examine timeseries from the control simulation of the model paying particular attention to the adjustments of the ocean towards a steady state, examine its ability to simulate both the mean climate and other phenomena of interest, and summarise the model's overall skill using a quasi-objective method. We also present results from some idealised sensitivity experiments with both a slab ocean version of the model (HadGSM1), and with HadGEM1 itself. We conclude with a brief summary and outline some future developments and applications of HadGEM1.

2 HadGEM1 model design objectives, development strategy, and cost

The key strategic objective behind the development of HadGEM1 was to build a replacement for the aging HadCM3 model (Gordon et al. 2000; Pope et al. 2000), and in particular to move to a new atmospheric dynamical core ("New Dynamics" or ND - Davies et al. 2004) that was then expected to become (and has now become) part of the Met Office Numerical Weather Prediction (NWP) model. This would then facilitate continuance of the Unified Model (UM) strategy for NWP and climate modelling at the Met Office. HadGEM1 was also designed from the outset to be a candidate for a community climate model for the whole UK with the ability to be developed further towards a full Earth System modelling capability – that is, coupling of physical climate with chemistry and ecosystem subcomponents. The scientific development strategy utilised established (project and team-based) model development methods, drawing on scientific expertise within the Met Office and via some external contracts, with a target objective of delivering higher resolution and greater experimental flexibility in HadGEM1 while achieving a better scientific performance than HadCM3. For the first time, quasi-objective methods of measuring model performance were employed alongside subjective assessment.

A starting point for constructing a HadGEM1 prototype was the physical and technical improvements developed in two intermediate models, specifically the atmospheric component HadAM4 (Webb et al. 2003) and the coupled model HadCEM (Roberts et al. 2004). However, the atmospheric physics improvements in HadAM4 were developed in the context of HadCM3's old dynamical core, so putting the atmospheric component of

HadGEM1 together using ND necessitated large changes amounting almost to starting from a completely new atmosphere model.

HadCM3 became operational towards the end of 1997, so projecting a normal rate of increase in computer power (doubling every 18 months) up until 2003/04 (the target timetable for operational delivery of HadGEM1) suggested that a model of approximately 15-20 times the cost of HadCM3 would be affordable at that time. This was factored into the design to allowing something like a 6-8 times cost increase from higher resolution, with a further 2-3 times from additional physical complexity.

Since HadOM3, the ocean component of HadCM3 (Gordon et al., 2000) was developed (with a horizontal resolution of 1.25° in both latitude and longitude), there had been experimentation with higher resolution ocean components (for example, Roberts et al. 2004 included a 1/3° resolution ocean component in HadCM3 - the model referred to as HadCEM). One of the most significant differences between HadCM3 and HadCEM was the timescale for the spinup of the ocean (Roberts et al., 2004); HadCM3 took nearly 400 years for ocean and atmosphere freshwater budgets to balance in the Atlantic while HadCEM took less than 100 years. The ocean design changes in HadGEM1 were much more modest than for the atmosphere component, being a compromise between the pull towards higher resolution and the practical constraints on the computer time available to develop the model. It was decided to keep the basic resolution of the ocean component of HadGEM1 close to HadCM3 at ~1° rather than the higher resolution in HadCEM (see section 3.2 for more details) and it is therefore of considerable interest to understand whether HadGEM1's behaviour is closer to HadCM3 or HadCEM.

In the event, the standard HadGEM1 N96L38 atmosphere model resolution has ended up with 8 times as many grid points as HadCM3 (2x2x2 in latitude, longitude and vertical dimensions), while the ocean has a lesser increase in grid points compared to HadCM3 by a factor of 3.75 (1.5x1.25x2 in latitude, longitude and depth). Both the atmosphere and ocean timesteps are unaltered however, so this amounts to a cost increase of around 6 times due to resolution factors alone (consistent with the original plans). Other changes and additions to the model physics and dynamics in turn account for an additional cost factor of about 2-2.5 times, giving an overall cost factor of 12-15x for HadGEM1 compared to HadCM3. Note however that the relative computational cost of these models in practice is highly dependent on their implementation and optimisation on a given computer.

In view of the substantial changes, the prototype HadGEM1 model required a lot of methodical improvement and tuning before it could meet a similar standard of performance to HadCM3. Starting from the prototype model, configured in both atmosphere and coupled modes, scientific performance problems were tackled initially by focussed expert teams ("Tiger Teams"), typically working in parallel over a period of a year and running and analysing sensitivity tests to arrive at improvements which were consolidated into later generations of the prototype model. In the early stages, as much common ground as possible was sought between climate and NWP applications of the model in identifying and understanding the performance problems. Once the main problems had been rectified by this means sufficiently to allow the NWP model to become operational with ND, some identifiable issues remained for HadGEM1 which required further team-based work to achieve the necessary improvements. The final stage of development was to tune the model by means of further refinements to the schemes and parameter-based tuning in order to optimise the skill of the model (a mixture of objective measures and subjective consensus), such that any imbalances and implied drifts in the coupled model were within an acceptable tolerance.

3 Description of the HadGEM1 model and initial experiments

3.1 HadGAM1 - Atmospheric model description

HadGAM1, the atmospheric component of HadGEM1, is markedly different from the predecessor model HadAM3, probably the most significant difference being the move to New Dynamics ("ND" - Davies et al. 2004).

The advances offered by ND to the climate model include: a non-hydrostatic, fully compressible, deep atmosphere formulation with fewer approximations to the basic equations; semi-Lagrangian advection of all prognostic variables except density, permitting relatively long timesteps to be used at high resolution; a conservative and monotone treatment of tracer transport; better geostrophic adjustment properties bringing better balance (and reduced timestep dependence) to the coupling with physical parametrizations, which now calculate increments in parallel based on balanced states rather than in sequence. Importantly, ND brings the capability to run at much higher resolution in future without the need for further major revisions to the dynamics itself.

Another key advance in HadGAM1 is the inclusion of the interactive modelling of atmospheric aerosols, driven by surface and elevated emissions (from both natural and anthropogenic sources) and including tropospheric chemical processes as well as physical removal processes such as washout. This scheme is coupled on each timestep to the atmospheric model dynamics and physics, including radiation, cloud microphysics, precipitation and boundary layer, the aerosol species represented being sulphate, black carbon, biomass smoke, and sea salt. (Mineral dust is not yet modelled, but such a scheme is under development.) Modelling atmospheric aerosols removes the need for a climatological aerosol representation which was included in HadCM3. It also permits modelling of the direct and indirect effects of the aerosol species represented, these being important potential forcings (and major sources of modelling uncertainty) under climate change.

In the standard configuration of HadGAM1 used in the work presented here, the atmosphere grid has a horizontal resolution of 1.25^{o} x 1.875^{o} in latitude and longitude with 38 layers in the vertical extending to over 39 km in height, as given in Table 1 (see Davies et al. 2004 for the definition of the hybrid height coordinate system). We refer to this resolution as N96L38 for shorthand.

The many other underlying differences in the physical parametrizations in HadGAM1 compared to HadAM3 are beyond the scope of this paper to document. Table 2, adapted from Martin et al. (2004), summarises the main differences, references therein giving more details.

Layer boundary (n)	Hybrid "eta" coordinate	Hybrid height (m)
38 (lid)	1.0	39254.8
37	.8383348	32908.7
36	.7443435	29219.1
35	.6772068	26583.6
34	.6230643	24458.3
33	.5763897	22626.1
32	.5347160	20990.2
31	.4968308	19503.0
30	.4620737	18138.6
29	.4298913	16875.3
28	.3998142	15694.6
27	.3714396	14580.8
26	.3444162	13520.0
25	.3184321	12500.0
24	.2934670	11520.0
23	.2695209	10580.0
22	.2465938	9680.0
21	.2246857	8820.0
20	.2037966	8000.0
19	.1839264	7220.0
18	.1650752	6480.0
17	.1472430	5780.0
16	.1304298	5120.0
15	.1146356	4500.0
14	.0998603	3920.0
13	.0861040	3380.0
12	.0733668	2880.0
11	.0616485	2420.0
10	.0509491	2000.0
9	.0412688	1620.0
8	.0326074	1280.0
7	.0249651	980.0
6	.0183417	720.0
5	.0127373	500.0
4	.0081519	320.0
3	.0045854	180.0
2	.0020380	80.0
1	.0005095	20.0
0 (surface)	0.0	0.0

Table 1: Vertical levels in the standard HadGAM1 N96L38 configuration. The hybrid height represents the true height above a surface at mean sea level. Layer boundary heights depend on surface orographic height up to n=29, but are at constant real height above this.

	HadAM3	HadGAM1
Atmospheric grid	Arakawa-B grid	Arakawa-C grid
Hydrostatic	Yes	no
Vertical resolution (atmosphere)	19 levels; hybrid pressure; Lorenz grid	38 levels; hybrid height; terrain-following near bottom boundary; Charney-Phillips grid
Physics-dynamics coupling	Sequential	Parallel-split (slow processes), sequential-split (fast processes). (Dubal et al., 2004)
Dynamics	Eulerian advection, split-explicit time integration (Cullen 1993)	Semi-Lagrangian advection, conservative monotone treatment of tracers; semi-implicit time integration (Staniforth et al., 2003, Davies et al., 2004)
Radiation	Edwards and Slingo (1996); Cusack et al. (1999a)	Edwards and Slingo (1996); Cusack et al. (1999a)
Boundary layer	Local Richardson number mixing scheme (Smith 1990,1993)	Non-local mixing scheme for unstable BLs (Lock et al. 2000). Local Richardson number scheme for stable layers (Smith 1990, 1993)
Microphysics	Senior and Mitchell (1993); evaporation of precipitation as in Gregory (1995).	Wilson and Ballard (1999)
Convection	Mass flux scheme (Gregory and Rowntree,1990); convective downdraughts (Gregory and Allen, 1991); convective momentum transport (Gregory et al., 1997)	Revised scheme including diagnosed deep and shallow convection; new thermodynamic closures at lifting condensation level; new CMT parametrisation based on flux-gradient relationships; parametrised entrainment /detrainment rates for shallow convection. Based on ideas in Grant and Brown (1999), Grant (2001); Convective anvil scheme (Gregory, 1999)
Gravity wave drag	Gregory et al. (1998)	GWD scheme with low-level flow blocking Webster et al. (2003)
Orography	Derived from US Navy 10' dataset	Derived from GLOBE dataset at 1' resolution
Hydrology	MOSES-I (Cox et al., 1999)	MOSES-II (Essery et al., 2001); 9 surface tile types plus coastal tiling; seasonally-varying vegetation (Lawrence and Slingo, 2004)
Clouds	Smith (1990); prescribed critical relative humidity for cloud formation (RH-crit)	Smith (1990); parametrised RH-crit (Cusack et al., 1999b); vertical gradient area cloud scheme (Smith et al., 1999)
River routing	Simple basin aggregate output instantaneously to ocean	Embedded 1x1 degree river transport/ hydrology sub-model (Oki and Sud, 1998)
Aerosols	prescribed	Interactive; sulphate, black carbon, biomass-burning and sea-salt aerosol schemes; direct/indirect radiative forcing (Jones et al., 2001; Roberts and Jones, 2004; Jones and Roberts 2004; Woodage et al., 2003)

Table 2: Summary of HadAM3 and HadGAM1 configurations. (After Martin et al. 2004)

3.2 HadGOM1 – Ocean model description

The ocean component (HadGOM1) of the HadGEM1 coupled climate model is based on the Bryan-Cox code (Bryan 1969; Cox 1984), and is a development of the ocean component of HadCM3 (Gordon et al. 2000). The model uses a latitude-longitude grid with a zonal resolution of 1°, and a meridional resolution of 1° between the poles and 30°, from which it increases smoothly to 1/3° at the equator, giving a grid of 360x216 points. It has 40 unevenly spaced levels in the vertical (see Table 3), with enhanced resolution near the surface better to resolve the mixed layer and thermocline.

Level	Depth (m)	Thickness (m)	Level	Depth (m)	Thickness (m)
1	5.0	10.0	21	398.60	80.8
2	15.0	10.0	22	488.25	98.5
3	25.0	10.0	23	596.40	117.8
4	35.0	10.0	24	724.50	138.4
5	45.0	10.0	25	873.85	160.3
6	55.0	10.0	26	1045.60	183.2
7	65.0	10.0	27	1240.70	207.0
8	75.0	10.0	28	1459.90	231.4
9	85.0	10.0	29	1703.70	256.2
10	95.0	10.0	30	1972.40	281.2
11	105.0	10.0	31	2265.80	305.6
12	115.0	10.0	32	2581.75	326.3
13	125.0	10.0	33	2914.95	340.1
14	135.6	11.2	34	3257.50	345.0
15	148.5	14.6	35	3602.50	345.0
16	165.95	20.3	36	3947.5	345.0
17	190.25	28.3	37	4292.5	345.0
18	223.6	38.4	38	4637.5	345.0
19	268.1	50.6	39	4982.5	345.0
20	325.8	64.8	40	5327.5	345.0

Table 3: Depth and thickness of model levels (centred on tracer points)

The model uses an implicit linear free surface (Dukowicz and Smith 1994) to solve for the barotropic mode, using a conjugate gradient solver, and this scheme allows for a more realistic representation of freshwater fluxes than was possible with the rigid lid of HadCM3 (see UMDP62, Roberts and Rickard 2004, and Table 4 for parameter settings).

Scheme	Parameter	HadGEM1 value	HadCM3 value
Kraus-Turner mixed layer	wind mixing energy scaling factor	0.55	0.7
	decay of wind mixing energy with depth	100m	100m
	decay of conv. generated energy	0.15	0.15
Peters et al vertical mixing	background vert mix momentum	$2x10^{-5}$ m^2 s^{-1}	N/A
	vert mix momentum on Ri	$5.5x10^{-3}$ m^2 s^{-1}	N/A
	background vert mix tracer (surf)	$1x10^{-5}$ m^2 s^{-1}	N/A
	rate of increase with depth	$2.8x10^{-2}$ m^2 s^{-1}	N/A
	max vert mixing for stability	$1x10^{-2}$	N/A
Quadratic Large	critical Richardson number	0.3	N/A
	maximum depth for qlarge	80m	N/A
Free surface solver	max iterations	2000	N/A
	criterion for convergence	$1x10^{-2}$	N/A
	delplus/cross weighting	0.5	N/A
Momentum diffusion	Laplacian horiz	2000 m^2 s^{-1}	3000 + 3000 cos(lat) m^2 s^{-1}
	Biharmonic horiz	$1.0x10^{13}$ $\cos^3$ (lat) m^4 s^{-1}	N/A
Tracer diffusion	Isopycnal diffusion coeff	500 m^2 s^{-1}	1000 m^2 s^{-1}
	Biharmonic adiabatic coeff	$1.0x10^{12}$ $\cos^3$ (lat) m^4 s^{-1}	N/A
	Horiz biharmonic (levels 1-2)	$2.5x10^{12}\cos^3$ (lat) m^4 s^{-1}	N/A
	Visbeck minimum value	150 m^2 s^{-1}	350 m^2 s^{-1}
	Visbeck maximum value	2000 m^2 s^{-1}	2000 m^2 s^{-1}
	Visbeck inverse timescale crit	$3.5x10^{-6}$ s^{-1}	$1.4x10^{-6}$ s^{-1}
	Bottom friction	0.001	N/A
Penetrative solar absorption	ETA1	1.0 m^{-1}	1.0 m^{-1}
	ETA2	$5.9x10^{-2}$ m^{-1}	$5.9x10^{-2}$ m^{-1}
	RSOL	$3.8x10^{-1}$	0.0
Timestep related	Timestep	1 hour	1 hour
	Constant for time filtering	0.01	0.01
	Semi-implicit Coriolis term coefficient	0.75	0.75

Table 4: Summary list of values used in model parameterization schemes in HadGEM1 and HadCM3.

The mixed layer is represented by the Kraus and Turner (1967) bulk mixed layer for tracers, together with a quadratic approximation to the Large et al. (1994) scheme for momentum mixing in the mixed layer (see UMDP59, Rickard 2004). Vertical mixing beneath the mixed layer is performed by the Peters et al. (1988) scheme; this is a Richardson-number dependent scheme, and its parameters have been altered better to fit the observed data in their paper by Cusack (2004). This change reduces the excessive noise near the ocean surface. There is also a modification to the standard vertical mixing scheme to enhance the mixing at the base of the mixed layer, to increase the communication between the ocean surface and the deeper layers and make the profile more similar to that observed (Wu and Ineson, personal communication, 2003).

The Griffies et al. (1998) isopycnal scheme is included with a uniformly constant diffusion coefficient of 500 m^2s^{-1}. The Gent and McWilliams (1990) scheme is used in the skew-flux form, with a coefficient that varies horizontally in space and time according to a scheme based on Visbeck et al. (1997) as detailed in UMDP54 (Roberts 2004a). The minimum Visbeck coefficient is 150 m^2s^{-1}, the inverse timescale used is $3.5x10^{-6}s^{-1}$, and the distribution of the coefficient in a 10 year mean from the HadGEM1 control run (described later) is shown in Figure 1. The biharmonic adiabatic scheme (Roberts and Marshall 1998) is also used, with coefficient $1.0x10^{12}$ cos^3 (lat) m^4s^{-1} (the latitude variation is needed for stability near the poles); this removes some of the grid-point tracer noise. There is also horizontally-aligned biharmonic tracer mixing in the top 2 model levels, with coefficient $2.5x10^{12}cos^3$ (lat) $m^4 s^{-1}$, which partially represents the enhanced mixing at the ocean surface which the Gent and McWilliams (1990) scheme is unable to deal with.

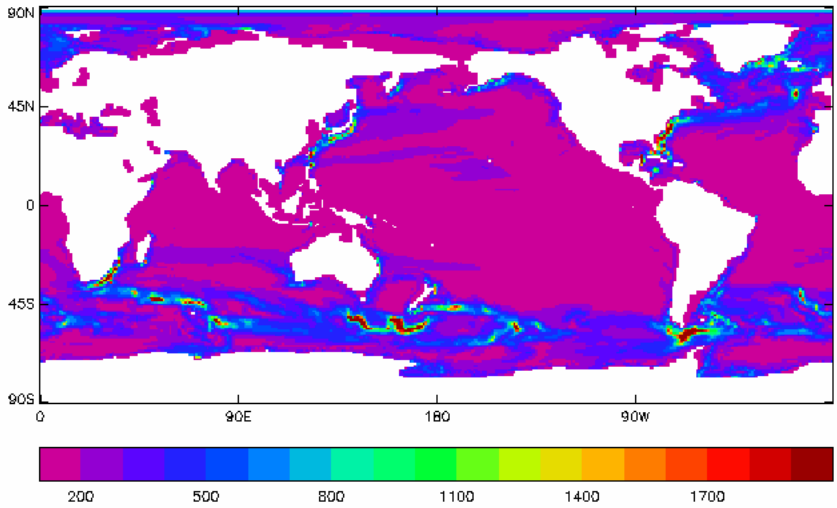

Figure 1: A decadal average of the Visbeck diffusion coefficient in HadGEM1.

Momentum diffusion is achieved using a Laplacian scheme with a constant coefficient of 2000 $m^2 s^{-1}$, together with a scale-selective biharmonic scheme with coefficient $1.0x10^{13}$

$\cos^3$ (lat) m^4 s^{-1}. A pseudo-fourth order advection scheme is used (Pacanowski and Griffies 1998), which is more accurate and generates less grid-scale noise than a second order scheme - this includes upwind mixing at the ocean bottom, to improve model stability at the expense of more excessive mixing.

The model uses Fourier filtering at high latitudes, northwards of 73° N, to remove spurious short-wavelength waves due to the convergence of meridians caused by the use of a latitude-longitude grid. The model timestep is 1 hour, with a mixing timestep once per day. There is a simple semi-implicit representation of linear bottom friction implemented in the model, with a drag coefficient of 0.001, which removes momentum at the ocean bottom depending on the magnitude of the velocities found there.

The ocean model bathymetry is derived from the Smith and Sandwell (1997) 1/30° depth dataset (merged with ETOPO5 1988 1/12° data at high latitudes), which is averaged onto the model grid, then smoothed twice using a 2-dimensional five-point smoother. Important narrow flow pathways are examined and corrected to allow appropriate flow; such areas include the Indonesian region, the channels connecting the North Atlantic and the Nordic Seas, and deep flow pathways in the Atlantic, Pacific and Indian Oceans.

There is a parameterization of flow into three marginal seas where the passages are not resolved by the model grid. For the Mediterranean, Red Sea and Persian Gulf, 0.2Sv, 0.2Sv and 0.1Sv of water respectively is fluxed into and out of these basins; for the Mediterranean, the inflow occurs near the surface and the outflow at depth, while this is reversed for the other two seas. These values are based on observed values, although the Mediterranean value has had to be decreased (from about the 0.7Sv observed (Baringer and Price 1997) because the model does not represent many of the mixing processes that would modulate the water as it flows over the sill.

Convective mixing in the model uses the Rahmstorf (1993) full convection scheme as in HadCM3, but does not use the Roussenov convective adjustment scheme (Roether et al. 1994, which was used in HadCM3). The equation of state remains the UNESCO 1981 polynomial approximation as in HadCM3. There are limits on the model surface salinity, which is not allowed to go outside the range (0,45) psu - it is reset to those limits otherwise.

The land masks for the atmosphere and ocean grids are different, because of the difference in the model resolutions. To enable the daily coupling between the models to be conservative, a tiling scheme has been introduced. For each atmosphere grid box, fractions of the fluxes can be coupled to both land, sea and sea-ice models (depending on the underlying surface type) so that the total flux is conserved - though locally the flux may not be conserved, so diagnosis can be difficult. River runoff is done by a new river routing scheme in the atmosphere, and this collects the runoff into river outflows around the coasts of the ocean model. There have been problems with conservation of fresh water through the coupling, leading to a drift in the free surface height over the initial years of the control run which is described later.

The only ancillary flux file used by the ocean is to enable a balance in the freshwater flux to be maintained, since the accumulation of frozen water on land is not returned into the freshwater cycle, i.e. there is no representation of icebergs calving off ice shelves in the model. Hence an ancillary field is used to add freshwater back into the model, calibrated from HadCM3 to give a balanced freshwater budget.

3.3 Sea ice model description

Sea ice plays an important role in global climate by affecting the exchange of heat, moisture and energy between the ocean and atmosphere. It is also important in climate change because of the ice-albedo feedback: decreasing ice cover results in more absorption of solar radiation at the surface because open water has a much lower albedo than ice. Hence it is important to produce a realistic simulation of sea ice within the coupled model.

In outline, the sea ice model is split in HadGEM1 as in HadCM3 between the atmosphere and ocean model components. The atmosphere part calculates the atmosphere-ice heat fluxes, the diffusive heat flux through the ice, the ice surface temperature and surface melting. This allows the diurnal cycle of the surface temperature to be modelled. The ocean part deals with the remaining thermodynamics, calculates basal melting by heat supplied from the mixed layer, keeps account of snow and ice thickness changes including conversion of submerged snow to ice, and deals with ice dynamics including ridging, using daily mean fields of the atmospheric forcings supplied via coupling routines.

The ice velocities are computed using the Elastic-Viscous-Plastic dynamics of Hunke and Dukowicz (1997). The ice momentum and stress state equations are solved to balance the effects of the wind stress, ocean currents, Coriolis term and the internal ice stresses, while maintaining a viscous plastic ice rheology. Ice is allowed to flow across the North Pole despite the ocean model having a polar island.

The zero-layer thermodynamics model of Semtner (1976), combined with a multiple ice thickness category model (Lipscomb, 2001) is used to capture the sub-gridscale ice thickness distribution. Ice thickness affects many sea ice properties and processes, including the growth rate, ice strength and surface energy fluxes. As ice thickness can vary greatly within the grid box length scale, a multiple ice category model should lead to an improved representation of sea ice processes. A mechanical redistribution (or ridging) scheme is also included, which can convert thinner ice to thicker ice within a grid box.

The ice albedo scheme is based on the scheme of Ebert and Curry (1993) with a parameterisation based on SHEBA observations (Curry et al., 2001). The bare ice albedo is modified (Semtner, 1987) to simulate internal scattering processes in the zero layer scheme, which act to delay the onset of melt. In addition, the snow parameterisation scheme used in the HadGEM1 land surface scheme MOSES2 (Essery et al., 2003) is included, which allows for partial and semi-transparent snow cover. The snow albedo is modified by surface temperature, representing the increase in liquid water content. As a consequence the surface albedo, in addition to surface air temperature, is highly responsive to modelled snow fall events.

The sea ice component model in HadGEM1 is clearly more sophisticated than that used in HadCM3, with improvements to both the thermodynamics and the dynamics. As there are important new features in HadGEM1 and it is not yet documented in full elsewhere, we include a more comprehensive description of the sea ice scheme, including its coupling with the atmosphere and ocean, in Appendix A of this note. We also include a summary table of parameters used in the current version of the sea ice (Table A2).

3.4 Coupling between atmosphere, ocean and sea ice

HadGAM1 is physically coupled to HadGOM1 once per model day. The coupling is carried out by transferring surface atmospheric fluxes to the ocean (and sea ice) grid at the end of

each atmosphere day and by transferring ocean surface boundary conditions (fixed for the duration of the atmosphere day) to the atmosphere grid at the end of each ocean day. The atmosphere-to-ocean coupling fluxes comprise wind stress, shortwave radiation, non-penetrative surface heat flux, precipitation minus evaporation, river outflow, snowfall, sublimation and top and bottom melting of sea ice. The ocean-to-atmosphere boundary fields comprise surface current, ice concentration, ice depth, snow depth and sea surface temperature. Since the coupling occurs only at the atmosphere-ocean-sea ice interface, all the coupling fields are two-dimensional apart from top and bottom melting of sea ice which have an extra dimension to represent ice thickness categories (see Appendix A).

The coupling of fluxes between the atmosphere and ocean grids consists of several steps. Multiple diagnostics are first combined if necessary into a single field (e.g. non-penetrative heat flux is calculated from incoming short and longwave radiation, sensible heat flux and latent heat flux of evaporation), and scaling factors for the appropriate model units are applied in some cases. The fluxes are then transferred to the ocean grid by horizontal bilinear interpolation followed by a coastal adjustment step which maps each coastal point to its nearest compatible point on the atmosphere grid, attempting to correct for discontinuities interpolating across the land/sea boundary. Finally, due to the non-congruent nature of the atmosphere and ocean grids, a further local adjustment is applied to the interpolated fields to ensure that global fluxes are conserved. This interpolation scheme follows that employed in HadCEM (Roberts et al. 2004). For ocean-to-atmosphere coupling, all values of each area-averaged ocean coupling field are then set to a single mean value on the polar rows, which is necessary to avoid numerical problems in the ND.

3.5 HadGSM1 - Slab model description and coupling

HadGAM1 is coupled to a 50m thermodynamic mixed layer ocean (slab) model and sea ice model, forming the Hadley Centre Global Slab Model version 1 (HadGSM1). The surface temperature of the ocean is maintained close to climatological values in the absence of ocean currents by the use of a monthly varying heat flux. This is calculated in a calibration experiment during which the SSTs are reset to climatological values each timestep and the heat flux required to do this is averaged for use in subsequent experiments. The sea-ice model is essentially the same as that used in the full coupled model as described in section 3.3 and Appendix A, except that the ocean to ice heat flux is a simple function of the difference between the ocean temperature and the freezing point of sea water, and the fraction of the grid box covered by ice, instead of the more detailed McPhee scheme (see Appendix A, subsection A.3.5). HadGSM1 includes both EVP dynamics of sea ice and multi-category ice depth thermodynamics as in HadGEM1 itself. The prognostic ice advection in the EVP scheme is driven using surface wind stress and monthly climatological surface currents calibrated from the full coupled model and supplied via external files (the sea ice does not exert a further drag on these currents in the slab model experiments).

Coupling in HadGSM1 follows a similar basic pattern to HadGEM1, using a one day coupling period, but with a few technical differences. In HadGSM1 the slab ocean and sea ice grids are forced to be identical to the atmosphere grid rather than independent, so no spatial interpolation or area averaging is applied in either coupling direction. The internal formulation of the sea ice model is essentially the same as in the full coupled model, but the grid resolution is therefore somewhat coarser in HadGSM1 than HadGEM1 (which has some impact on numerical truncation errors). A consequence for coupling to the sea ice model is that coastal tiling must be applied internally to some calculations. Sea ice at coastal points is taken to be purely thermodynamic with no ice advection (for stability reasons associated

with the coastal tiling). Also, since the slab ocean has no dynamics, ocean surface currents are not predicted, but are supplied from external ancillary files instead as described above.

3.6 Experiments for the IPCC AR4

A number of runs with different configurations of the model will be or have already been conducted, illustrated schematically in Figure 2.

The backbone of the experimental design is the coupled spin up and control run, both of which are run with fixed 1860 forcing levels for greenhouse gases, ozone, sulphur and other aerosol precursor emissions, land surface boundary conditions, etc. On top of this, transient forced coupled runs from 1860 to present with a reconstruction of anthropogenic-only and anthropogenic plus natural forcing boundary conditions are included. These will continue up to 2100 using agreed SRES forcing scenarios, and in one case up to 2200 with a proxy for a stabilisation scenario at 750 ppmv for CO_2.

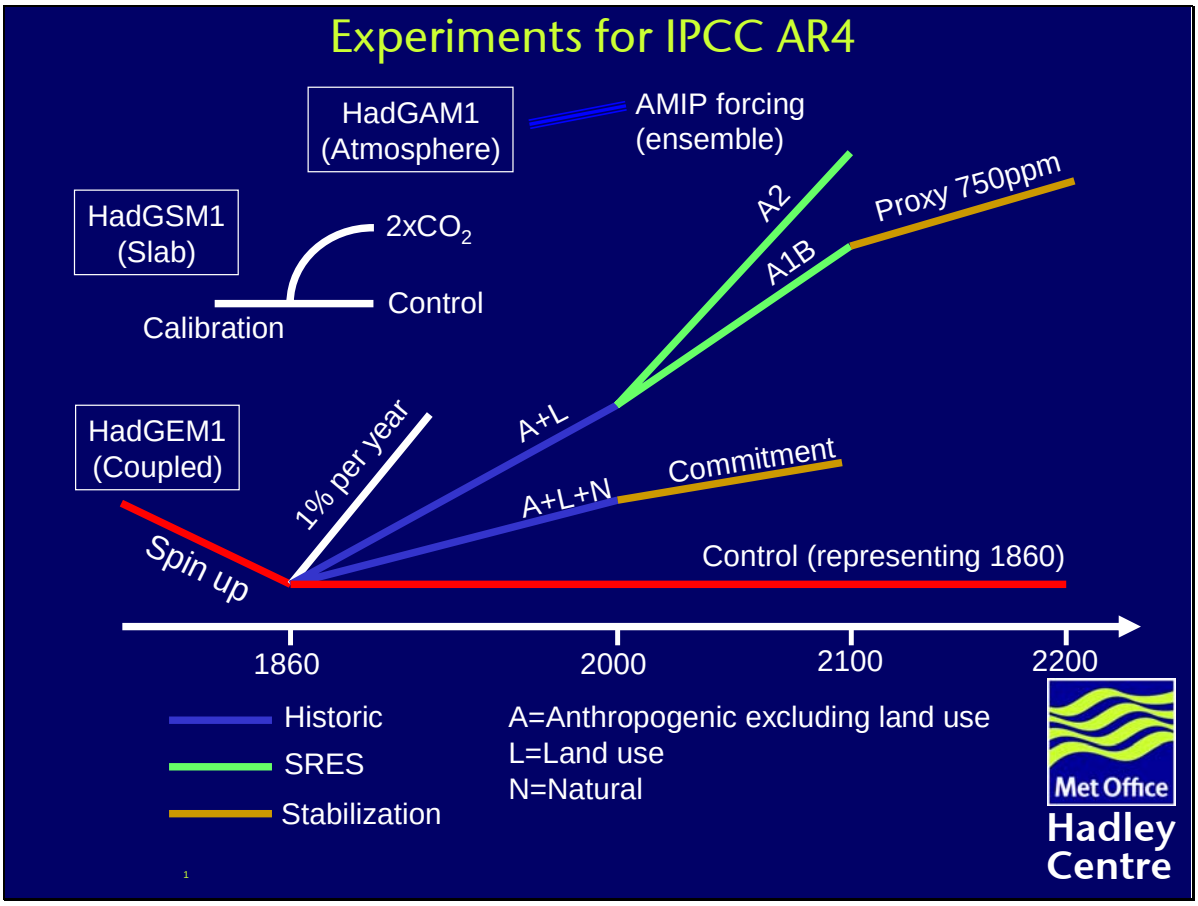

Figure 2: Schematic of the HadGEM1 experimental design for IPCC AR4.

The boundary conditions used in these anthropogenic/natural forced runs are:

- For greenhouse gases – historic reconstructions followed by concentrations as tabulated in the IPCC Third Assessment Report (IPCC TAR).
- For ozone – the SPARC dataset (Randel and Wu, 1999; Randel et al., 1999; Kiehl et al., 1999) up to 2000, with trends derived from off-line STOCHEM chemistry transport model calculations in the troposphere forced by appropriate scenario emissions thereafter, using effective equivalent stratospheric chlorine (EESC) estimates for future stratospheric ozone assessment.
- For sulphur emissions - natural emissions from DMS and volcanoes (Kettle et al. 1999; Jones and Roberts 2004; Andres and Kasgnoc 1998), anthropogenic emission data provided by S. J. Smith, Pacific Northwestern National Laboratory, USA (personal communication).
- For fossil fuel black carbon and biomass smoke - datasets provided by T. Nozawa, National Institute for Environmental Studies, Japan (personal communication).
- For land use changes – following Goldewijk (2001).
- For solar variations – following Solanki and Krivova (2003).
- For volcanic emissions – following a recently updated version of Sato et al. (1993) from http://www.giss.nasa.gov/data/strataer/, averaged into four equal area latitudinal zones (90S-30S, 30S-0, 0-30N, 30N-90N).

An idealised transient run with a standard 1%-per-annum increase in CO_2 from 1 times up to 2 times the control CO_2 level (a "CMIP" run) is also being done, and we concentrate on that rather than the anthropogenic/natural forced runs in this paper. (Note that similar sets of coupled transient runs to the above are also being carried out by several independent modelling groups in the ENSEMBLES EU project, allowing intercomparisons of the response and physical mechanisms to be done over the next few years.)

The slab model simulations consist of a calibration and control run with pre-industrial greenhouse gas concentrations and an anomaly run in which CO_2 is instantaneously doubled ($2xCO_2$). The calibration is started from the same initial conditions as the coupled model spin up and run for 25 years, with the final 10 years being sampled to calculate the heat flux. The control and $2xCO_2$ integrations are both initialised from the end of the calibration and are to be run until quasi-equilibrium is reached, and then on for at least a further 20 years. In this document, we consider 15 years of quasi-equilibrium of the $2xCO_2$ simulation (as the run is yet to be completed) and 38 years of the control (after the first 5 years of spin up). The difference between the two runs defines the equilibrium climate sensitivity and feedbacks of the model (neglecting feedbacks involving changes of ocean circulation and limitations of the slab model as an analogue for the fully coupled model).

A further set of atmosphere-only runs using HadGAM1 forced with AMIP boundary conditions, running from 1978-2003 with corresponding greenhouse gas concentrations, completes the experiment. These AMIP runs are described and analysed in the accompanying note by Martin et al. (2004).

4 Simulated control climate, drifts and variability

We concentrate in this section mainly on coupled aspects of performance in the HadGEM1 spin up and control runs, including drifts, simulation of specific phenomena, and quantify HadGEM1 "skill" compared to HadCM3 using a quasi-objective statistical method. Analysis of the performance of the atmospheric component of HadGEM1 in terms of its mean climate and variability up to intra-seasonal timescales is covered in the accompanying paper by Martin et al. (2004), to which the reader is referred for further details.

The spin up of HadGEM1 was initialised from an ocean state using Levitus (Levitus et al., 1998) fields for September mean potential temperature and salinity, at rest. These were interpolated to the defined model levels and bathymetry with various infilling and adjustment procedures to avoid obvious instabilities or inconsistency. The sea ice was initialised as described in section A.4 of Appendix A. The atmosphere was initialised from an analysed state corresponding to 1 September, which was also used for initialising AMIP runs with HadGAM1.

Due to IPCC time deadlines, the length of the spin up possible before starting the control and other runs (85 years) is shorter than ideal, but is nonetheless considered sufficient to allow the faster components of the climate system to approach equilibrium. A few scientific changes were made during the spin up near the start: to make barotropic and baroclinic filtering in the ocean consistent (minor impact), to correct the albedo of bare ice (affecting mainly the net radiation and to some extent the sea ice extents), and to apply a relative humidity based convective available potential energy closure to mid-level convection (helping to make the model more robust against potential grid point storm instabilities). Towards the end of the spin up a further change was made to correct a bug in the convective momentum transport scheme which has an impact, though not a first-order one, mainly on the tropical warm pool and surrounding regions.

4.1 Global energy balance and sea surface temperature (SST) errors

An important objective for the control simulation is that it should be stable, and in an accurate balance at the top of the atmosphere (TOA), at the atmosphere-ocean-sea ice boundaries, and preferably also in the ocean interior. The latter is particularly difficult to achieve given the short spin up phase, but at the TOA HadGEM1 exhibits only a slight imbalance, with a fairly stable net heating of just over 0.3 W/m^2 averaged over years 1-145 of the combined spin up/control with a negligible trend in the control run itself. While a larger imbalance than in HadCM3, which was very close to zero from the start, this is small enough to be acceptable for multi-century timescale experiments. (It is of interest to note, however, that the TOA net heat flux is more consistent between HadGAM1 and HadGEM1 than was the case with HadCM3 and HadAM3.)

There is a rapid adjustment over the first year or so in the coupled model simulated SST fields, as the model components develop an approximate balance in the near surface and ocean mixed layer. On somewhat longer timescales of a few decades, the sea ice model approaches a stable seasonal cycle and SST and SSS fields react to slower adjustments in the ocean and coupled response. The SST errors, once established (Figure 3) show quite distinct patterns which differ substantially to those exhibited by HadCM3. The predominant errors in HadGEM1 are now cold biases in the tropics, subtropics, and northern mid latitudes. The north Pacific cold bias in HadCM3 is much larger than in HadGEM1, but the equatorial Pacific cold bias is larger in HadGEM1. The warm bias exhibited by HadCM3 in the eastern subtropical oceans is considerably alleviated in HadGEM1 as a consequence of a better

reproduction of the marine stratocumulus cloud (largely absent in HadCM3). This is a combined effect of higher vertical resolution, improved physics and improved dynamics-physics coupling in HadGEM1, possibly assisted by the revised vertical grid staggering. The Southern Ocean warm bias in HadCM3 has also been removed in HadGEM1. Analysis of the large scale cold SST bias patterns suggests they are probably linked to excessively strong surface windstresses and associated latent heat flux forcing errors, but the reasons for these atmospheric biases, which are also present (though not so pronounced) in HadGAM1 experiments with specified SSTs (see Martin et al. 2004), is not yet clear.

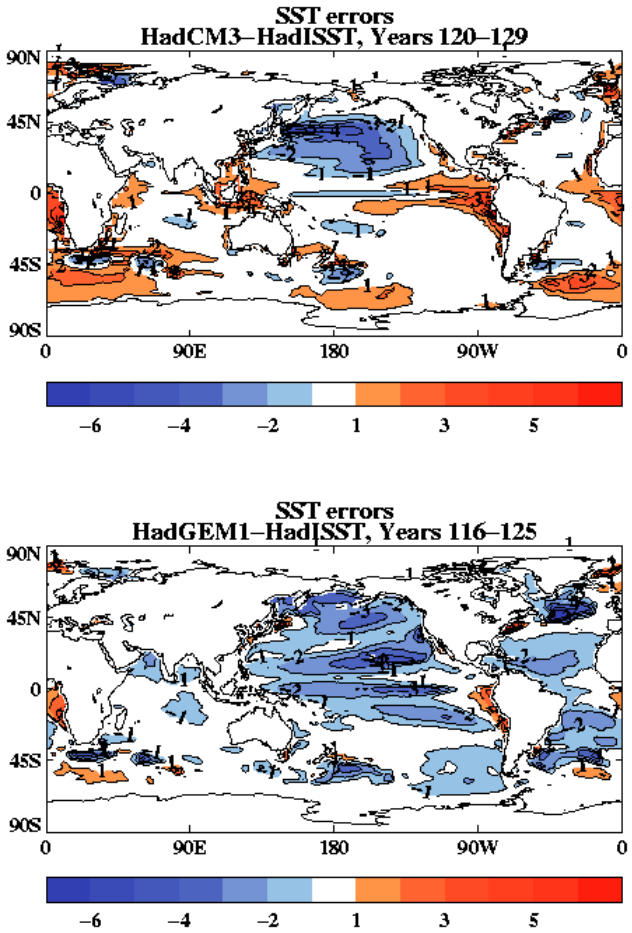

Figure 3: Decadal mean SST error patterns relative to HadISST (Rayner et al., 2003) simulated by HadCM3 (top) and HadGEM1 (bottom) about 120 years into their respective spin up and control runs.

4.2 Oceanic adjustments and simulated mean climate

We next examine timeseries from the model paying particular attention to the adjustments of the ocean towards a steady state. We also analyse years 116-125 counting from the start of the spin up (corresponding to the fourth decade of the control run) to quantify drifts relative to the initial state.

Drifts in temperature and salinity

SST error patterns compared against Levitus et al. (1998) for the years 1-10 and 116-125 (Figure 4, left panels) is dominated by cooling in both hemispheres as previously shown. The patterns are similar for both periods but the magnitude of the differences is greater in the later period. Global and hemispheric mean SST trends (Figure 5) show that the differences stabilise over the first fifty years, cooling being established in the first twenty years but then a slight warming taking place between years 30-50.

SSS error patterns compared to Levitus et al. (1998) for the two periods (Figure 4, right panels), show a pattern of large-scale freshening except in the ice covered regions and in the tropics where salinity has increased. Between years 1-10 and 116-125 the surface freshening can be seen to intensify. This is also apparent in the timeseries of surface salinity (Figure 6), where a freshening trend in surface salinity is apparent in both hemispheres. The trend decreases significantly over the period of the control.

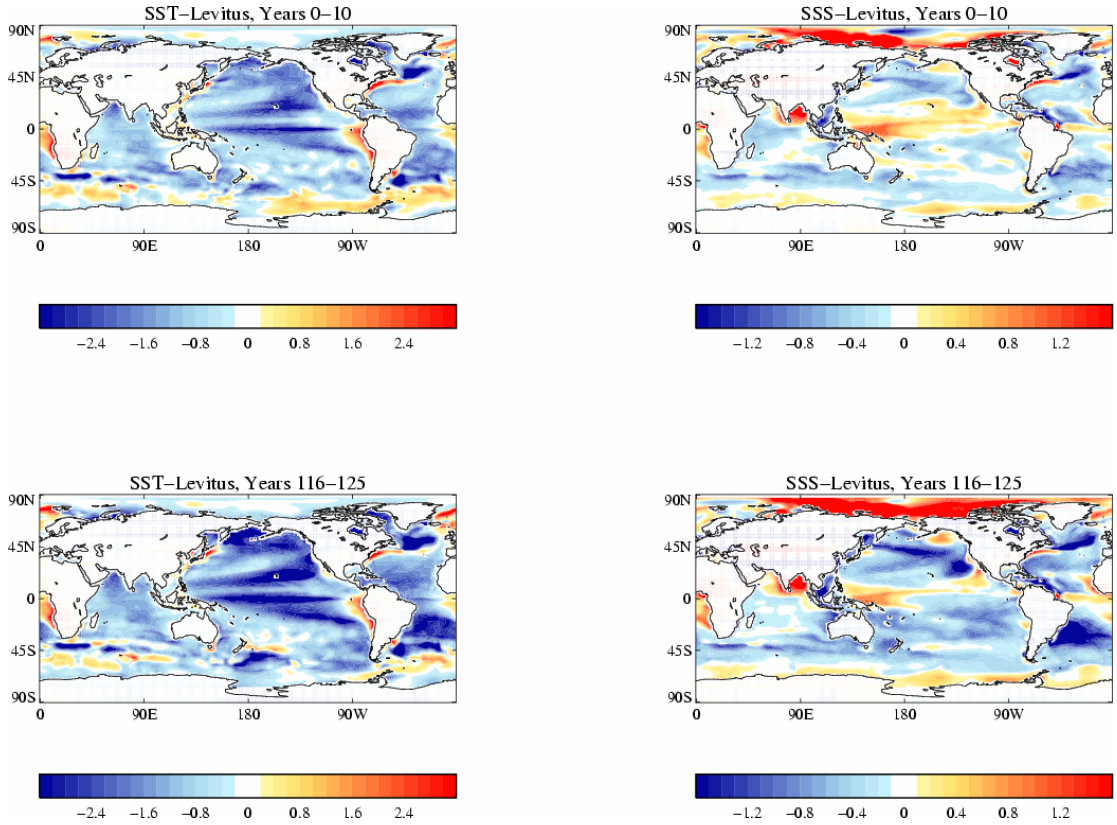

Figure 4: Sea Surface Temperature (SST) and Sea Surface Salinity (SSS) differences relative to Levitus for years 1-10 and years 116-125 of the combined spin up and control.

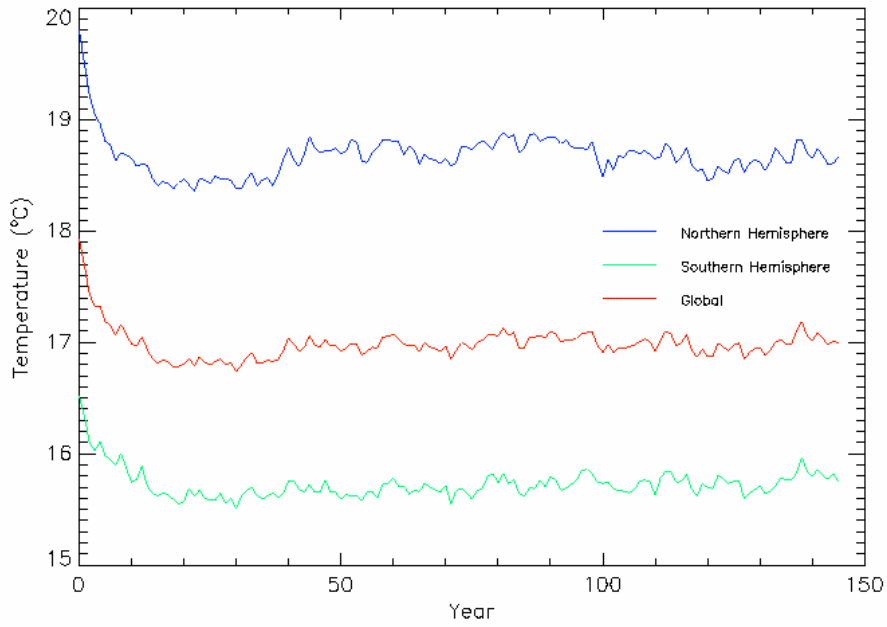

Figure 5: Timeseries of hemispheric and global average SST from the spin up and control.

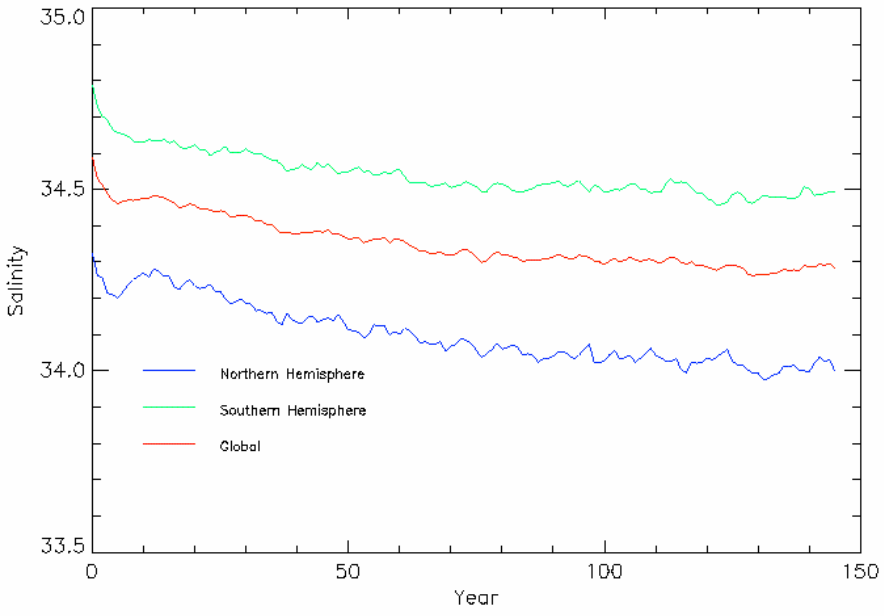

Figure 6: Timeseries of hemispheric and global average SSS from the spin up and control.

Hovmuller plots of temperature and salinity in the control as a function of depth and time (Figure 7) show that while SST is cooling, the temperature is warming globally in the upper 2000m of the water column with cooling below. The global volume averaged temperature increases through the control from 3.64°C in years 1-10 to 3.74°C in years 116-125. This increase is consistent with a positive net downward top of the atmosphere (TOA) radiation. The heat capacity of the atmosphere being small, any residual TOA energy imbalance must be taken up by the ocean. While an increase in volume averaged temperature may appear inconsistent with surface cooling, it can be explained by the different timescales for equilibration of the coupled atmosphere/upper ocean compared to the deep ocean.

Figure 8 shows the zonally averaged temperature differences relative to Levitus et al. (1998) for each ocean basin in years 116-125. The subsurface temperature shows the largest increases in the tropical Atlantic and in the Northern Indian Ocean. The subsurface temperature also increases in the Pacific subtropical gyres and the Arctic and subpolar North Atlantic. In addition to temperature decreases in the near surface layer, the subsurface temperature also decreases in the Southern Ocean. In the Southern Ocean the temperature profile is typically produced by a balance between diffusive cooling and advective warming (Gregory, 2000). This suggests that in HadGEM1 either the mixing or circulation are leading to subsurface cooling.

Figure 7 also shows Hovmuller diagrams of the global salinity drifts. This shows freshening down to 500 m and salinification below this down to 2000 m. Below 2000 m a more complex time-dependent drift occurs but is eventually dominated by salinification at depth. The volume average salinity increases from 34.7258 in years 1-10 to 34.7279 in years 116-125. This is consistent with a reduction in surface height due to a deficit in runoff (caused by non-conservation of runoff when passed from the atmosphere to the ocean). Figure 8 shows that there is a correlation between subsurface warming (cooling) and subsurface salinification (freshening).

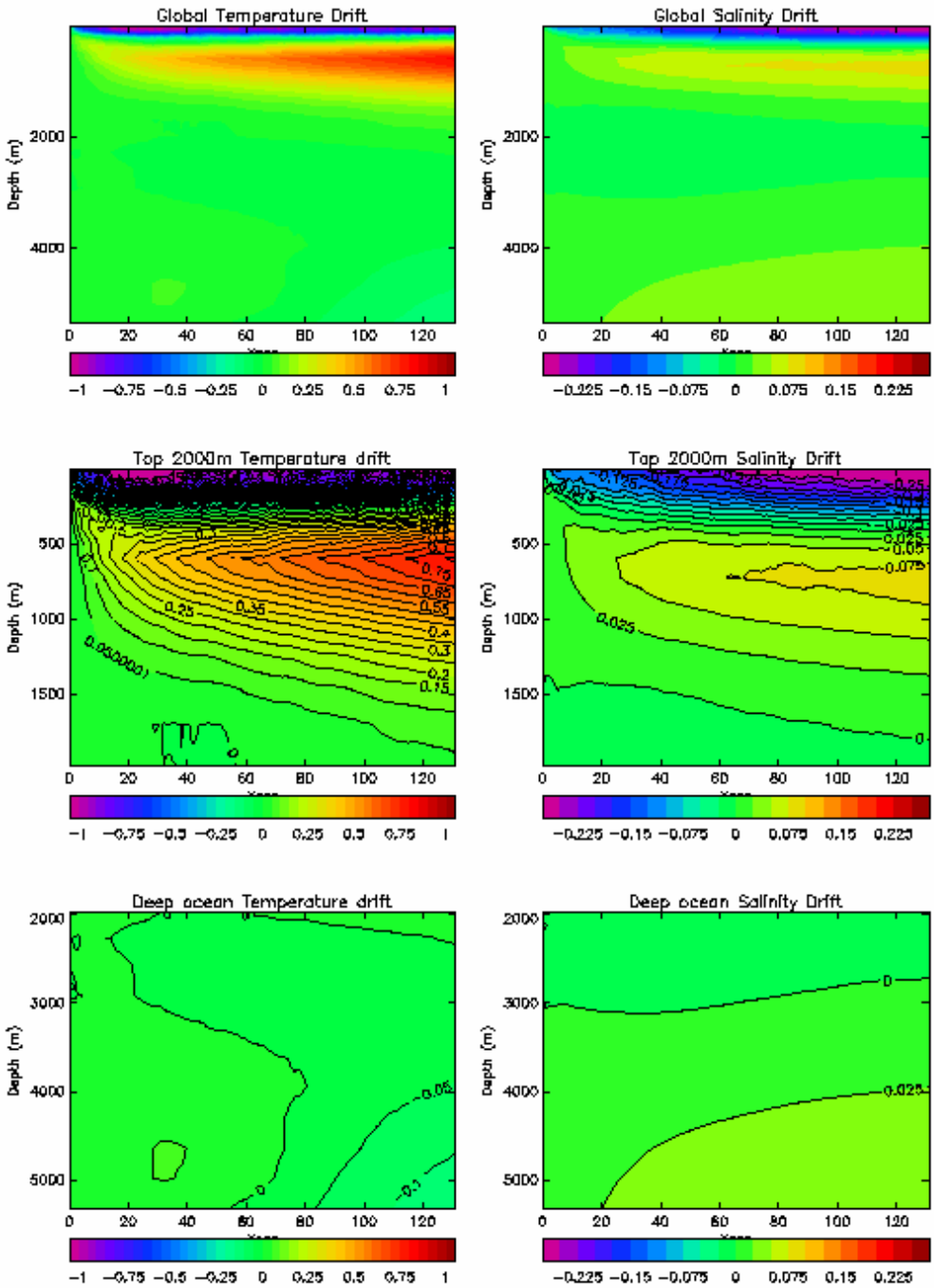

Figure 7: Hovmuller plots (as a function of depth and time) of global temperature and salinity drifts of the spin-up/control run of HadGEM1 relative to the initial conditions.

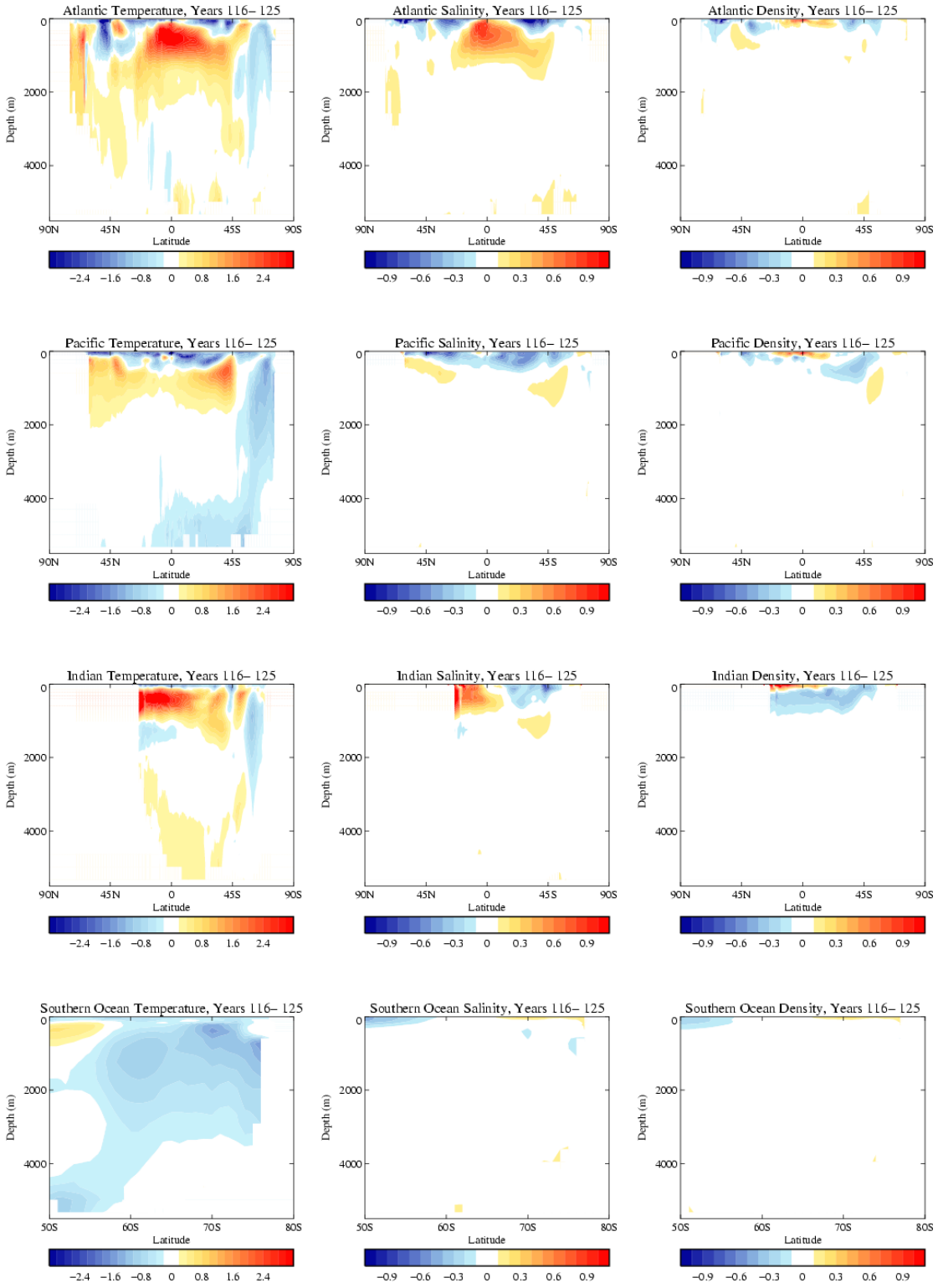

Figure 8: Zonally averaged temperature and salinity differences at years 116-125 relative to Levitus et al. (1998) for each ocean basin

Heat and freshwater transports

Figure 9 shows the implied and actual ocean heat transports for years 1-10 and years 116-125. The implied heat transports are calculated by integrating the zonally integrated surface

fluxes southward assuming that the heat transport at 90°N is zero. In both periods there is a residual southward transport at 90°S which implies that there is a net heat gain by the ocean. This agrees with the increase in volume averaged temperature discussed earlier.

Gordon et al. (2000) discuss the relationship between the implied and actual ocean heat transports. In the zonal average, any difference between the surface fluxes and the advection of heat will lead to a change in the zonally and vertically averaged temperature. In Figure 9 this can be seen as regions where the gradients of the implied and actual heat transports differ. The largest differences in the heat transport gradients occur in the subtropics between 10 and 30°N (and S). The vertically averaged temperature change (not shown) does show a temperature increase in the subtropics which is partly offset by decreases in the Southern Ocean (as may be expected from Figure 8).

Observed heat transports from Macdonald and Wunsch (1996) and Ganachaud and Wunsch (2000) are also shown on Figure 9 with the error bars of ±0.3 PW. At both latitudes it is clear that HadGEM1 is within the observational uncertainty.

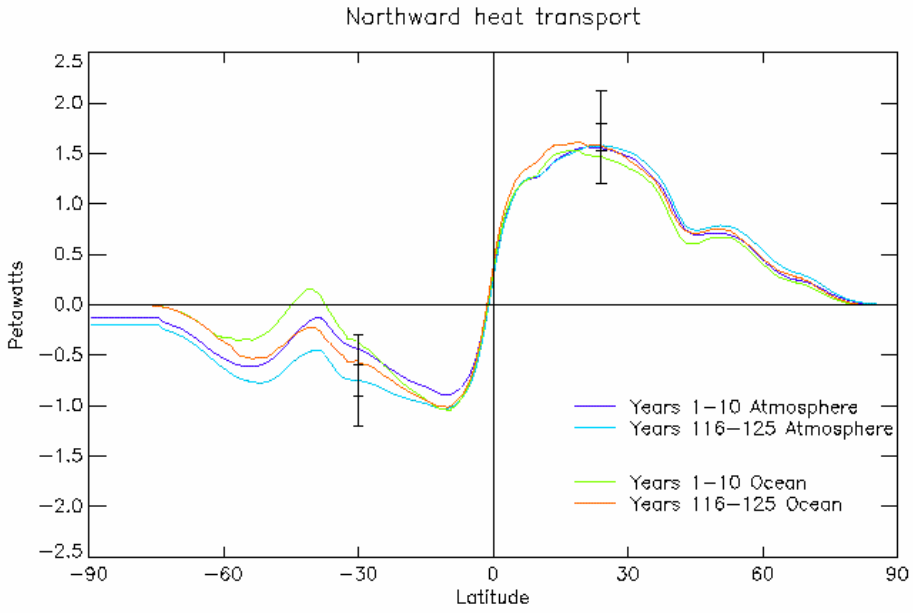

Figure 9: implied and actual global ocean heat transports: years 1-10 and 116-125. Estimates from Macdonald and Wunsch (1996) and Ganachaud and Wunsch (2000) at 24°N and 30°S are shown with the appropriate error bars.

Figure 10 shows the implied freshwater transports at different times in the control. The surface freshwater fluxes have been integrated northwards from 90°S. At each time there is a small residual southward transport at 90°N which indicates that there is a small deficit in the freshwater budget of 0.04Sv due to the non-conservation of runoff as discussed earlier. Through the run there is some adjustment in the implied freshwater transports presumably driven by changes in the surface temperature.

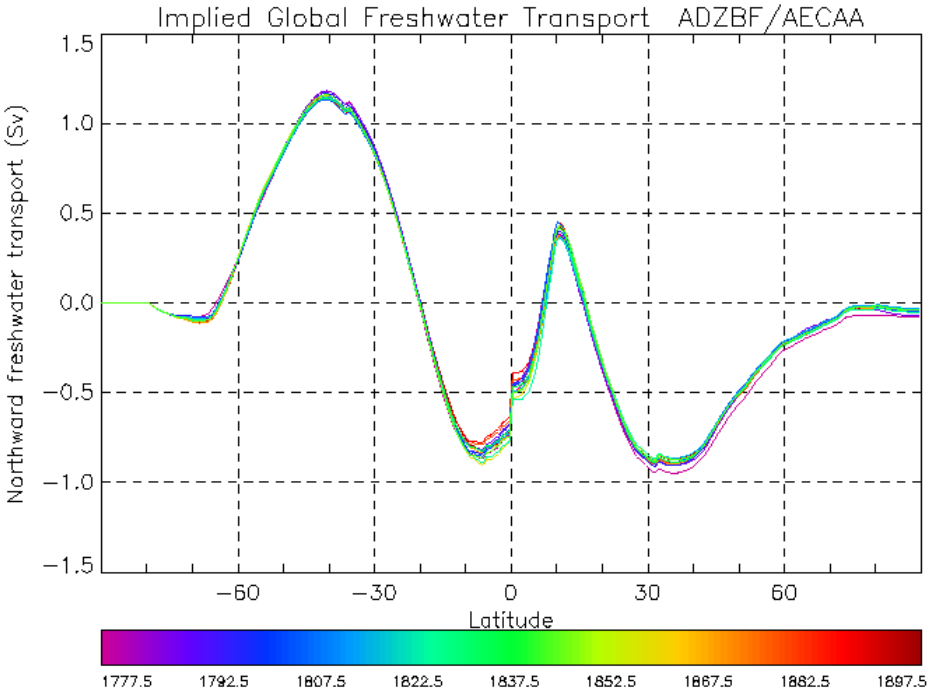

Figure 10: Implied global freshwater transports for successive decades in the spin up/control run of HadGEM1 indicated by a progression of colours (year 1 of the spin up is equivalent to 1774).

Thermohaline circulation

Figure 11 shows the overturning in the Atlantic in HadCM3 and HadGEM1. The overturning in HadGEM1 has a maximum of approximately 16 Sv compared with 20 Sv in HadCM3. The observations of Hall and Bryden (1982) suggest a maximum of approximately 18 Sv at 24°N.

The pattern of the overturning is also different in HadGEM1; HadCM3 was characterised by strong sinking at the Northern boundary with southward flow almost following pressure surfaces, while HadGEM1 shows sinking over a range of Northern latitudes and a suggestion of downslope flow (in spite of having no bottom boundary layer).

Associated with these differences in the overturning we also see a very different pattern in the salinity drifts; HadCM3 showed large scale salinification while in HadGEM1 this is more localised in the Equatorial region.

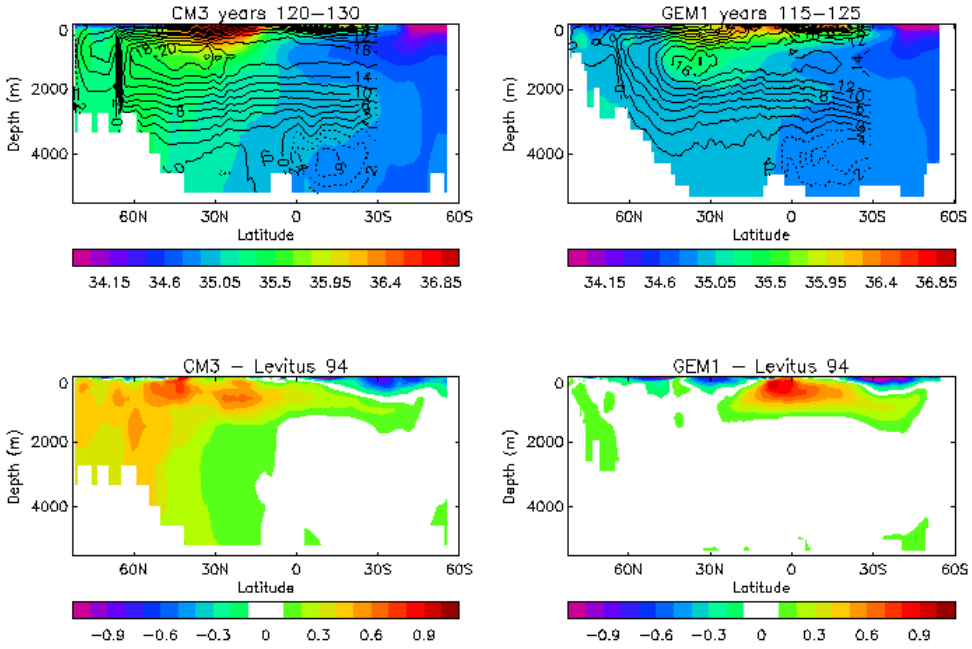

Figure 11: Atlantic overturning and salinity drifts in HadGEM1 control compared with HadCM3 control

The Indonesian throughflow (Figure 12, top) has an average magnitude of 15.6 Sv for years 116-125. This compares with an estimate of 7±12 Sv by Wijffels et al. (1996). The Antarctic Circumpolar Current (ACC) (Figure 12, bottom) has an average magnitude of 203 Sv over the same period. This is much higher than observational estimates of 130 ± 13 Sv (Whitworth et al. 1982) but comparable with other coupled models.

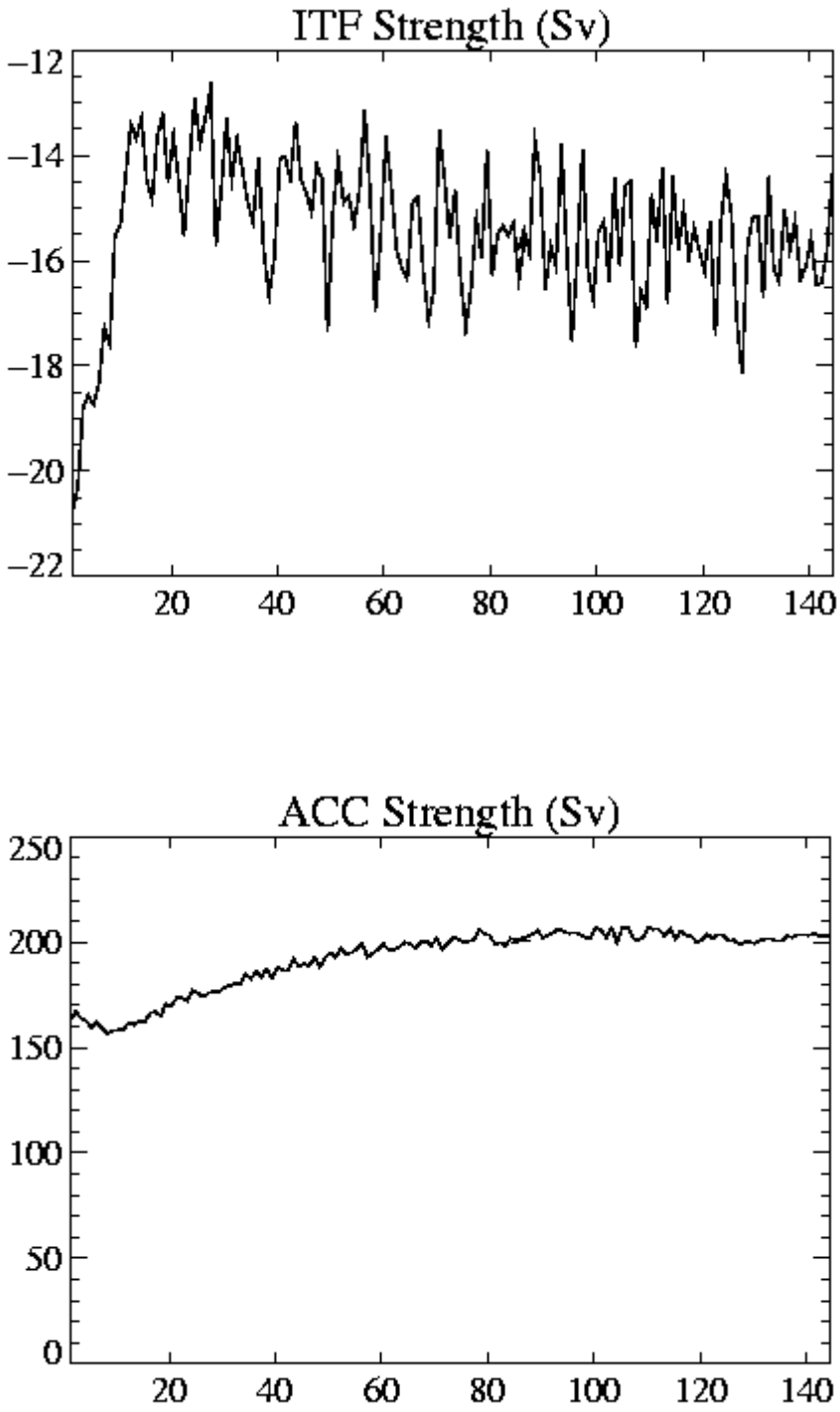

Figure 12: Timeseries of Indonesian throughflow (ITF) and Antarctic Circumpolar Current magnitude (Sv).

Ventilation

Figure 13 shows the mixed layer depths from HadGEM1 compared with observations from Levitus et al. (1998). HadGEM1 has significantly deeper mixed layer depths in the winter hemisphere than Levitus et al. (1998). In HadGEM1 we take the wind mixing energy scaling factor to be equal to 0.55. Figure 13 illustrates that this value gives some improvement in the mixed layer depths when compared with the value of 0.7 which was used in HadCM3. The value of 0.55 is within the range of 0.5 to 1.0 suggested by the MILE experiment (Davis et al., 1981; Warn-Varnas et al. 1981).

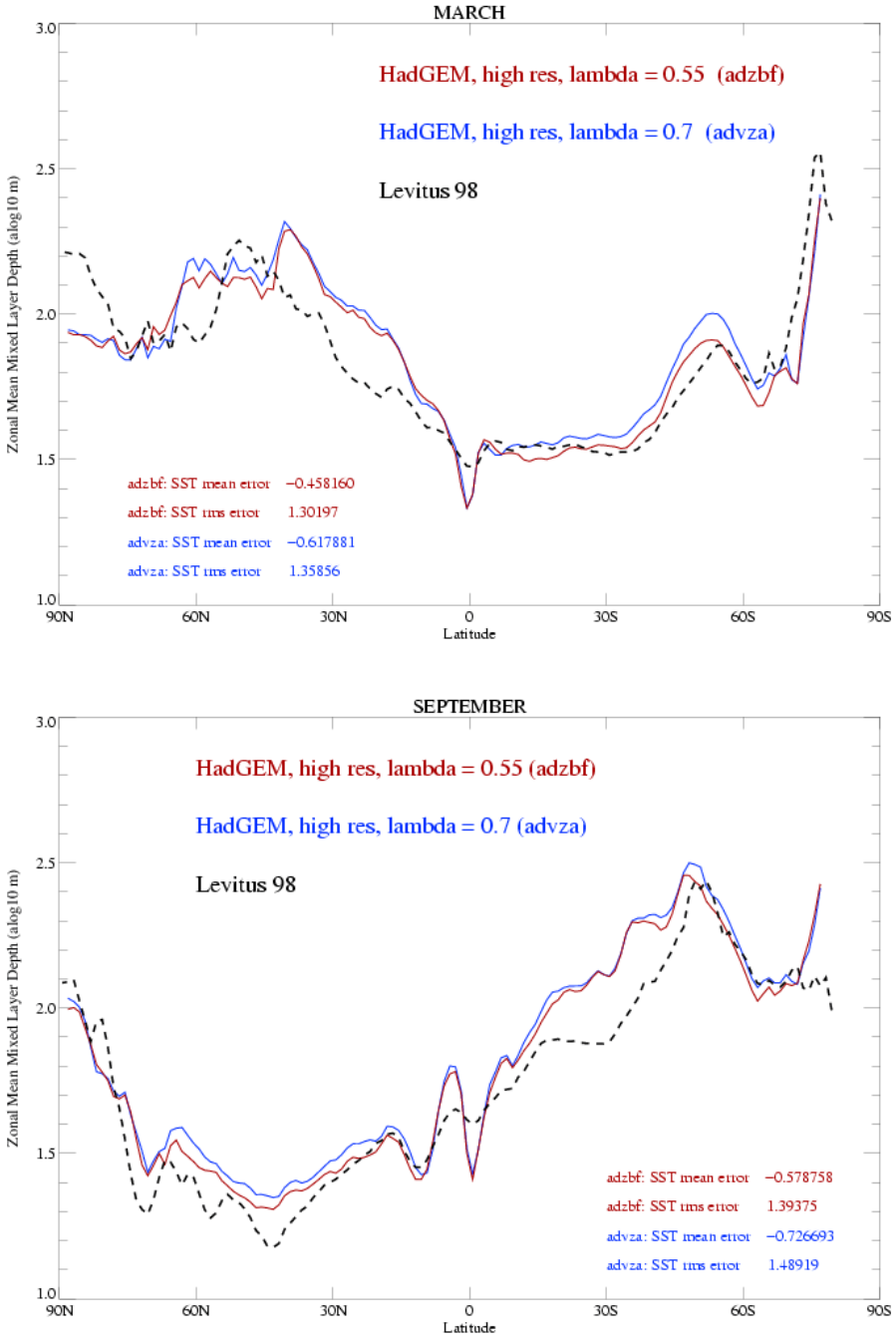

Figure 13: March and September zonal mean mixed layer depths in HadGEM1 (lambda (wind mixing energy scaling factor) equal to 0.55) compared with Levitus et al. (1998). For comparison we also show a test with a lambda value of 0.7 as used in HadCM3.

4.3 Sea ice

Figure 14 shows timeseries of the ice concentration in each hemisphere for 60 years of the control integration, compared with the observational dataset HadISST (Rayner et al., 2003) , and a long term mean of the HadCM3 control.

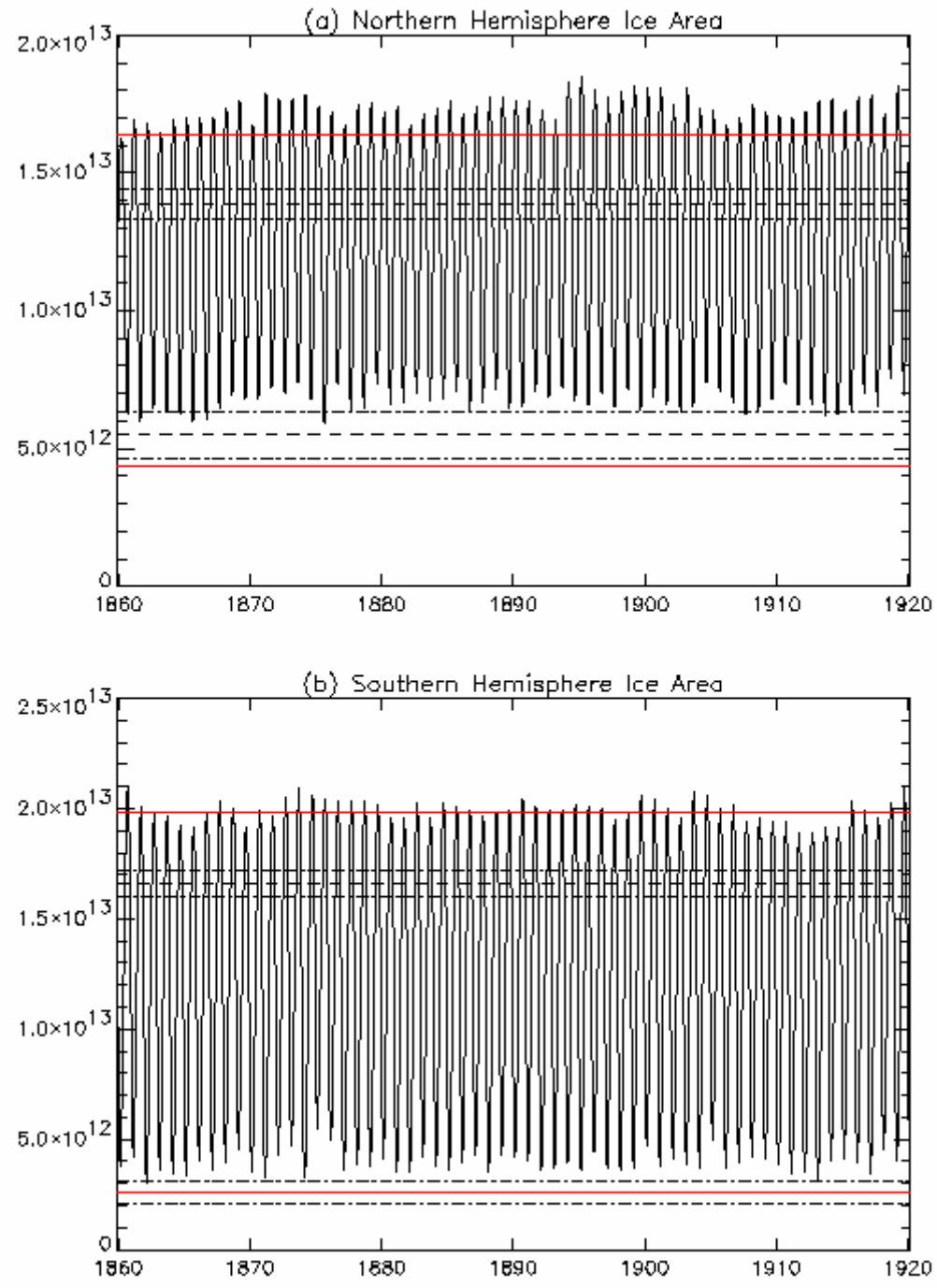

Figure 14: Timeseries of mean ice concentration for HadGEM1. Dashed lines show the mean +/- 2 standard deviations for years 1979-2002 of HadISST data (the period for which SSMI data is included). The red lines are for a 240 year mean of the HadCM3 control.

Both HadCM3 and HadGEM1 controls simulate the climate forced by the mid-late 19th century concentrations of atmospheric greenhouse gases, and are being compared here with the contemporary ice concentration observations of HadISST. Since the modeled sea-ice area responds linearly to the global mean surface air temperature, at least in the Arctic (Gregory et al., 2002), the HadISST ice area observations should be regarded as a lower limit when used to validate the model control simulations. The amplitude of the seasonal cycle of ice area compares well with observations in the Antarctic, but is larger in the Arctic. As expected for a cooler global climate, the maximum and minimum ice areas in both hemispheres are larger than current day observations.

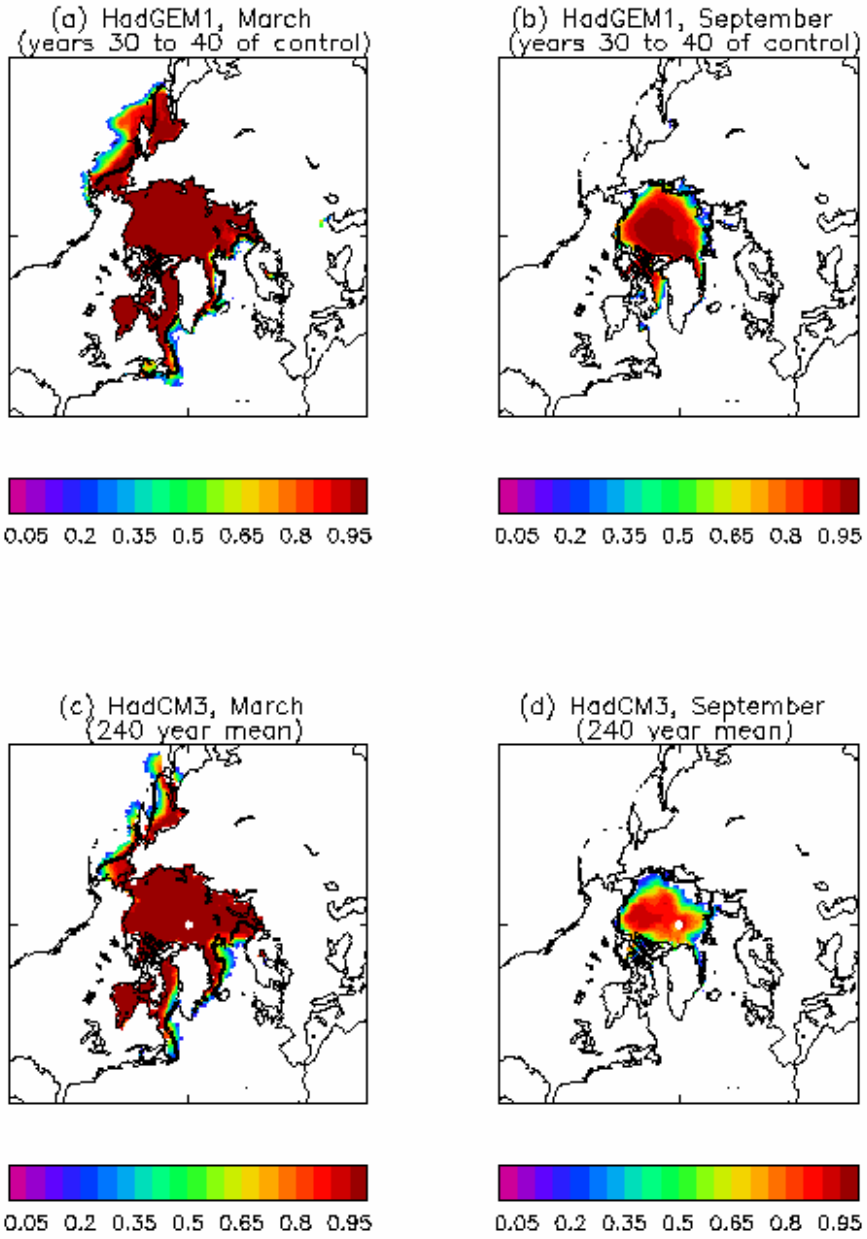

Figure 15: Mean Arctic sea ice concentration for HadGEM1 and HadCM3. The thick lines show 0.15 contours for HadISST data. Model data is only shown where it is >0.15, as the SSMI does not detect ice below this concentration.

In the Arctic, in winter both HadGEM1 and HadCM3 have greater ice coverage (Figure 15) in the North Atlantic, Bering Sea and the Sea of Okhotsk than in observations. This is consistent with the cooling of the ocean surface in HadGEM1, in particular the presence of a cold SST bias in the North Pacific. HadCM3 probably had too much ice in the Greenland-Iceland-Norwegian seas, which is reduced in HadGEM1. In the Antarctic, the winter sea ice extent in HadGEM1 agrees reasonably well with observations (Figure 16). In the summer there is a larger area of ice of high concentration than in HadCM3, which is an improvement.

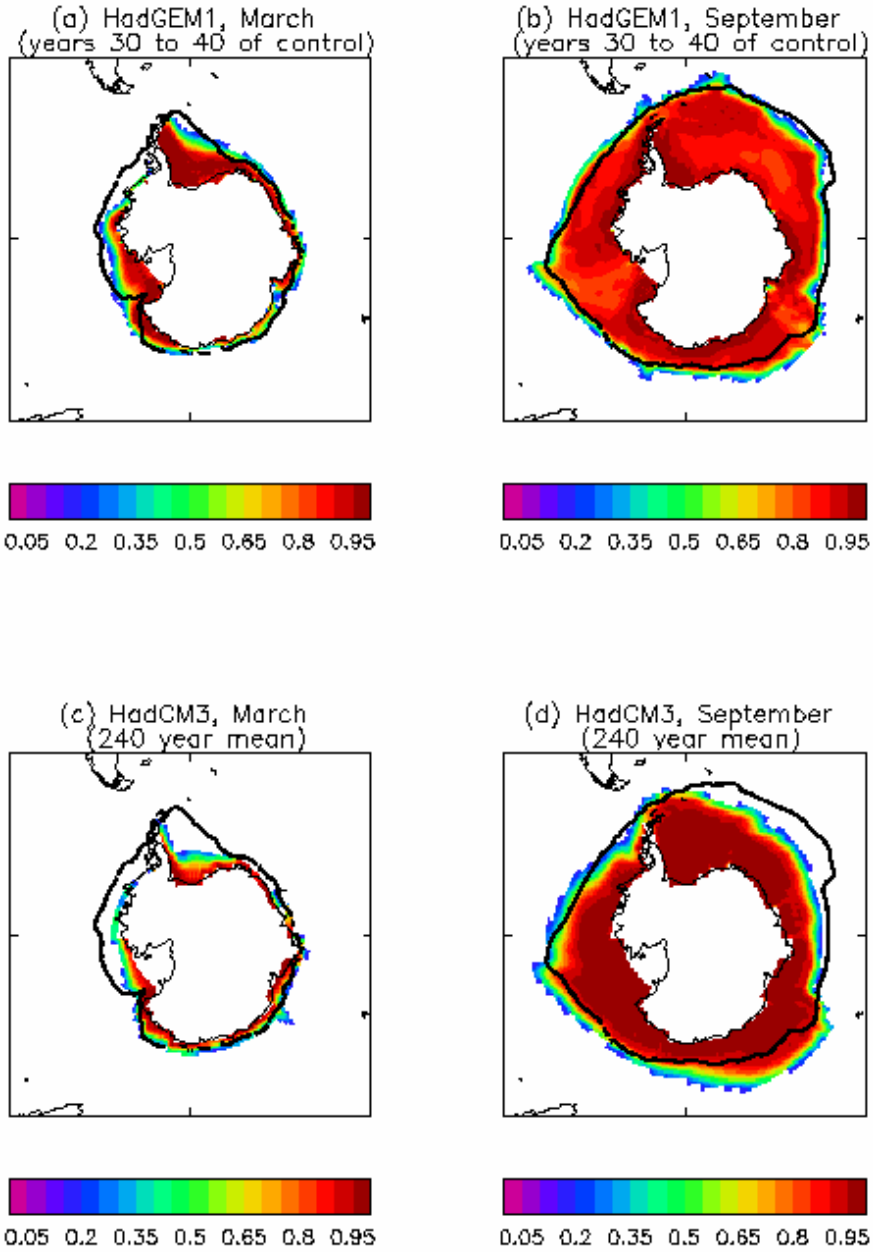

Figure 16: Mean Antarctic sea ice concentration for HadGEM1 and HadCM3. The thick lines show 0.15 contours for HadISST data. Model data is only shown where it is >0.15.

The simulation of ice depth in the Arctic is much improved in HadGEM1 (Figure 17). The deepest ice is banked up against the north Greenland coast and the Canadian Archipelago as observed (Bourke and Garrett, 1987), whereas in HadCM3 the deepest ice occurred in the centre of the Beaufort Gyre. The improvement in HadGEM1 is likely to be partly due to more realistic atmospheric surface pressure fields which drive the winds and ice velocities (discussed later), and partly due to the inclusion of the ice thickness distribution. This scheme, combined with the ridging mechanics, allows greater ice volume mobility than in HadCM3 resulting in relatively rapid ice redistribution in the Arctic basin in response to interannual variability in wind forcing. The mean winter HadGEM1 ice volume in the northern hemisphere is 4.0×10^{13} $m^{3,}$ in good agreement with HadCM3 (3.9×10^{13} m^3). The NH summer HadGEM1 ice volume (2.0×10^{13} m^3) is double that of HadCM3, resulting from a more consolidated ice pack and increased thickness on the Canadian coast. The southern hemisphere ice volumes are similar in HadCM3 and HadGEM1.

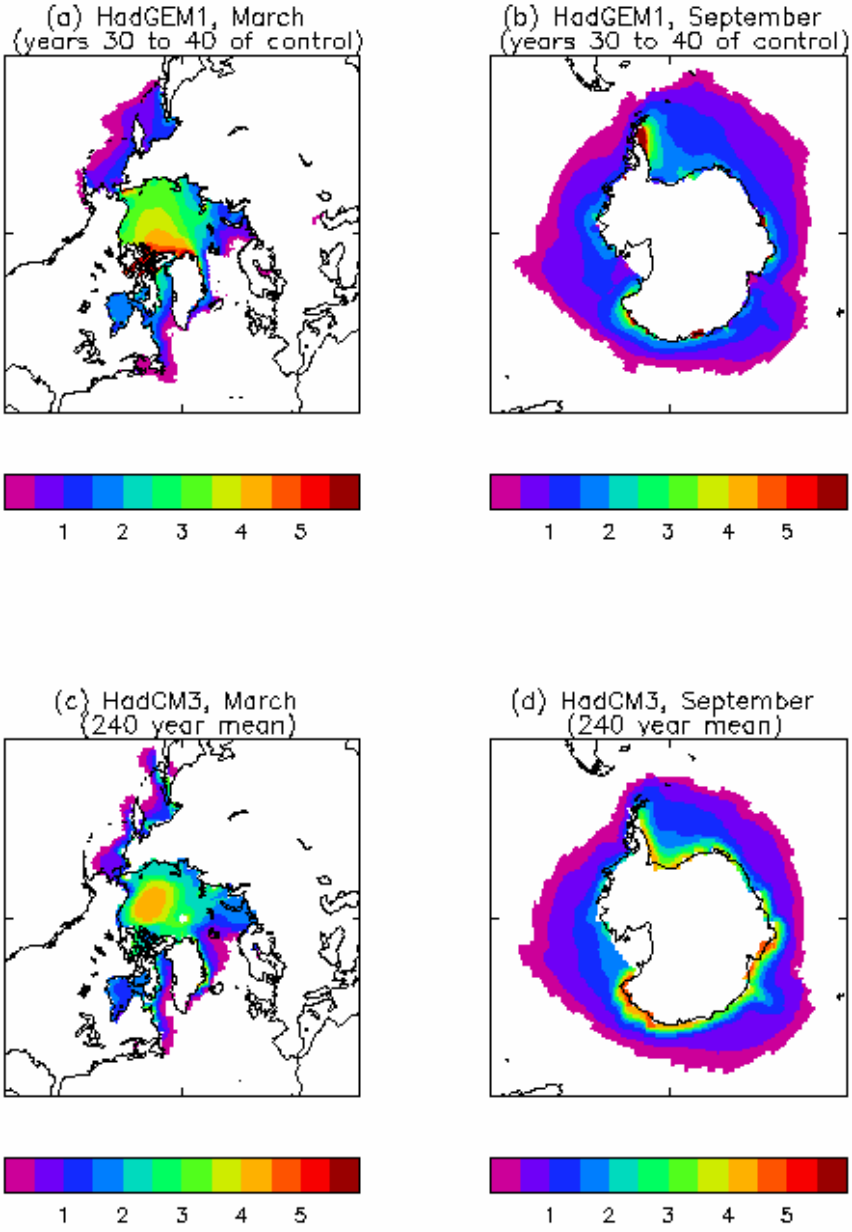

Figure 17: Mean aggregate ice depth for HadGEM1 and HadCM3. Values are only shown where the sea ice concentration is > 0.15.

The spatial pattern of ice motion is improved in HadGEM1 (Figure 18), partly due to the higher resolution. In the Arctic, the coherent southward flow of ice either side of Greenland is now captured, and the movement of ice in the central Arctic is improved. In HadCM3 a persistent high pressure system centred over the Beaufort Gyre caused strong circulation of the ice here, which may contribute to the poor distribution of ice thickness. The export of sea-ice through the Fram Strait is estimated to be 0.08Sv, compared to the 0.09Sv suggested by Aagaard and Carmack (1989), and 0.03Sv in HadCM3. This increased export is consistent with higher ice velocities in the Fram strait and the flow of ice across the pole, which was not allowed in HadCM3.

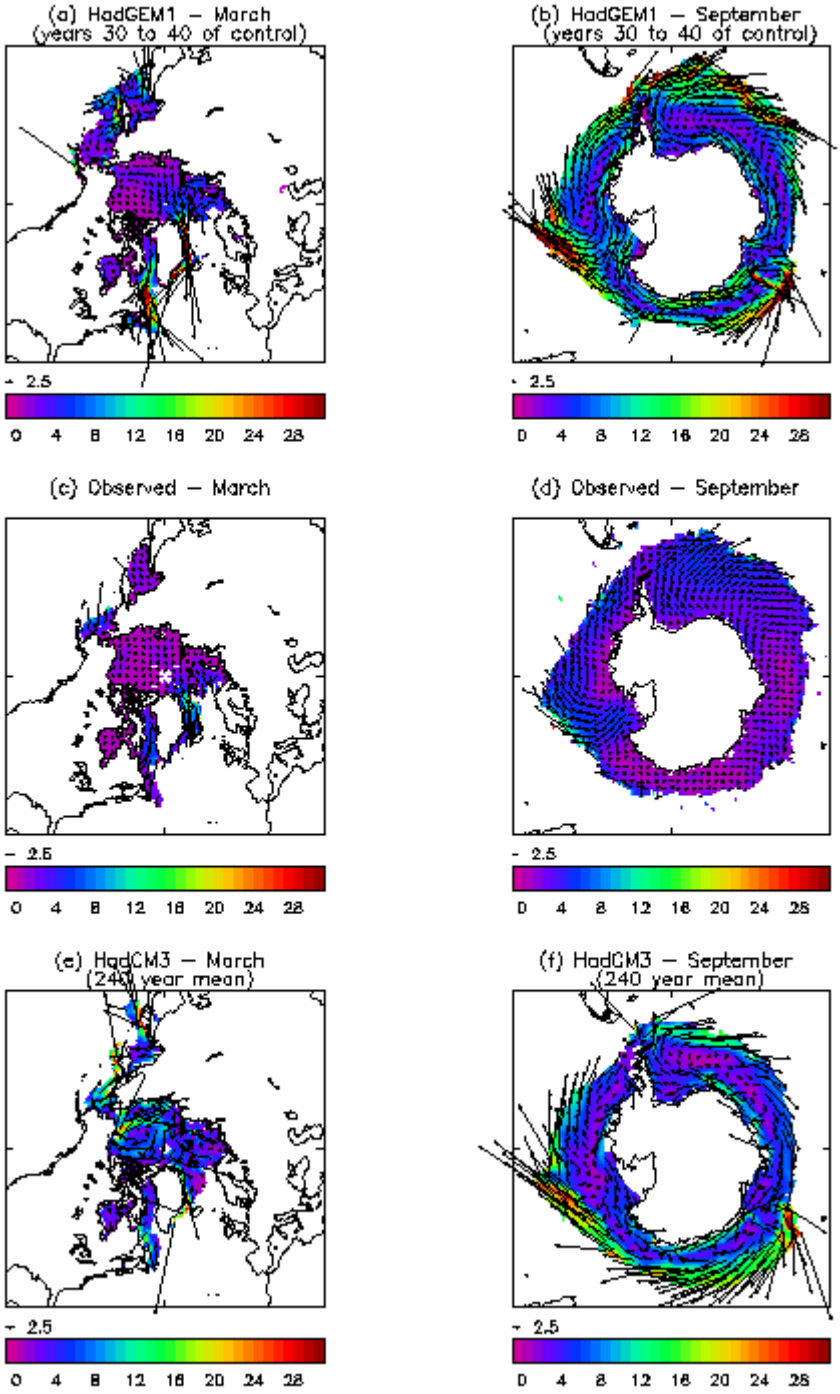

Figure 18: Mean sea ice velocities for HadGEM1, HadCM3 and observations (Fowler, 2003). For the model data, values are only shown where the sea ice concentration is >0.15.

In the Antarctic, higher ice mobility of HadGEM1 leads to the off-shore winds causing strong ice formation in the shore leads at the front of the major ice shelves. The increased northward ice flux in these regions provides an improved ice drift pattern than HadCM3 when compared with observations.

The annual variation in the ice surface albedo in the Beaufort Sea (Figure 19) is validated using SHEBA observations (Curry et al., 2001). The HadGEM1 ice albedo shows a better agreement with observations than the simpler HadCM3 scheme, providing a shorter summer melt period (low albedo) consistent with the increase in summer ice volume and ice area.

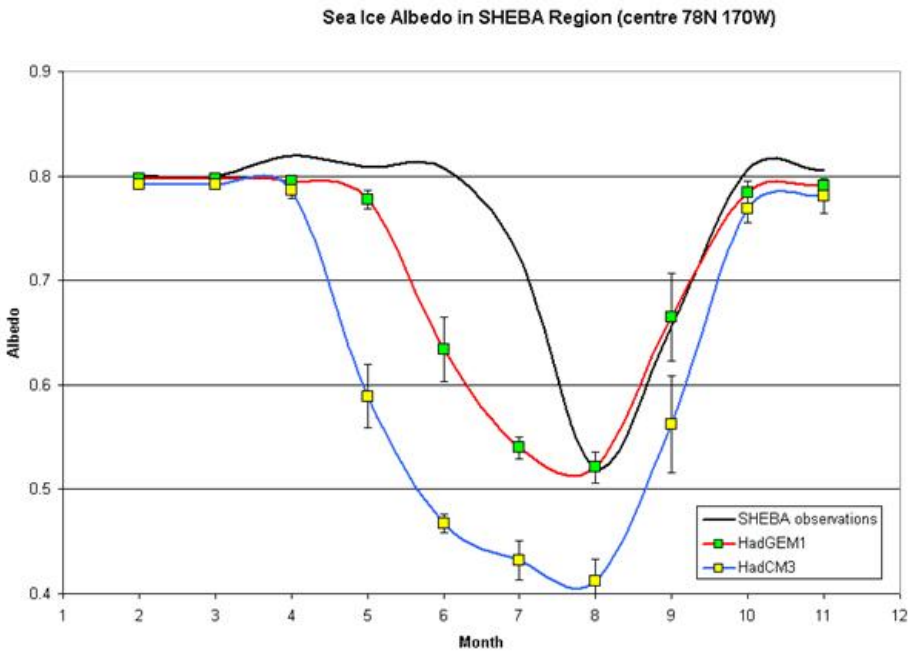

Figure 19: The annual variation in ice albedo for HadGEM1 compared with SHEBA observations and HadCM3. Bars show one standard deviation of the interannual variability for each month.

In summary, HadGEM1 includes a more sophisticated sea ice model than HadCM3. The ice thickness distribution is much improved in the Arctic, and the spatial pattern of ice velocities is better. The simulation of the ice concentration is good although the ice tends to be too extensive, due in part to the cold SST bias. The annual variation in the ice surface albedo is improved.

4.4 Variability and associated phenomena

Martin et al. (2004) discuss the simulation of atmospheric variability on synoptic to intra-seasonal timescales. Here we focus on inter-annual and longer timescales, and coupled modes of variability.

Simulation of El-Nino

The mean climatological SSTs and zonal windstress in the equatorial tropical Pacific (Figure 20) reveal that in HadGEM1 the trade winds are too strong westwards of about 150°W. This is directly responsible for driving excessive upwelling across much of the Tropical Pacific, suppressing SSTs and pushing the themocline too deep in the W. Pacific warm pool. In fact the thermocline in HadGEM1 is about 20-25 metre too deep in December in the western tropical Pacific compared with an ocean analysis (not shown). The thermocline depth in the western tropical Pacific in HadCM3 and HadCEM was very close to the ocean analysis, by contrast, reflecting the fact that the equatorial windstress forcing was closer to reality in those models.

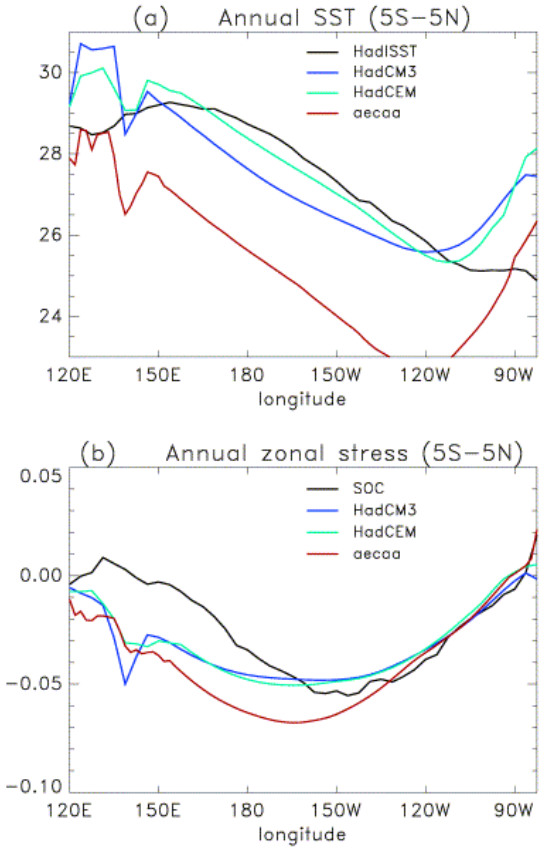

Figure 20: Annual mean tropical Pacific SSTs and zonal windstress in HadGEM1 (aecaa), compared to HadCM3, HadCEM and climatological data (HadISST and SOC, respectively).

Interannual variability of Nino-3 SST anomalies (Figure 21) shows ENSO events in HadGEM1 in comparison with HadCM3, HadCEM and the HadISST climatology. The standard deviation is somewhat low in HadGEM1 at 0.65 K in HadGEM1 compared to 0.80 K based on HadISST. Both HadCM3 (0.85 K) and HadCEM (1.12 K) overestimated the variability by this measure.

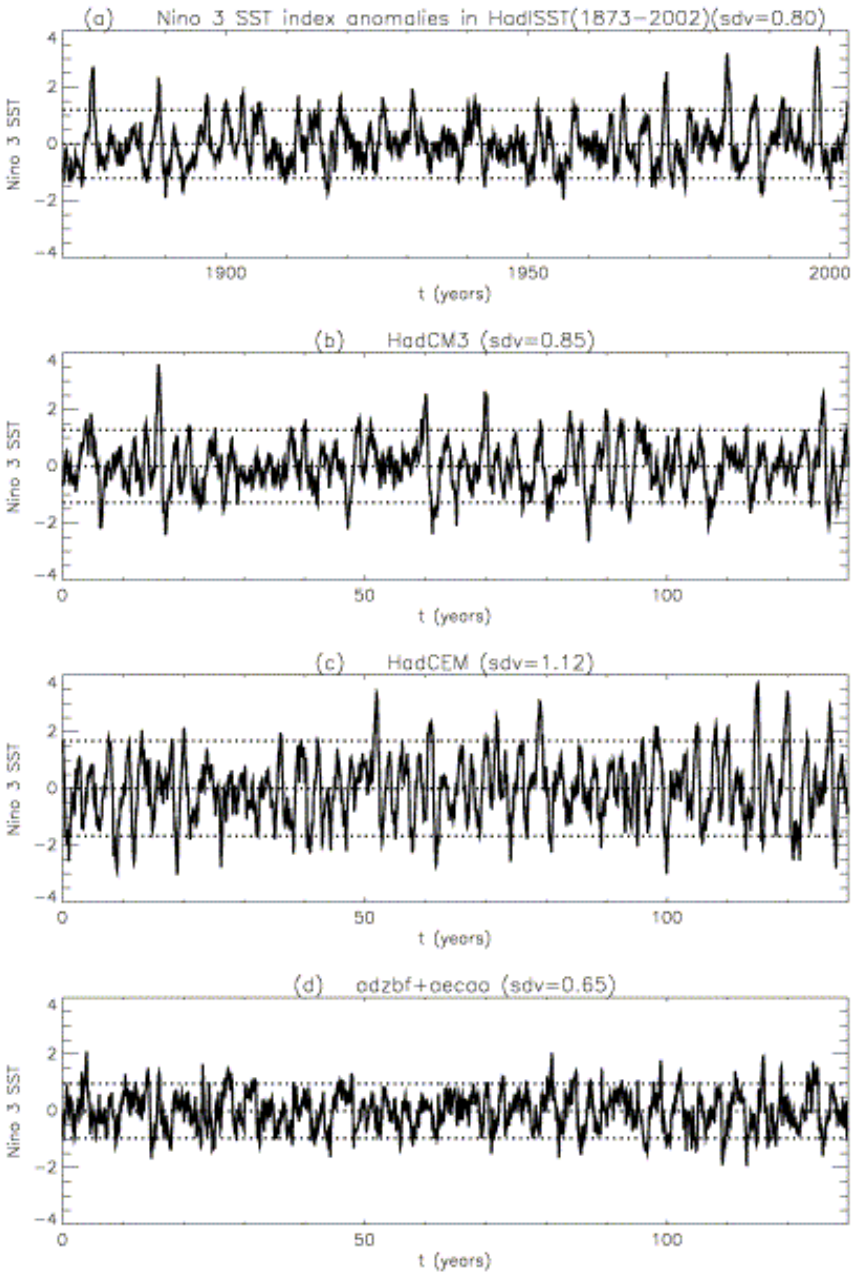

Figure 21: Monthly mean Nino 3 (5°S-5°N, 150°W-90°W) SST anomaly index timeseries from (a) HadISST 1873-2002 (b) HadCM3 (c) HadCEM and (d) HadGEM1 (adzbf+aecaa).

Most observed ENSO events begin in northern spring and peak from November to January. The annual cycle of Nino-3 SST interannual variability provides a measure of this behaviour of ENSO. The HadGEM1 simulation does not capture the observed phase-locking well (Figure 22a). Nonetheless the HadGEM1 power spectrum (Figure 22b) shows a broad peak at about 3.0-4.5 years and another at about 4-4.5 year, which is very close to the major time scale in observations.

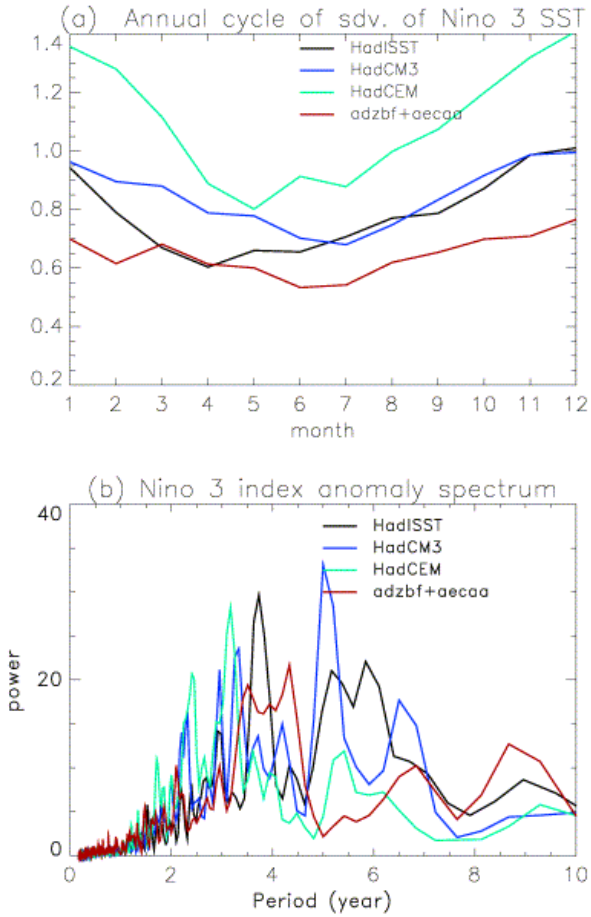

Figure 22: (a) Annual cycle of the interannual standard deviation of monthly mean Nino-3 SSTs for HadISST, HadCM3, HadCEM and HadGEM1 (adzbd+aecaa); (b) power spectra of the corresponding Nino-3 monthly mean anomaly timeseries.

Time evolution of the anomalous SST in the equatorial latitude band of 5°S-5°N in the central Pacific (Figure 23) shows westward propagation in the HadGEM1 simulation. This implies that surface processes associated with local coupled instability are responsible for the ENSO events in HadGEM1. More work is required in order to understand this.

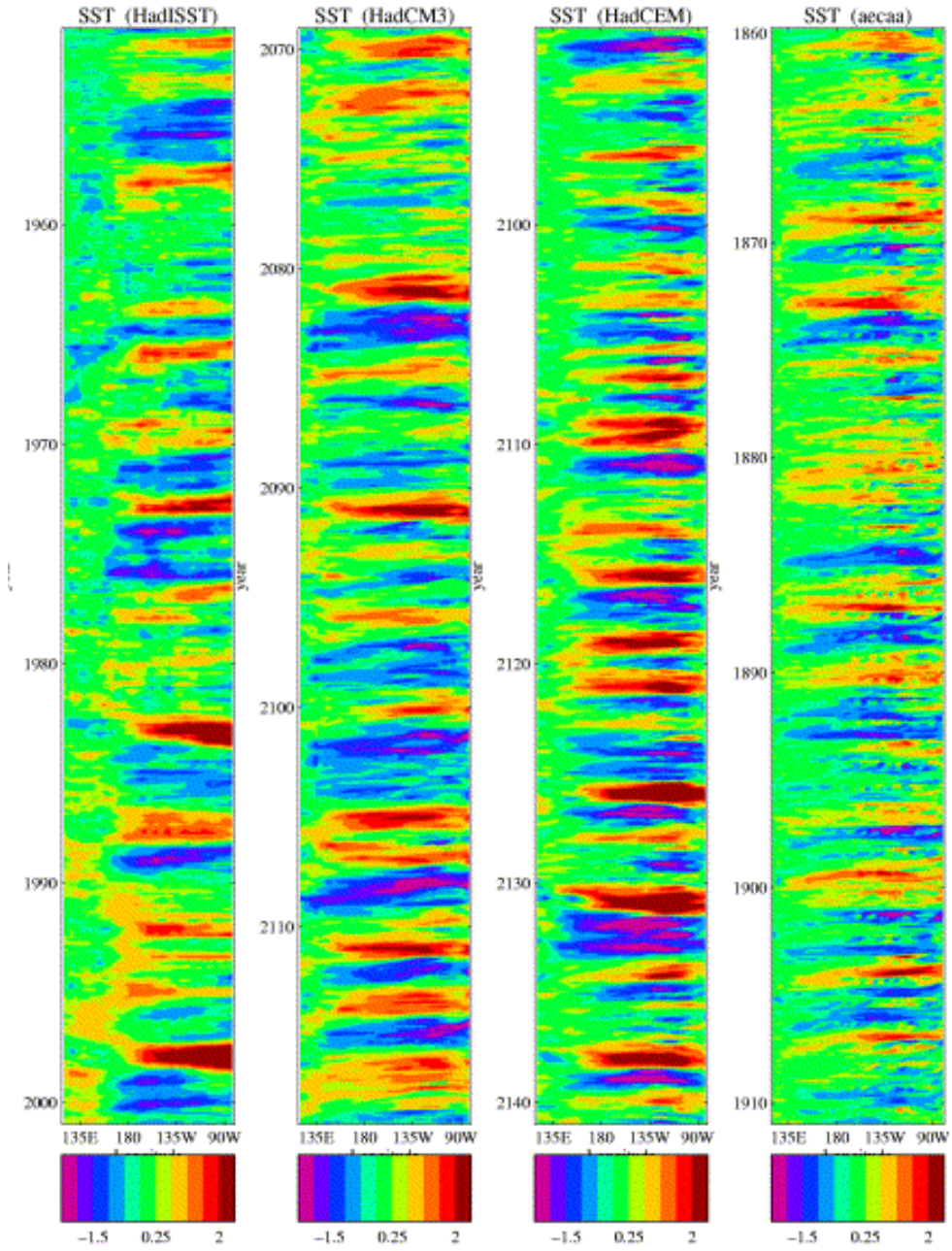

Figure 23: Time-longitude plot of SST anomalies in the equatorial Pacific (5°N-5°S) in (a) HadISST, (b) HadCM3, (c) HadCEM, (d) HadGEM1.

In Figure 24 below, warm events are defined to be those that have a December Nino 3 SST anomaly greater than 1.5 times the Nino 3 SST standard deviation. In general, the positive anomalies in the central and eastern tropical Pacific are weaker in HadGEM1 than in observations, HadCM3 or HadCEM.

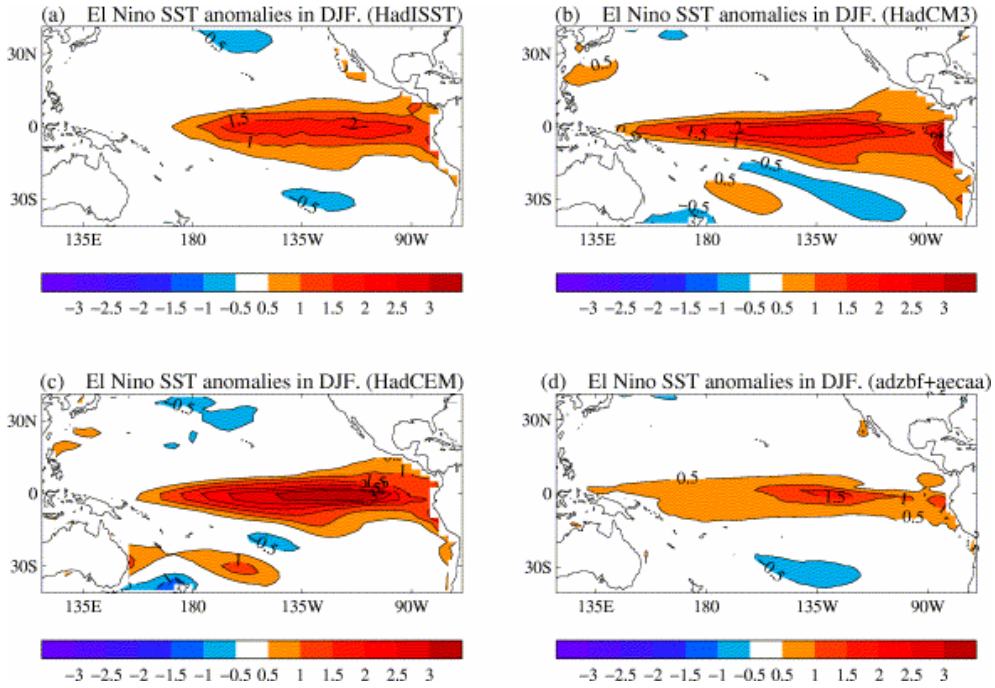

Figure 24: Composite SST anomalies for El Nino events in (a) HadISST, (b) HadCM3, (c) HadCEM, (d) HadGEM1.

NCEP analyses of composite DJF El-Nino sea level pressure anomalies indicate high pressure anomalies over the Maritime continent and low pressure over the east tropical Pacific. These pressure anomalies are reproduced more weakly in HadGEM1 (not shown), consistent with its weaker SST anomalies.

The east-west dipole structure of observed precipitation anomalies indicate that the convection maximum shifts eastward during El Nino winters. This particular feature is not captured in HadGEM1. In fact, the HadGEM1 control simulation produces enhanced precipitation at the equator and south of equator across the tropical Pacific (not shown).

The temporal evolution of subsurface temperature anomalies (Figure 25) indicates a weak role of thermocline feedback on El Nino in HadGEM1. Surface anomalies are predominantly due to the upwelling feedback. Time-longitude cross sections of composite SST anomalies (not shown, but consistent with Figure 23) reveal that SST anomalies propagate westward in HadGEM1, consistent with the dominant role of anomalous upwelling.

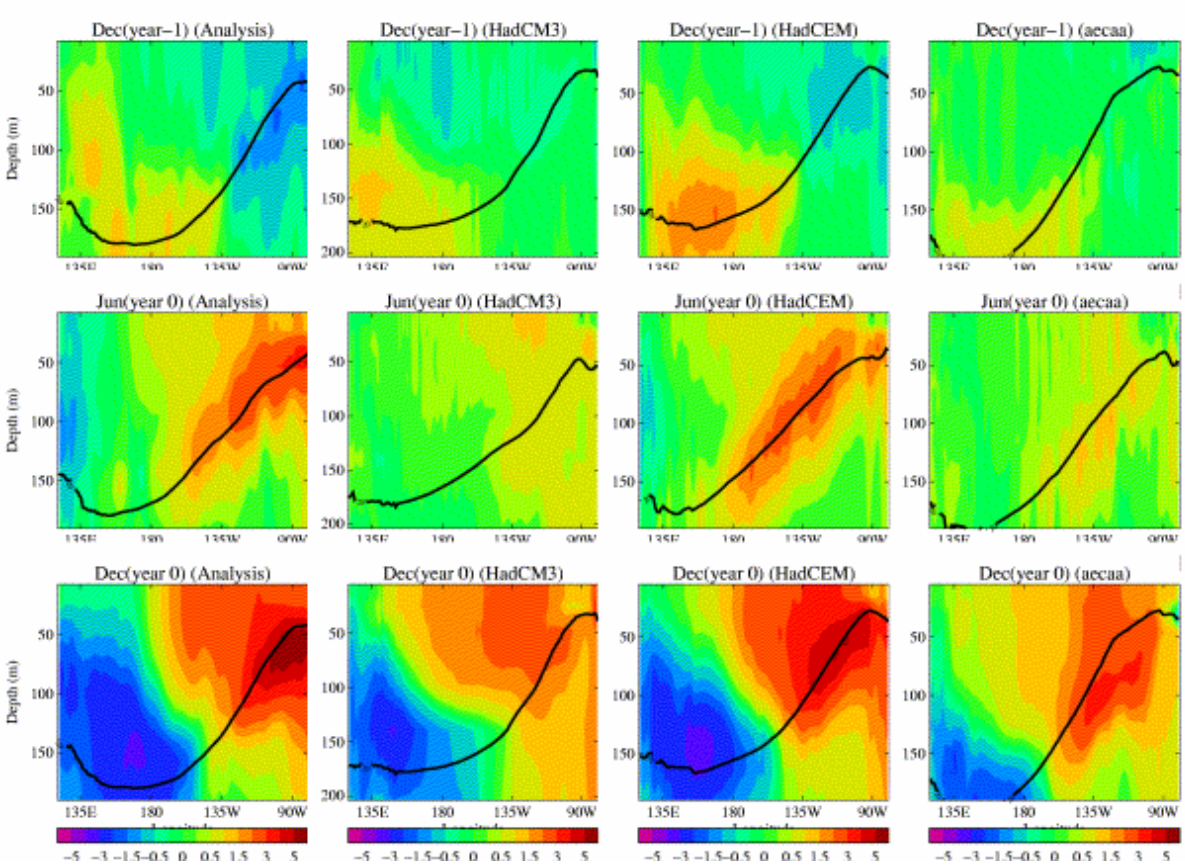

Figure 25: Evolution of upper ocean temperature anomalies (°C) and 20°C isotherm (thick line) for the composite El Nino events along the equatorial tropical Pacific (5°S-5°N).

Cloud-climate interactions during El-Nino

The simulation of clouds in HadGAM1 is detailed in by Martin et al. (2004), but there has been considerable recent interest in devising ways of testing cloud-climate interactions within models using, for example, cloud changes in response to short term forcing such as strong El Nino events. Cess et al (2001), show that the lack of a zonal SST gradient in the tropical Pacific Ocean during the 1997/98 El Nino caused a collapse of the Walker circulation and enhanced upward motion over the tropical eastern Pacific (TEP). Using satellite data from ERBE and CERES, Cess et al (2001) show these circulation changes are associated, on average, with higher level clouds in the TEP and lower clouds in the tropical western Pacific (TWP). Cess et al (2004) show that HadAM3 reproduced both the collapse of the Walker circulation and similar trends in cloud altitudes over both the TEP and TWP as seen in the satellite data. Here we show the same analysis for HadGAM1. This model also reproduces the collapse of the Walker circulation (Figure 26) between 1985 (a 'normal' year) and 1998 (a strong El Nino year) as seen in the NCEP reanalysis data (Figure 4 of Cess et al 2001). The cloud response can be characterized by the (sign-reversed) ratio of shortwave to longwave cloud forcing, N, here shown from ISCCP radiative fluxes (Zhang et al 2004) (Table 5). In a typical year, over the TWP there is a reasonable amount of compensation between SW and LW cloud forcing, but in 1998 SW cooling dominates and N increases (Table 5). In the TEP, SW cooling dominates in a typical year, but there is a strong reduction in 1998 with N being lower than in the TWP. HadGAM1 captures the shift in convection from west to east in the Tropical Pacific and simulates the changes in N realistically (Table 5)

A preliminary assessment of the degree to which these same processes are captured in the coupled model, HadGEM1 (by compositing strong El Nino events - here chosen to be events greater than 3 standard deviations), shows very little change in N in either basin (Table 5) and no evidence of a collapse of the Walker circulation in the zonal winds (not shown). This lack of response is likely to be associated with overly weak SST variability and/or a cold bias in the tropical pacific and is the subject of on-going analysis.

Model	TWP		TEP	
	'normal' year	strong ENSO	'normal' year	strong ENSO
ISCCP	1.27	1.84 (+45%)	2.9	1.63 (-40%)
HadGAM1	1.20	1.47 (+23%)	2.7	1.44 (-47%)
HadGEM1	1.29	1.25 (-3%)	3.0	2.62 (-11%)

Table 5: The value of N (see text) for ISCC-FD satellite observations (Zhang et al, 2004) for 1985 (normal year) and 1998 (strong ENSO), HadGAM1 for 1985 and 1998 and HadGEM1 for a 130-year climatology (normal year) and a composite of 2 strong ENSO events defined as events greater than 3 standard deviations away from climatology. The regions TWP and TEP are as used by Cess et al, 2001. Percentage change from normal year shown in brackets.

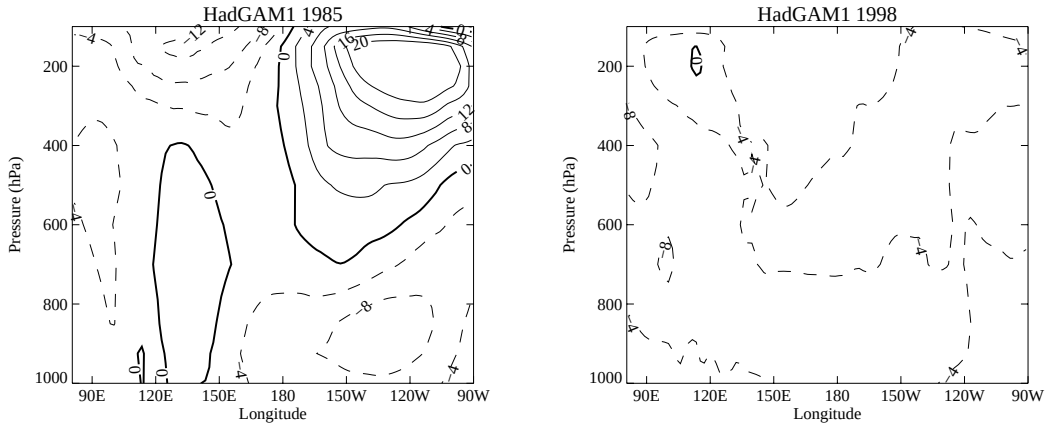

Figure 26: Pressure-longitude cross sections of zonal mean wind (ms^{-1}) averaged from 5°S to 5°N from HadGAM1 for a 4 month (JFMA) mean for a) 1985 – a 'normal' year b) 1998 – a strong ENSO year.

Indian Ocean Variability

A basic analysis of the interannual variability of the tropical Indian Ocean with particular reference to the Indian Ocean Dipole (IOD) or Zonal Model has been completed using 52 years of integration from the HadGEM1 spin up, in comparison with HadCM3 and observed SSTs from HadISST. This analysis builds on the comprehensive diagnosis of 3 coupled models HadCM3, HadCEM and HadCEML described in Spencer et al. (2004). At this stage only the SST has been diagnosed and no subsurface fields have been analysed.

Figure 27 shows the seasonal mean interannual variability in tropical SST. As expected, El Nino is the dominant factor in the observations and to a large extent in HadCM3. In HadGEM1, however, El Nino variability appears to be somewhat reduced and the seasonality, with maximum variance in MAM, is wrong. As in HadCM3, the SST variability in the subtropics of the north Pacific and southern Indian Ocean is greatly overestimated for reasons that are unclear at present. In the equatorial Indian Ocean, HadGEM1 has a high level of variability along the coasts of Java and Sumatra during JJA and SON, indicative of an overactive Indian Ocean Dipole.

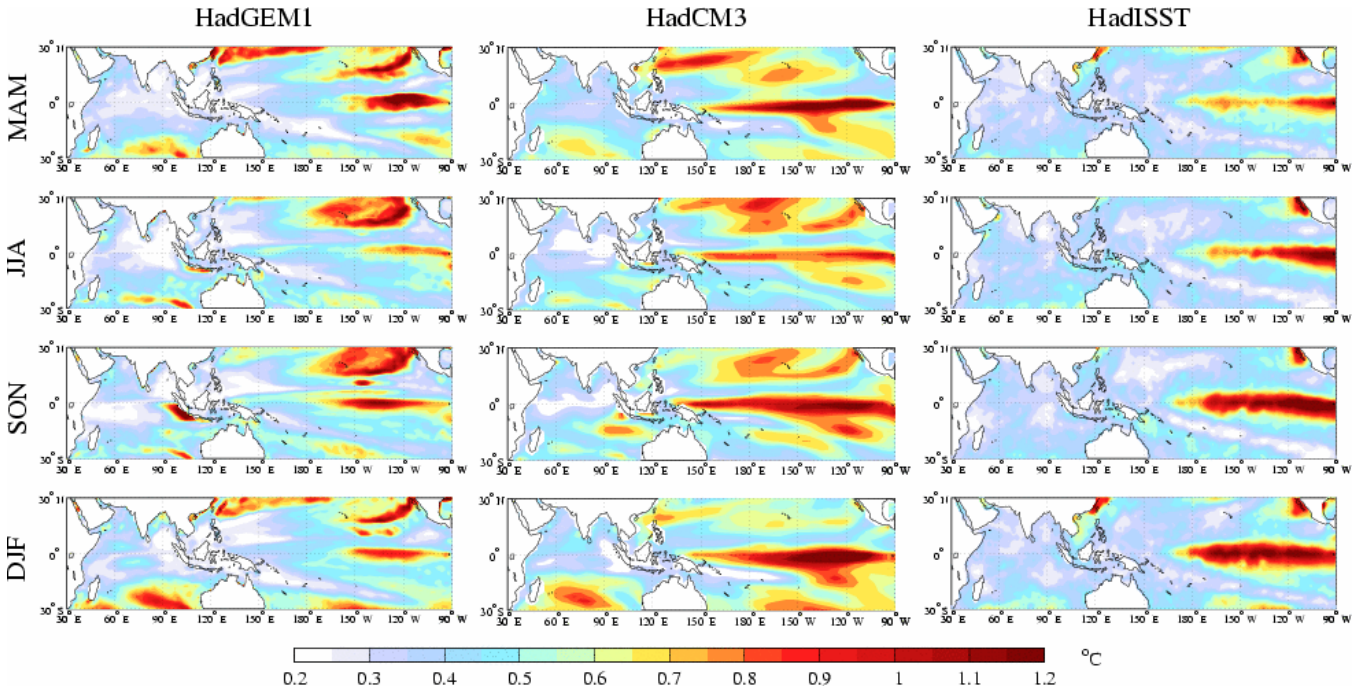

Figure 27: Standard deviation of the seasonal mean interannual variability in SST (K).

The temporal behaviour of the IOD is shown in Figure 28, where an index based on the difference in SST between the west and south-east tropical Indian Ocean is plotted for the observations (top panel), from HadGEM1 (middle panel) and HadCM3 (bottom panel). Note the change in scale for HadGEM1. Overall the comparison with observations is better for HadGEM1 than HadCM3. There are more extreme peaks, well separated by weak variability, and little evidence of recurring IOD events from year to year, which were an undesirable feature of HadCM3. However, the seasonality of the IOD is even more marked in HadGEM1 (Figure 29) suggesting a strong positive feedback between the south-easterly winds along the coast of Sumatra, coastal up-welling and cooler SSTs during SON.

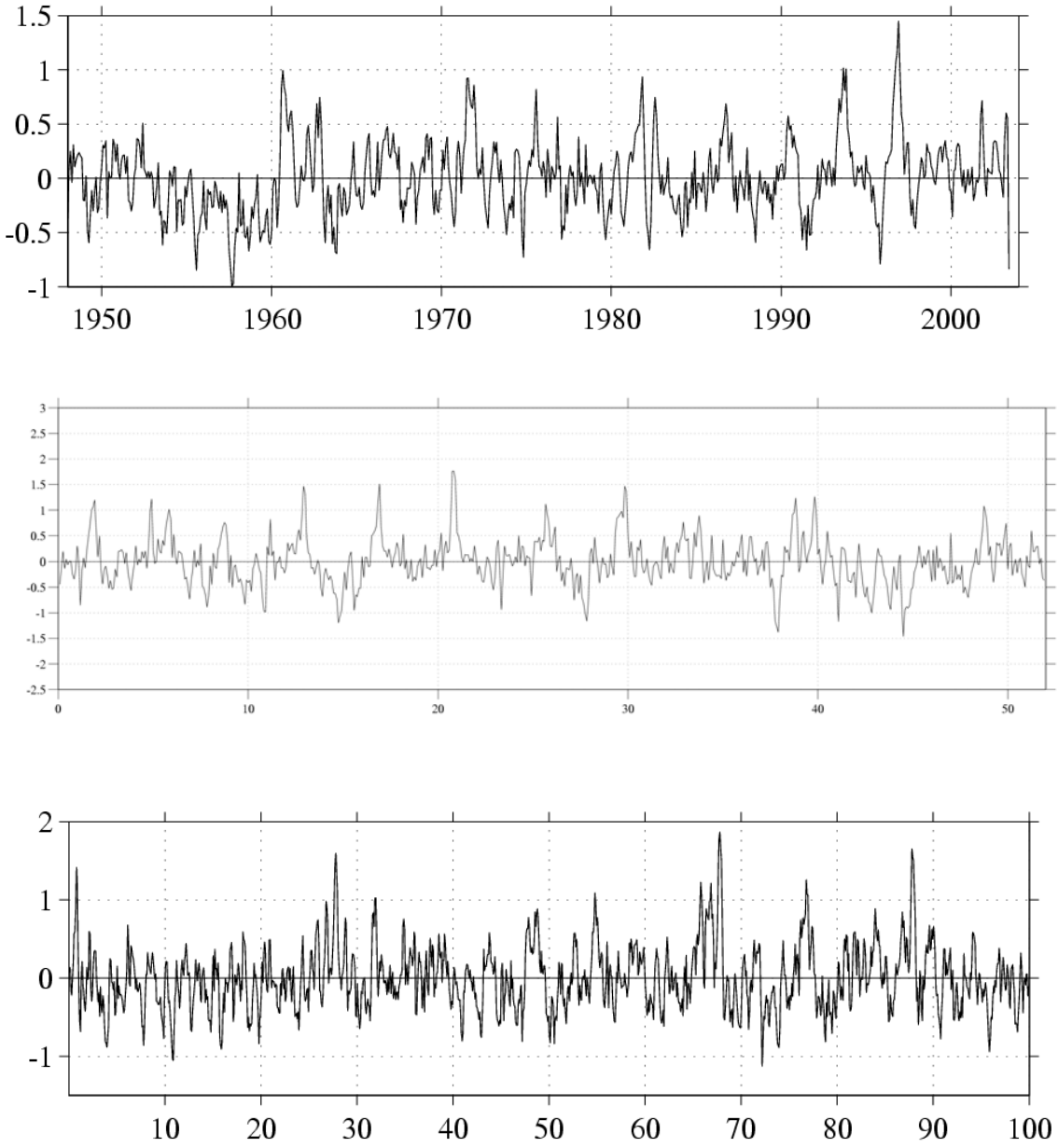

Figure 28: Indian Ocean Dipole Mode index from HadISST (top), HadGEM1 (middle) and HadCM3 (bottom). The Index is based on the difference in SST between the west and south-east tropical Indian Ocean.

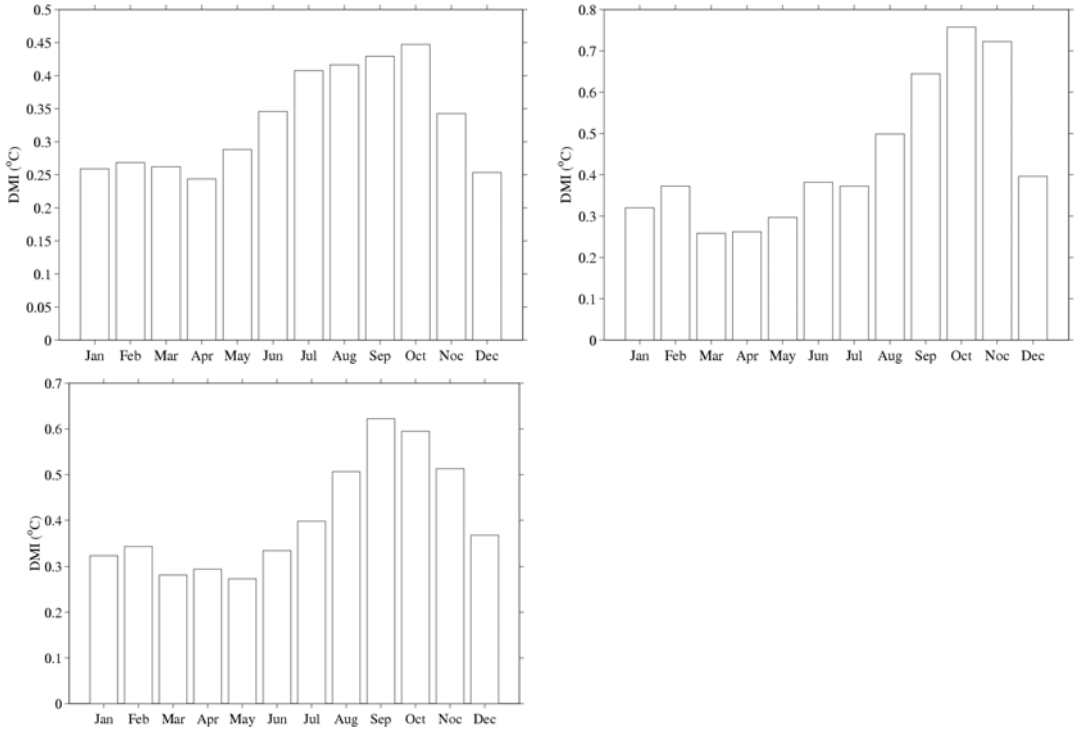

Figure 29: Seasonal variation in the amplitude of the Indian Ocean Dipole Mode index from HadISST (top left), HadGEM1 (top right) and HadCM3 (bottom). Note that the vertical scales vary.

The IOD has a strong association with El Nino in observations (Figure 30, top panel). The atmospheric teleconnections into the Indian Ocean region give rise to a basin-wide warming, which is evident in the large, positive correlations between Nino3.4 and the western node of the IOD in the observations. In contrast, the correlation between Nino3.4 and the western node of the IOD is very weak for most of the year, particularly in spring, suggesting that the remote effects of ENSO are not as well captured in HadGEM1 as in HadCM3. It is worth noting that the lack of correlation between Nino3.4 and the Indian Ocean during the Asian Summer Monsoon season in HadCM3 can be substantially improved when the systematic SST errors in the West and central Pacific are reduced (Turner et al. 2004).

Both models capture the strong negative correlation between El Nino and the SSTs in the south-east Indian Ocean – the S.E. node of the IOD. Overall the relationship between ENSO and the IOD is represented to some extent in both models with the strongest correlations occurring towards the end of the year. However the abrupt decline in correlation is not well captured suggesting that the termination of the IOD by the seasonal reversal of the monsoon winds is not well simulated in either model.

Further research is planned to explore the vertical structure of the Indian Ocean in the model and the characteristics of the ocean waves that contribute to the IOD and to Indian Ocean variability in general. The earlier study of Spencer et al. (2004) suggested that enhanced vertical resolution and the proper representation of the islands of Java and Sumatra, are key to capturing the IOD. Both these elements are present in HadGEM1.

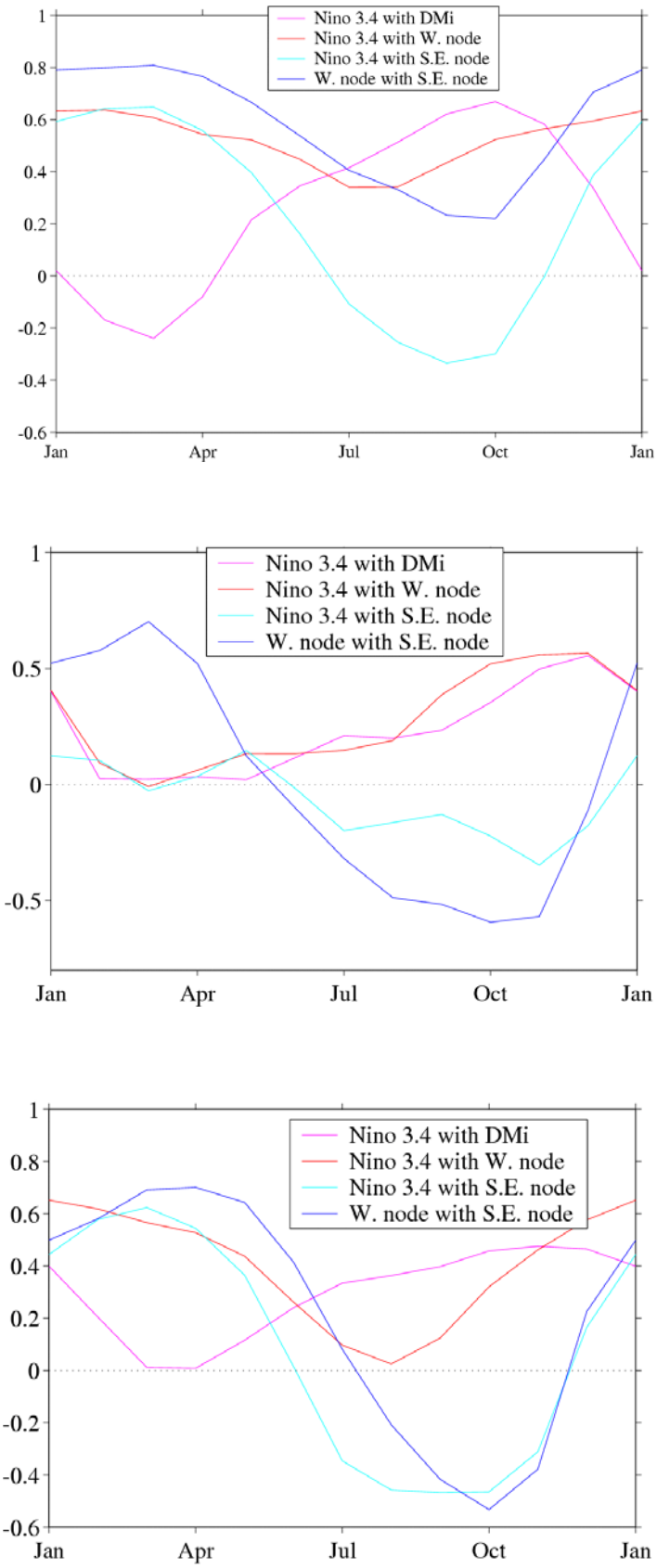

Figure 30: Seasonal evolution of the correlations between ENSO and aspects of the Indian Ocean Dipole Mode from HadISST (top), HadGEM1 (middle) and HadCM3 (bottom).

4.5 Assessment of overall model skill scores

There is currently no universally accepted objective method of defining the overall skill of one coupled model against another in reproducing observed climate. While it is to some extent desirable and useful to have such objective measurement methods, the practical difficulty in tuning a model to be skilful across all likely applications means that the associated metrics used in such measurements will contain an element of prior judgement in the choice of variables used and their relative weightings, as well as the observational sources and errors adopted, in the statistical assessment. Nonetheless, in developing HadGEM1 we made use of a simple weighted measurement of rms errors compared to climatological means of a selection of multi-year mean fields (of monthly, seasonal and annual data) taken from the model. These cover the atmosphere, land surface, air-sea fluxes, sea ice and ocean. The basis of the statistical skill score is the Climate Prediction Index (CPI) devised by D. Sexton (see supplementary material in Murphy et al., 2004 for details of the method).

The CPI was used primarily during the development and tuning phase to quantify improvements or otherwise in model performance as a result of changes, supported by more detailed examination of fields. The CPI breakdown for the final version of HadGEM1 compared to HadCM3 (Figure 31) reveals improvements in the majority of the elements, particularly cloud-related fields, but with some notable exceptions such as 1.5m temperature and precipitation.

Taken overall, the weighted CPI score for HadGEM1 is considerably better than for HadCM3 (Table 6). Although the choice of weighting of the individual elements has an effect on the magnitude of this improvement, we decided not to tune the weightings beyond those already made when the CPI was designed for other purposes. Therefore we consider it justifiable to say that the new model possesses better overall skill in the simulation of mean climate, in a quasi-objective sense.

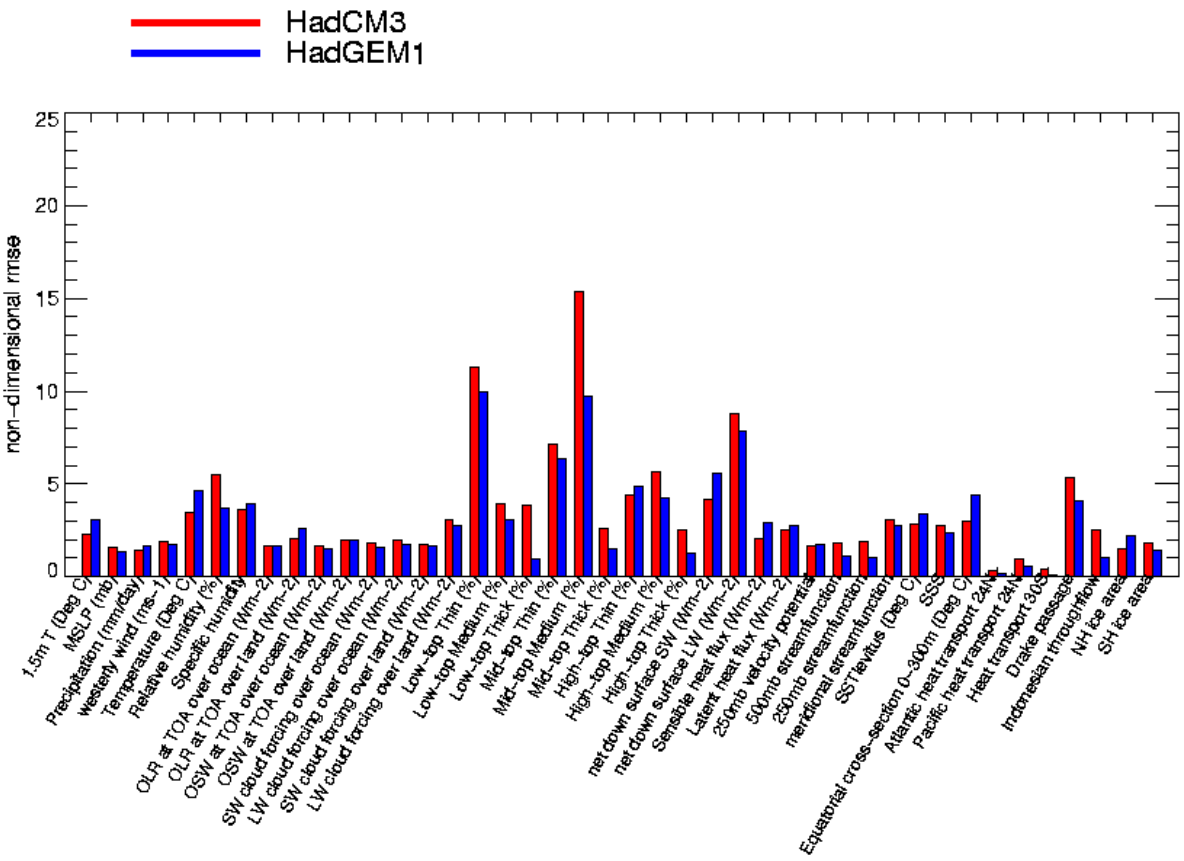

Figure 31: Comparison of non-dimensional rms error metrics for individual elements in the Climate Prediction Index (CPI) from HadCM3 (red bars) and HadGEM1 (blue bars) based on the 4th decade of the spin up with each model.

Model	Non-dimensional rms error	Bias	Correlation	Ratio of standard dev
HadCM3	3.335	8.943e+07	0.801	1.546
HadGEM1	**2.931**	**2.093e+07**	**0.824**	**1.245**

Table 6: CPI weighted absolute statistics for HadGEM1 and HadCM3 (the better score is in bold).

5 Climate sensitivity and response in idealised experiments

Slab experiments

The climate sensitivity of a model, defined as the difference in global mean surface temperature between a $2xCO_2$ simulation at equilibrium and a control, is widely regarded as a leading order measure of the response of a climate model. Due to the computing cost using a full coupled model, the climate sensitivity is more normally calculated using an atmosphere-mixed layer ocean version of the model. Figure 32 shows the time series of global mean surface temperature in such an experiment using HadGSM1 compared to HadSM3. Using the equilibrium period of the $2xCO_2$ run, and all of the control except the first 5 years, a climate sensitivity of 4.3K is obtained for HadGSM1. This is significantly higher than the climate sensitivity of HadSM3, which is 3.3K. The geographical pattern of response is similar, to first order, in both models (Figure 33), particularly at low latitudes (greater warming over land and at higher latitudes, minimum in warming over the south east Pacific, greater warming off the Californian coast, etc.). The enhanced warming in HadGSM1 is over areas of sea ice, in particular the Antarctic sea ice region. Further analysis reveals that the difference is mainly in the clear-sky shortwave, suggesting that a different sea ice albedo feedback is responsible. Interestingly, the global mean (and to some extent the geographical pattern) of the cloud response is reasonably similar in the two models despite the significant differences in the physical parametrizations and cloud simulations in the control.

A comparison of the sea ice extent in the control versions of the slab and coupled models suggests that the Antarctic summer sea ice extent is somewhat larger in HadGSM1 than HadGEM1. This implies the coupled model should have a weaker sea ice albedo feedback, and hence a slightly smaller climate sensitivity, than estimated by the slab model. However, the Arctic sea ice extent is similar in both the coupled and slab models suggesting that the new sea ice scheme is indeed more sensitive than that in HadCM3/HadSM3. Hence we expect HadGEM1 to be more sensitive than HadCM3. This result emphasises the importance of having as similar a sea ice scheme as possible in a slab model as in the fully coupled model. Analysis of HadSM3 and HadCM3 reveals that the slab model contains less Antarctic ice in the control than in the coupled model, leading to a weaker albedo response in HadSM3. This suggests that the climate sensitivity of HadCM3 is underestimated by HadSM3 (consistent with the higher estimate of HadCM3's climate sensitivity derived found by Gregory et al. 2004); and this also contributes to the difference in the Antarctic sea ice region in Figure 33 being so large.

In summary, the climate sensitivity of HadGSM1 is 4.3K which is significantly higher than HadSM3, mainly due to an enhanced sea ice albedo feedback. We expect HadGEM1 to be *slightly less* sensitive than HadGSM1 due to the sea ice extent being less in the coupled model control run. On the other hand, several pieces of evidence suggest that HadCM3 is *more* sensitive than estimated by HadSM3, so the difference between the two coupled models might be smaller.

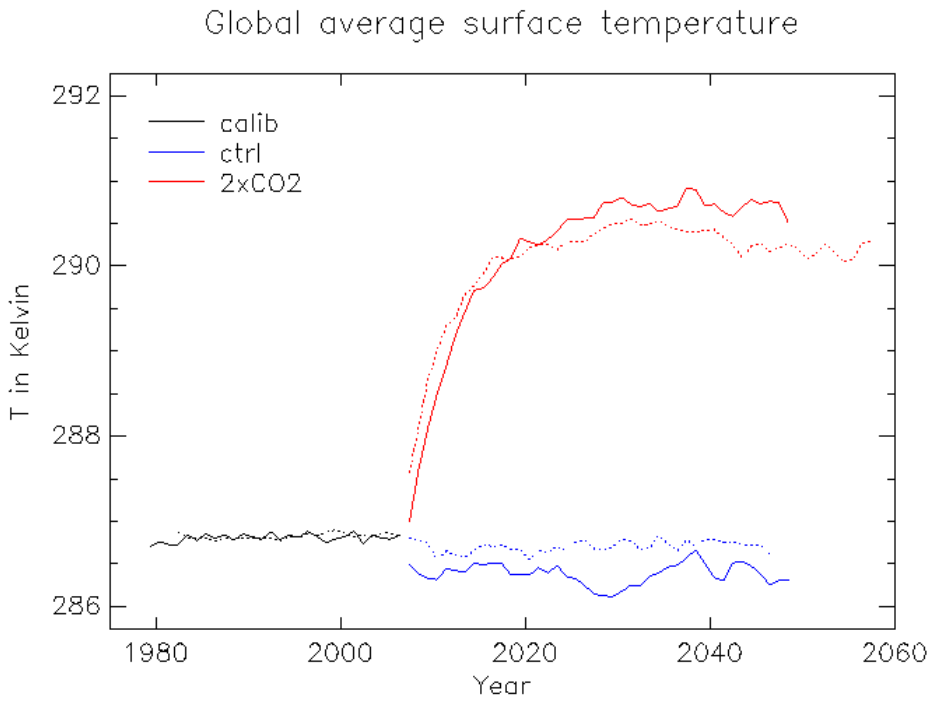

Figure 32: Time series of global annual mean 1.5m temperature (K) for HadGSM1 (solid) and HadSM3 (dotted), calibration (black), control (blue) and 2xCO2 (red) simulations.

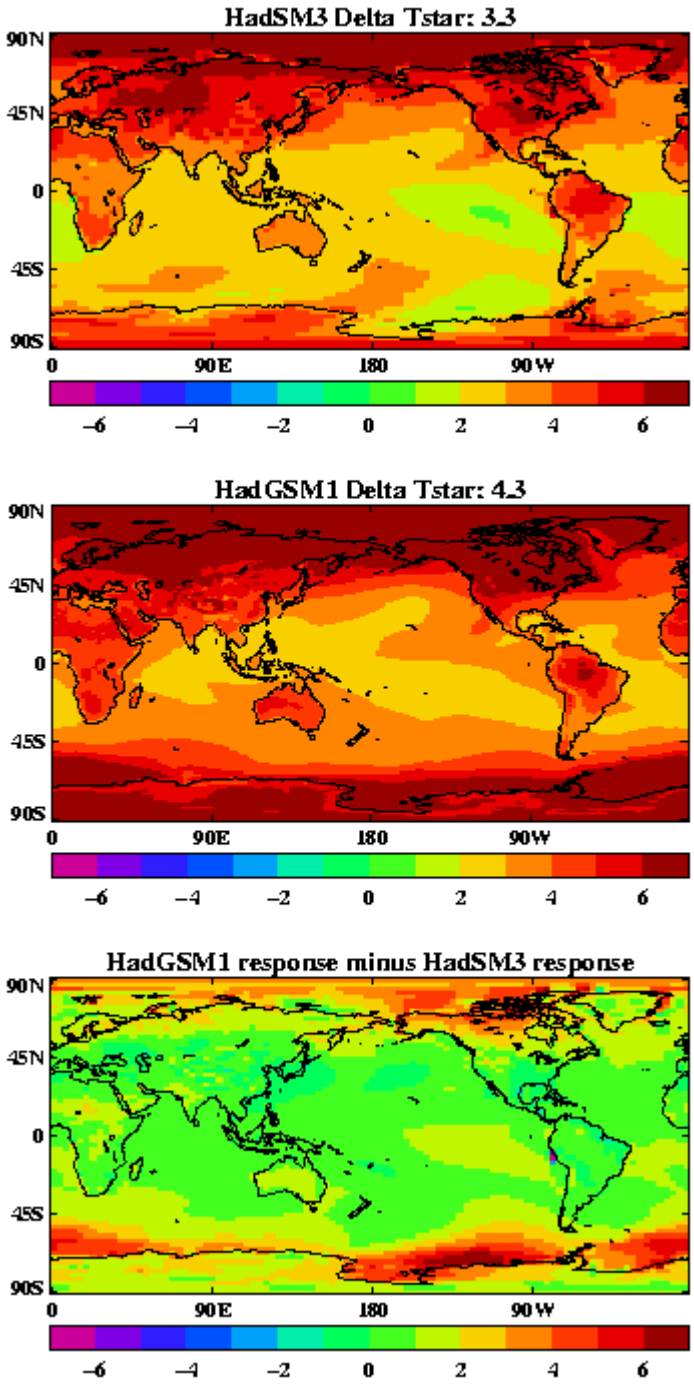

Figure 33: Change in 1.5m temperature (K) in response to a doubling of CO_2 in HadSM3 (top), HadGSM1 (middle) and the difference in response (bottom).

1%-per-year CO_2 coupled experiment

In the HadGEM1 control run the drift in global mean 1.5m surface temperature over the first 70 years is around -0.12 K per century, compared with the HadCM3 drift of +0.05 K per century. The global mean 1.5m surface temperature response in the 1% experiment ('adjusted' for the linear drift in the control experiment) is a near linear increase, reaching

approximately 2 K by year 70 (Figure 34), which is very similar to the response in the equivalent HadCM3 experiment.

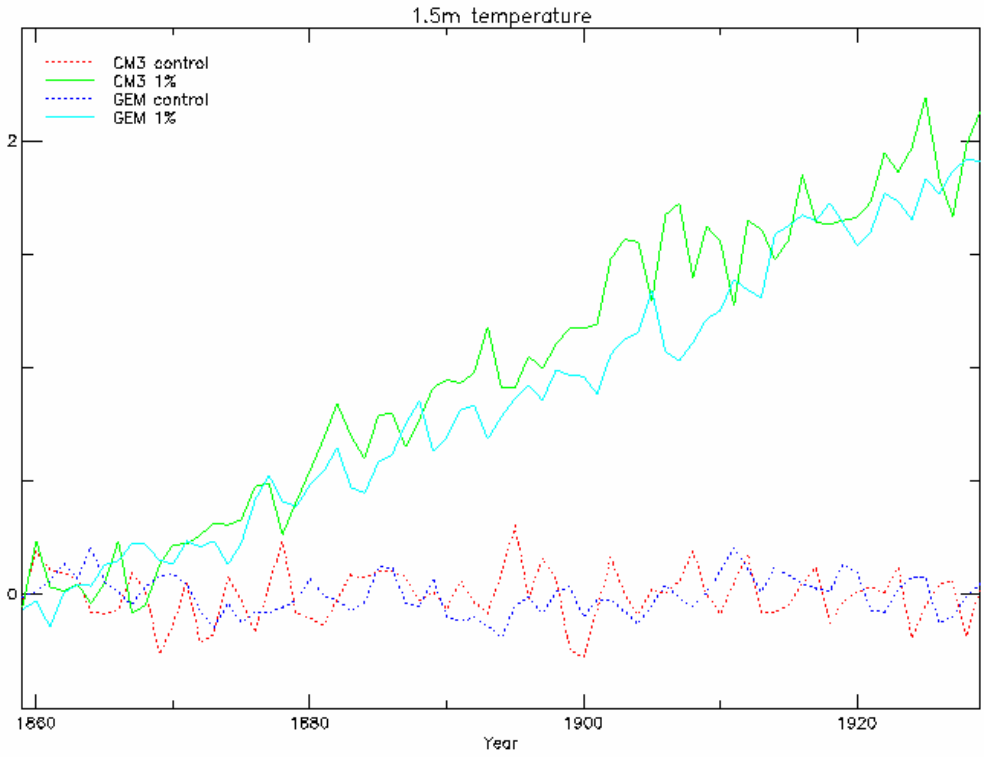

Figure 34: Time series of global mean 1.5m temperatures in the HadGEM1 and HadCM3 1% experiments with the linear control drift removed from the control and 1% simulations. The drift-adjusted control runs illustrate the variability.

The spatial pattern of warming for the 6th decade (Figure 35) contains many of the features seen in HadCM3, and in other climate models (Cubasch et al., 2001), including an enhanced polar warming and a greater warming over land than over the sea. The mean changes over this decade in HadGEM1 and HadCM3 are similar at 1.4 K and 1.6 K respectively. However, the range of temperature changes is greater in HadGEM1 at 10.5 K compared to 8.7 K in HadCM3. The largest differences in the spatial pattern of warming over the ocean occur over the Arctic, where HadGEM1 has greater warming, and over the North Atlantic to the south of Greenland, where HadCM3 warms more. There are also some sizeable differences over parts of the Pacific and around the coast of Antarctica. Apart from the high northern latitude continents, warming over land is lower in HadGEM1 and the value of the land-sea contrast in the 6th decade is 1.6 in HadGEM1 compared to 1.8 in the HadCM3 experiment.

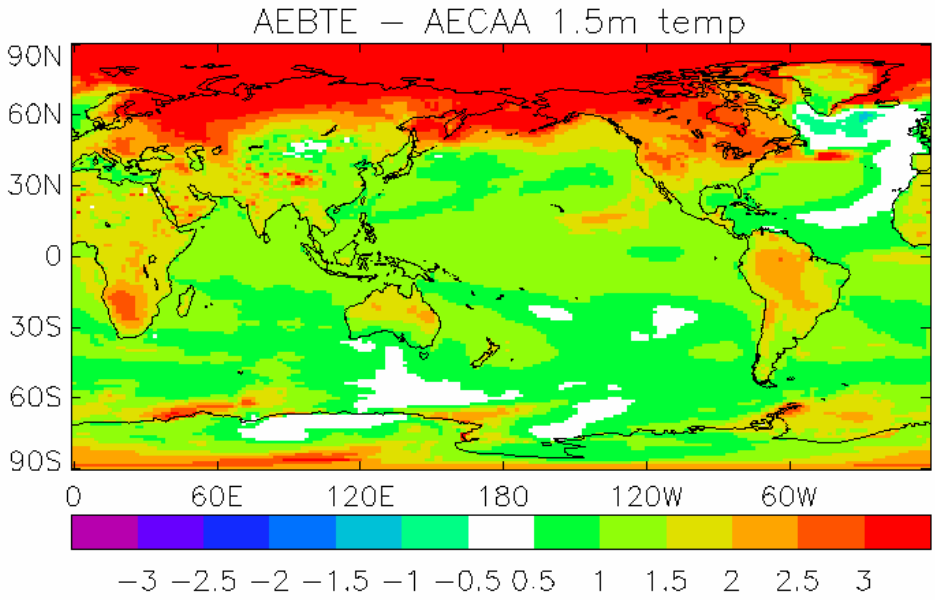

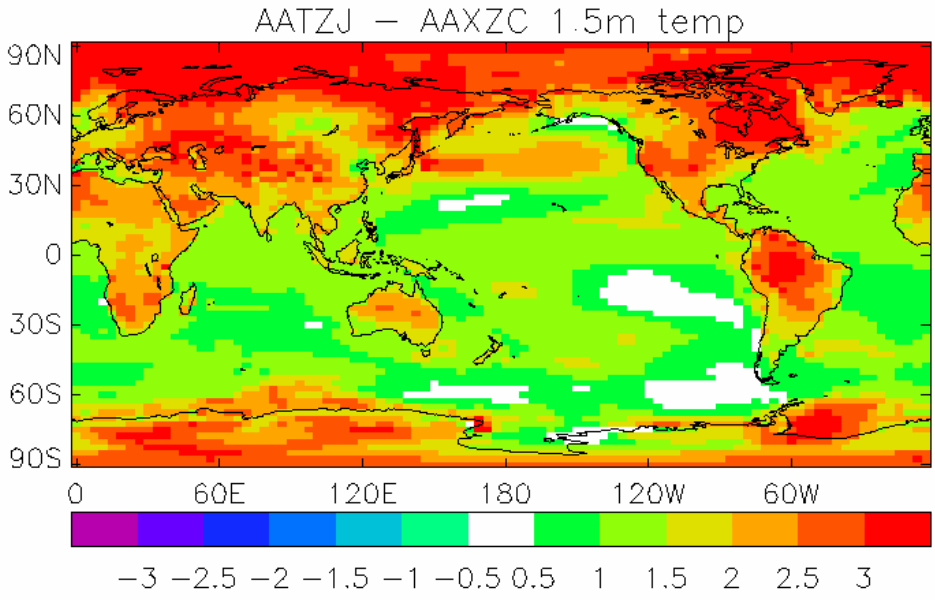

Figure 35: The spatial pattern of warming (K) in the 1% experiments relative to the control simulations for HadGEM1 (upper) and HadCM3 (lower) for decade 6.

Changes in the global net TOA radiative imbalance are shown in Figure 36. In the 1% case it has increased by around 1.2 Wm^{-2} by the 7th decade for both HadGEM1 and HadCM3 experiments. Averaged over the entire timeseries, the TOA flux anomaly is approximately 0.1 Wm^{-2} greater in HadGEM1 than in HadCM3. The ocean component of the HadGEM1 model receives most of the extra heat added to the system by the TOA imbalance in the 1% simulation (Figures 37 and 38). While the upper ocean warming is slightly less in HadGEM1 than in HadCM3, the total heat uptake in HadGEM1 is slightly greater, indicating that HadGEM1 is taking up more heat at depth. Figure 37 shows a larger potential temperature anomaly at the deepest levels in the southern hemisphere in HadGEM1 than in HadCM3, accompanied by a rather different anomaly in global mean overturning circulation.

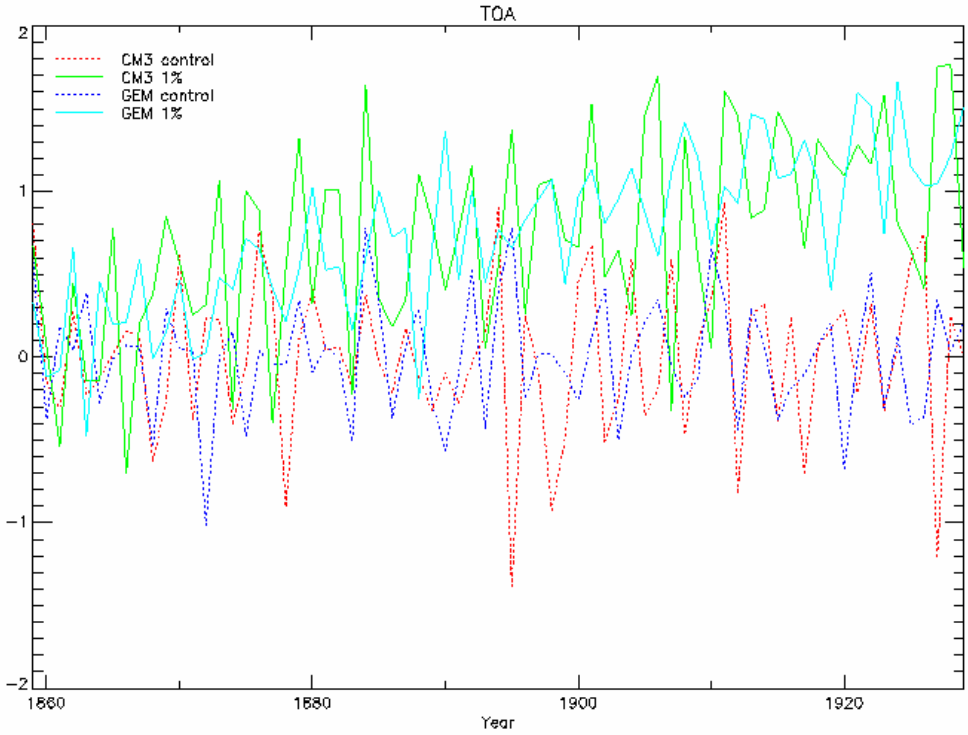

Figure 36: Time series of global net top-of-the-atmosphere radiative imbalance (W/m^2) in HadGEM1 and HadCM3 1% simulations relative to the control simulations. A linear trend has been fitted to the time series of each control simulation and removed from both the control and relevant 1% simulation results.

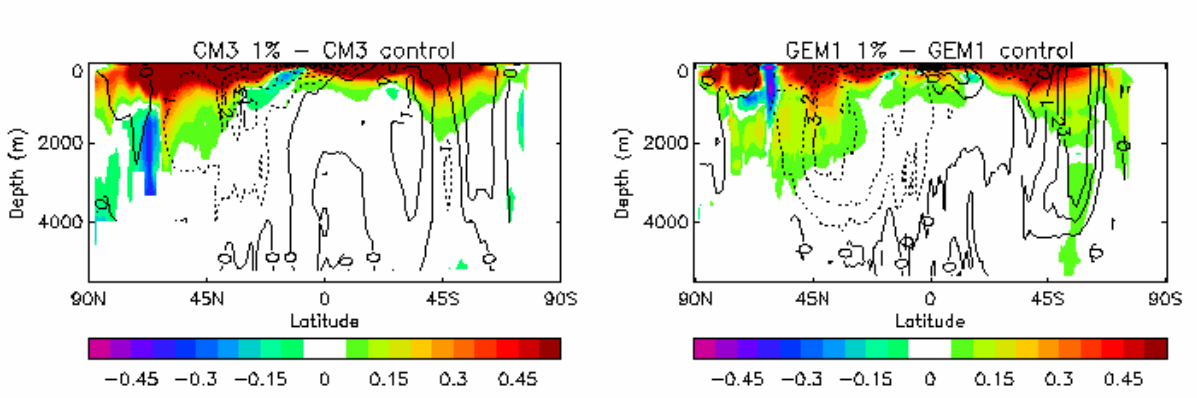

Figure 37: Ocean warming and circulation changes in the 1% run. Colours show the global zonal mean potential temperature anomalies (K) with depth for the 6th decade of the 1% runs relative to their control. The overlaid contours show the changes in global overturning circulation (Sv).

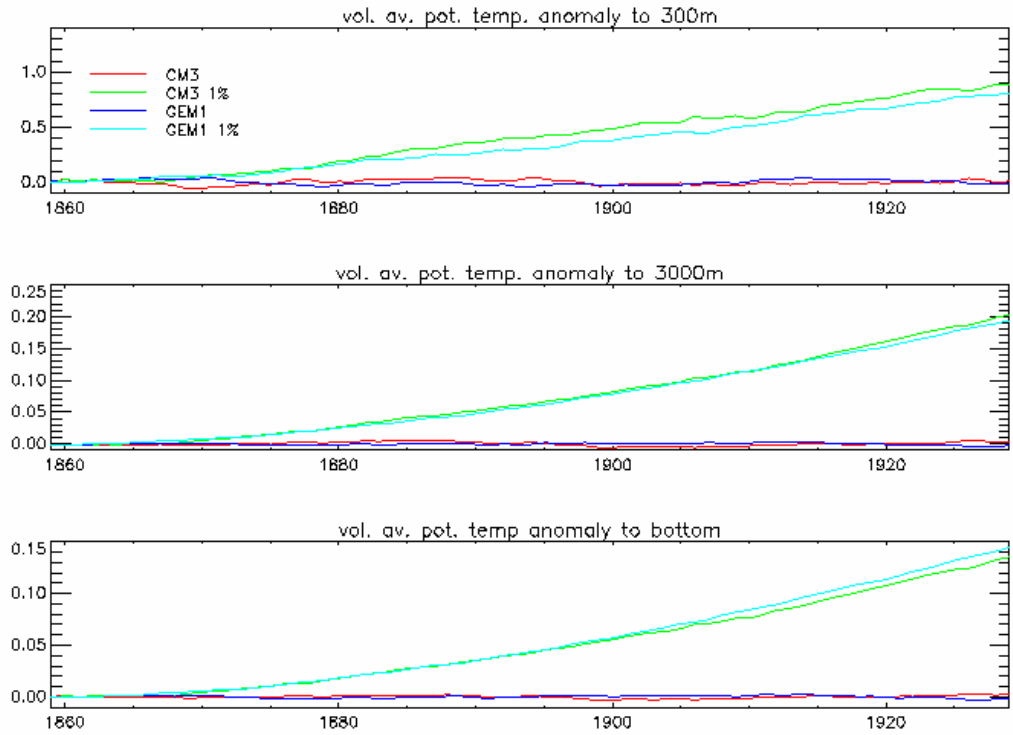

Figure 38: Time series of global ocean heat uptake, in terms of changes in volume averaged potential temperature (K), in the HadCM3 and HadGEM1 1% runs relative to their control (the linear trend in the control simulations has been removed from the control and relevant 1% results). The trends are shown for the surface-300m layer (upper panel), the surface-3000m layer (middle panel) and surface-bottom of ocean (lower panel).

The geographical pattern of heat uptake in HadCM3 and HadGEM1 (not shown) appears most similar in the southern hemisphere, with a sizeable contribution in both models occurring along the Antarctic circumpolar current. A notable difference in the southern hemisphere is the absence in HadGEM1 of heat uptake to the north east of Australia. The models are qualitatively less similar in the northern hemisphere. The large heat uptake in the Pacific gyre in HadCM3 does not occur in HadGEM1, and there are large differences in the Atlantic heat uptake patterns. The differences in Atlantic heat uptake in the two models are likely to be related to the different changes in overturning circulation (see contour lines on Figure 40).

The time series of maximum strength of the Atlantic overturning circulation at 40^{o}N is shown in Figure 39 for the spin up/control simulations of HadCM3 and HadGEM1 and for the 1% simulations. The 1% simulations for both models show a decrease in overturning as the simulations progress, but the HadGEM1 1% decrease is more clearly evident at an earlier stage to that of the HadCM3 simulation (the variability in the overturning is also large and the differences between the models may not be significant). Figure 40 shows the anomalies in Atlantic zonal mean salinity between the 1% and control simulations for the 6th decade of HadGEM1 and HadCM3, with the contours of overturning anomalies superimposed. The overturning anomalies show that the differences in overturning response at 40N shown in Figure 39 correspond to more wide-scale differences in response over the basin. The anomalies in zonal mean Atlantic salinity also show differences between the HadCM3 and HadGEM1 simulations with much more freshening evident in the higher northern latitudes in HadGEM1 than in HadCM3. The mechanisms controlling the thermohaline circulation in HadCM3 were investigated in detail by Thorpe et al. (2001) and we are now studying those in HadGEM1.

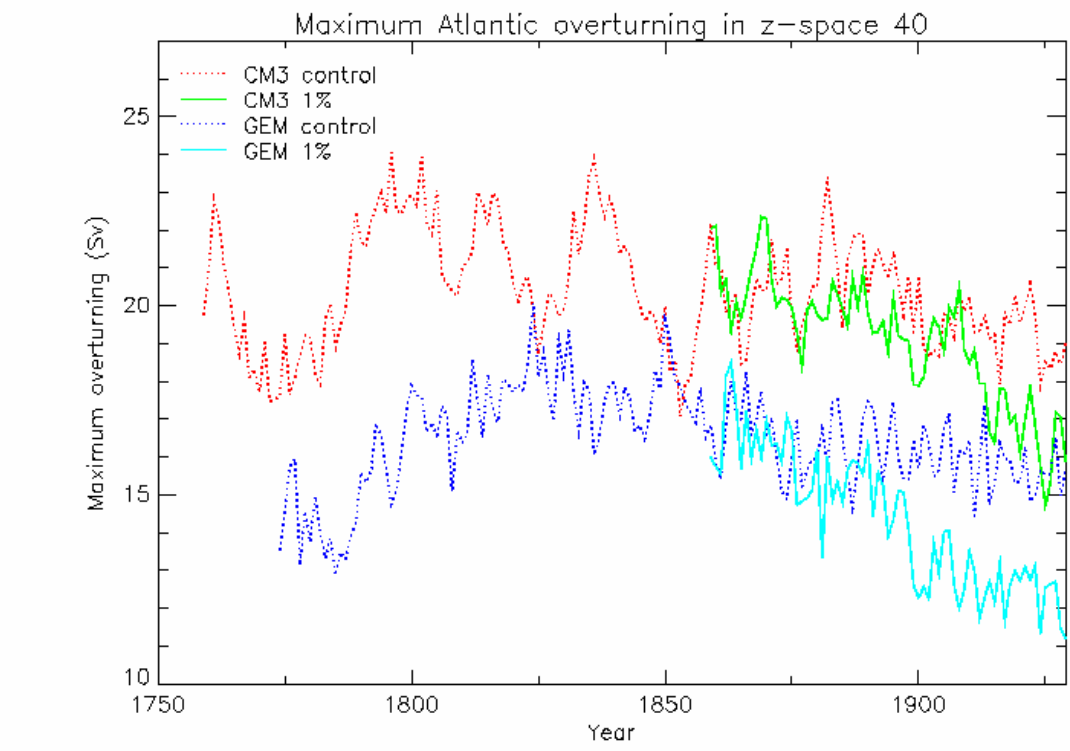

Figure 39: Time series of maximum Atlantic overturning at 40°N (Sv) for the spin up/control HadCM3 and HadGEM1 simulations and the 1% simulations. Note: the 1% curves have not been drift-adjusted.

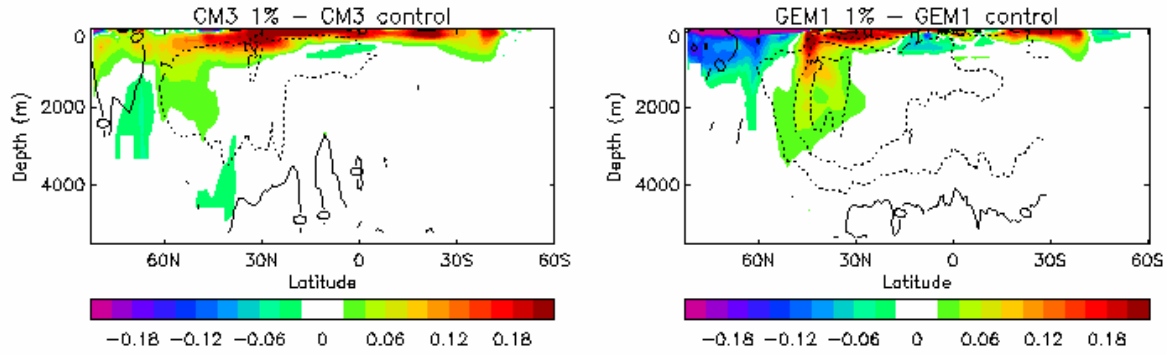

Figure 40: Atlantic zonal mean cross sections of salinity anomalies (psu) in the HadCM3 and HadGEM 1% simulations relative to the control for the 6th decade. Overturning streamfunction anomalies are overlaid.

The ocean and atmosphere changes also lead to significant reductions in sea ice area and thickness in both the northern (Figure 41) and southern hemispheres (not shown). In the northern hemisphere, the decreases in ice depth in the HadGEM1 1% simulation relative to its control are greater than the corresponding decreases in the HadCM3 model. The model

differences result from a combination of differences in the control sea ice distribution and in the ocean and atmosphere warming, and are likely to be partly due to there being a different representation of sea ice in the two models.

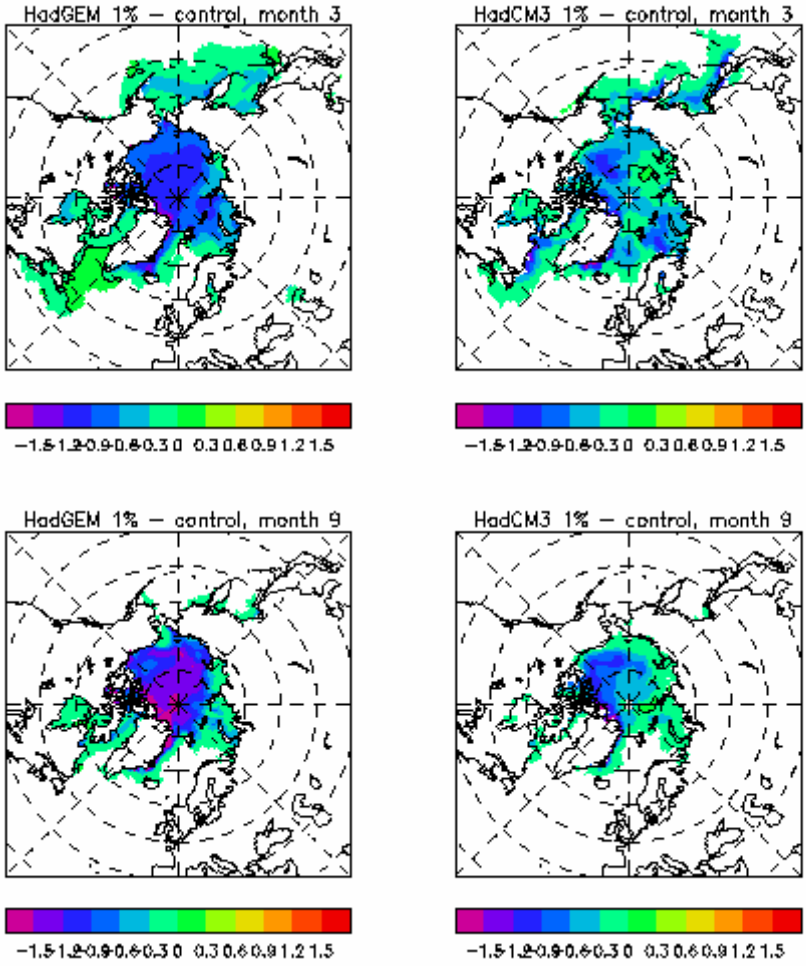

Figure 41: Northern hemisphere sea ice depth anomalies (m) in the HadGEM1 and HadCM3 1% simulations relative to the control for the 6th decade March (upper panels) and September (lower panels) means.

6 Concluding discussion

We have documented the new Hadley Centre climate model HadGEM1, and have evaluated its performance against its predecessor HadCM3 and observed climatologies. We have conducted a preliminary experiment with the model consisting of a set of runs designed to meet the objectives of the forthcoming IPCC Fourth Assessment Report, and at the same time the EU ENSEMBLES project. Some of the runs are still in progress so results discussed in this paper are to some extent preliminary.

The new model performs well, and in an overall quasi-objective sense outperforms HadCM3 in representing the mean climate. Despite some remaining problems which are the subject of future work, including in particular its representation of the tropics and some aspects of tropical variability, HadGEM1 is expected to provide a significant step forward for climate model development and experimental capability for the Met Office, continuing the Unified

Model strategy within the framework of the New Dynamics (ND). As shown in an accompanying paper by Martin et al. (2004), the atmospheric performance in HadGEM1 is better than in HadCM3 in important aspects, benefiting in part from ND but also particularly from improvements in the representation of clouds and their effect on the radiation budget through the depth of the atmosphere. HadGEM1 also contains a much more advanced representation of sea ice dynamics and physics. Both of these advances give reason to believe that HadGEM1 will provide more reliable climate change simulations.

HadGEM1 is already being used as a basis for the development of a higher resolution coupled model known as HiGEM, in a project sponsored by the UK National Environmental Research Council (NERC) and led by the University of Reading. This collaborative project involves several university partners and the Hadley Centre, and aims to deliver a community model as well as to help coordinate the understanding and improvement of the model by a wide user community, particularly regarding its systematic errors.

In keeping with the original design concept, versions of HadGEM1 are already being extended to encompass coupled climate, chemistry and ecosystem modelling. This will permit new earth system experiments to be conducted with a more consistent representation of feedbacks involving the biosphere and chemistry than were previously possible, although technical challenges and uncertainties in the modelling remain considerable. Through a Met Office collaboration with Japanese scientists (also in association with the HiGEM project) we plan to utilise the world's most powerful computer – the Earth Simulator – to run such experiments with HadGEM1 in order to advance the frontiers of science in this field.

Acknowledgements

The code for the EVP, ridging and linear remapping schemes in the HadGEM1 sea ice model are based on the Los Alamos sea ice model (CICE) (Hunke and Lipscomb, 2004), and the code used for the river routing model is based on TRIP (Oki and Sud, 1998).

Historical and future forcing datasets for black carbon and biomass-burning aerosols were kindly provided by T. Nozawa, NIES, Japan. Anthropogenic SO_2 emissions data were kindly provided by S. J. Smith, PNNL, USA.

We acknowledge the invaluable contributions of many past and present colleagues in the development of HadGEM1, in particular all those who participated in the Tiger Teams, and also those Met Office colleagues who helped with the difficult technical work in building, testing, porting and optimising the model. We are grateful to G. Martin for providing Table 2, and to D. Sexton for Figure 31 and Table 6.

References

Aagaard, K. and E.C. Carmack, 1989, The role of sea ice and other fresh water in the Arctic circulation. J. Geophys. Res., 94, 14,485-14,498.

Andres, R. J. and A. D. Kasgnoc, 1998. A time-averaged inventory of subaerial volcanic sulfur emissions. J. Geophys. Res., 103, 25251-25261.

Baringer, M. O. and J. F. Price, 1997. Mixing and spreading of the Mediterranean outflow, J. Phys. Oceanogr. , 27, 1654-1677.

Bitz, C., M. Holland, A. Weaver and M. Eby, 2001. Simulating the ice-thickness distribution in a coupled climate model. J. Geophys. Res., 106, 2441-2463.

Bourke, R.H. and R.P. Garrett, 1987. Sea ice thickness distribution in the Arctic Ocean. Cold Regions Science and Technology, 13, 259-280.

Bryan, K., 1969. A numerical method for the study of the circulation of the world ocean., J. Comput. Phys. , 4 , 347-376.

Cess, R.D, M.H. Zhang, P.-H. Wang and B.A. Wielicki, 2001. Cloud structure anomalies over the tropical Pacific during the 1997/98 El Nino, Geophys. Res. Lett., 28 4547-4550.

Cess, R.D, R. Lu, B. Dong and G. L. Potter, 2004. The 1997/98 El Nino: A test for climate models. Intergovernmental panel on climate change (IPCC) Workshop report on Climate sensitivity.

Cox, M. D., 1984. A primitive equation, three dimensional model of the ocean, Ocean Group Technical Report 1, GFDL, Princeton.

Cox P.M., Betts R.A., Bunton C.B., Essery R.L.H., Rowntree P.R. and Smith J., 1999. The impact of new land surface physics on the GCM simulation of climate and climate sensitivity. Clim. Dyn., 15, 183-203.

Cresswell, D., 2002. Implementation of the elastic-viscous-plastic sea ice dynamics scheme. UM Document 55, Met Office.

Cubasch U., Meehl, G.A., Boer, G.J., Stouffer, R.J., Dix, M., Noda, A., Senior, C.A., Raper, S., Yap, K.S., 2001. Projections of Climate Change. In: Climate Change 2001: The Scientific Basis. Contribution of Working Group I to the Third Assessment Report of the Intergovernmental Panel on Climate Change [Houghton, J.T., Y. Ding, D.J. Griggs, M. Noguer, P.J. van der Linden, X. Dai, K. Maskell, and C.A. Johnson, (eds.)]. Cambridge University Press, Cambridge, United Kingdom and New York, NY, USA, 881pp.

Cullen M., 1993, The Unified forecast/climate model. Meteorol. Mag. 122, 81-94.

Curry, J., J. Schramm, D. Perovich and J. Pinto, 2001. Applications of SHEBA/FIRE data to evaluation of snow/ice albedo parameterizations. J. Geophys. Res., 106, 15345-15355.

Cusack, S., 2004. A revision to the background vertical mixing scheme of Peters et al. (1988), Technical report, OA Tech. Note 33.

Cusack, S., J. M. Edwards and J. M. Crowther, 1999a. Investigating k-distribution methods for parametrizing gaseous absorption in the Hadley Centre climate model. J. Geophys. Res., 104, 2051-2057.

Cusack, S., J. M. Edwards and R. Kershaw, 1999b. Estimating the subgrid variance of saturation, and its parametrization for use in a GCM cloud scheme. Q J R Meteorol Soc. 125: 3057-3076.

Davis, R. E., R. DeSzoeke, and P. Niler, 1981. Variability in the upper ocean during MILE. Part II: Modelling the mixed-layer response. Deep Sea Res., 28, 1453-1475.

Davies, T., Cullen, M.J.P., Malcolm, A.J., Mawson, M.H., Staniforth, A., White, A.A., and Wood, N., 2004. A new dynamical core for the Met Office's global and regional modelling of the atmosphere. Q. J. R. Meteorol. Soc. (submitted).

Dubal, M., Wood, N. and Staniforth, A., 2004. Analysis of parallel versus sequential splittings for time-stepping physical parameterizations. Mon. Weath. Rev., 132, 121-132.

Dukowicz, J. K. and R. D. Smith, 1994. Implicit free surface method for the Bryan-Cox-Semtner ocean model, J. Geophys. Res. , C4 , 7991-8014.

Ebert, E.E., and J.A. Curry, 1993. An intermediate one-dimensional thermodynamic sea-ice model for investigating ice-atmosphere interactions. J. Geophys. Res., 98, 10085-10109.

Edwards J M , Slingo A, 1996, Studies with a flexible new radiation code. I: choosing a configuration for a large-scale model. Q J R Meteorol Soc, 122, 689-719.

Essery, R., M. Best, R. Betts, P. Cox and R. Taylor, 2003. Explicit representation of subgrid heterogeneity in a GCM land surface scheme. J. Hydrometeorology, 4, 530-543.

Essery, R., M. Best and P. Cox, 2001. MOSES 2.2 Technical Documentation. Hadley Centre Technical Note No. 30.

ETOPO5, Global 5'x5' depth and elevation., Technical report, National Geophysical Data Center, NOAA, U. S. Dept. of Commerce, Code E/GC3, Boulder, CO 80303, USA., 1988.

Flato, G. and W. Hibler, 1995. Ridging and strength in modeling the thickness distribution of Arctic sea ice. J. Geophys. Res., 100, 18611-18626.

Fowler, C., 2003. Polar Pathfinder daily 25km EASE-Grid sea ice motion vectors. National Snow and Ice Data Center, Boulder, CO, USA.

Ganachaud, A., and C. Wunsch, 2000. Improved estimates of global ocean circulation, heat transport and mixing from hydrological data. Nature., 408, 453–457.

Gent, P. R. and J. C. McWilliams, 1990. Isopycnal mixing in ocean circulation models, J. Phys. Oceanogr. , 20 , 150-155.

Goldewijk, K. K., 2001. Estimating global land use change over the past 300 years: The HYDE database. Global Biogeochem. Cycles, 15(2): 417-433.

Gordon, C. and M. Bottomley, 1984. A scheme for incorporating the thermodynamic sea-ice model into a coupled atmosphere-ocean model. Dynamical Climatology Technical Note 1, Met Office 20.

Gordon, C., C. Cooper, C. Senior, H. Banks, J. Gregory, T. Johns, J. Mitchell and R. Wood, 2000. The simulation of SST, sea ice extents and ocean heat transports in a version of the Hadley Centre coupled model without flux adjustments. Clim. Dyn., 16, 147-168.

Grant, A.L.M. and A.R. Brown, 1999. A similarity hypothesis for shallow-cumulus transports. Q. J. Royal Meteorol. Soc., 125: 1913-1936.

Grant, A.L.M., 2001. Cloud-base fluxes in the cumulus-capped boundary layer. Q. J. Royal Meteorol. Soc., 127: 407-421.

Gregory D and Rowntree P R, 1990. A mass flux convection scheme with representation of cloud ensemble characteristics and stability dependent closure. Mon Weather Rev. 118, 1483-1506.

Gregory D and Allen S, 1991. The effect of convective scale downdrafts upon NWP and climate simulations. Ninth conference on numerical weather prediction. Denver, Colorado, Amer Met Soc, 122-123.

Gregory D, 1995. A consistent treatment of the evaporation of rain and snow for use in large-scale models. Mon. Weather Rev., 123, 2716-2732.

Gregory D, Kershaw R, Inness P M, 1997. Parametrization of momentum transport by convection. II: Tests in single-column and general circulation models. Q J R Meteorol Soc 123: 1153-1183.

Gregory D, Shutts G J and Mitchell J R, 1998. A new gravity-wave-drag scheme incorporating anisotropic orography and low-level wave breaking: Impact upon the climate of the UK Meteorological Office Unified Model. Q J R Meteorol Soc 124, 463-494.

Gregory, J. 1999. Representation of the radiative effects of convective anvils. Hadley Centre Technical Note No. 7. Available at http://www.hadleycentre.com/research/hadleycentre/pubs/HCTN/index.html

Gregory, J. M., 2000. Vertical heat transports in the ocean and their effect on time-dependent climate change, Clim. Dyn., 501-515.

Gregory J.M., Stott P.A., Cresswell D.J., Rayner N.A., Gordon C., Sexton D.M.H., 2002. Recent and future changes in Arctic sea ice simulated by the HadCM3 AOGCM. GRL, Art. No. 2175.

Griffies, S. M., A. Gnanadesikan, R. C. Pacanowski, V. D. Larichev, J. K. Dukowicz, and R. D. Smith, 1998. Isoneutral diffusion in a z-coordinate ocean model, J. Phys. Oceanogr. , 28 , 805-830.

Guest, P. and K. Davidson, 1991. The aerodynamic roughness of different types of sea ice. J. Geophys. Res., 96, 4709-4721.

Hall, M. M., and H. L. Bryden, 1982. Direct estimates and mechanisms of ocean heat transport, Deep Sea Res., 29, 339-359.

Hibler, W., 1979. A dynamical thermodynamic sea ice model. J. Phys. Oceanogr., 9, 817-846.

Hibler, W., 1980. Modeling a variable thickness sea ice cover. Mon. Wea. Rev., 108, 1943-1973.

Hunke, E. and J. Dukowicz, 1997. An elastic-viscous-plastic model for sea ice dynamics. J. Phys. Oceanogr., 27, 1849-1867.

Hunke, E. and W. Lipscomb, 2004. CICE: the Los Alamos sea ice model documentation and software user's manual. Los Alamos National Laboratory.

Jones, A., Roberts, D. L., Woodage, M. J. and Johnson, C. E., 2001. Indirect sulphate aerosol forcing in a climate model with an interactive sulphur cycle. J. Geophys. Res., 106, 20293-20310

Jones, A. and Roberts, D. L., 2004. An interactive DMS emissions scheme for the Unified Model. Hadley Centre Technical Note No.47, Met Office, Exeter. Available at http://www.hadleycentre.com/research/hadleycentre/pubs/HCTN/index.html

Kettle A.J., Andreae M.O., Amouroux D., Andreae T.W., Bates T.S., Berresheim H., Bingemer H., Boniforti R., Curran M.A.J., DiTullio G.R., Helas G., Jones G.B., Keller M.D., Kiene R.P., Leck C., Levasseur M., Malin G., Maspero M., Matrai P., McTaggart A.R., Mihalopoulos N., Nguyen B.C., Novo A., Putaud J.P., Rapsomanikis S., Roberts G., Schebeske G., Sharma S., Simo R., Staubes R., Turner S., and Uher G., 1999. A global database of sea-surface dimethylsulfide (DMS) measurements and a procedure to predict sea surface DMS as a function of latitude, longitude and month. Global Biogeochem. Cycles, 13, 399-444.

Kiehl, J.T., Schneider, T.L., Poltmann, R.W., and Soloman, S., 1999. Climate forcing due to tropospheric and stratospheric ozone. J. Geophys. Res., 104, 31239-31254.

Kraus, E. B. and J. S. Turner, 1967. A one dimensional model of the seasonal thermocline. Part II, Tellus , 19 , 98-105.

Large, W. G., J. C. McWilliams, and S. C. Doney, 1994. Ocean vertical mixing: A review and a nonlocal boundary layer parameterization., rev. Geophys. , 32 , 363-403.

Lawrence, D.M. and Slingo, J.M., 2004. An annual cycle of vegetation in a GCM. Part I: Implementation and impact on evaporation. Clim. Dyn. 22: 87-106

Levitus S., T. P. Boyer, M. E. Conkright, T. Orian, J. Antonov, C.Stephens, L. Stathoplos, D. Johnson, and R. Gelfeld, 1998. World Ocean Database 1998. Number 18 in NOAA Atlas NESDIS. US Department of Commerce.

Lipscomb, W., 2001. Remapping the thickness distribution in sea ice models. J. Geophys. Res., 106, 13989-14000.

Lock, A.P., A.R. Brown, M.R. Bush, G.M. Martin and R.N.B. Smith, 2000. A new boundary layer mixing scheme. Part I: Scheme description and SCM tests. Mon. Weath. Rev., 128: 3187-3199.

Macdonald, A. M., and C. Wunsch, 1996. An estimate of global ocean circulation and heat fluxes. Nature., 382, 436–439.

Martin, G. M., Dearden, C., Greeves, C., Hinton, T., Inness, P., James, P., Pope, V.D., Ringer, M.A., Stratton, R.A., and Yang, G. Y., 2004. Evaluation of the atmospheric performance of HadGAM/GEM1. Hadley Centre Technical Note No. 54, Met Office, Exeter, UK. On-line at http://www.hadleycentre.com/research/hadleycentre/pubs/HCTN/index.html.

Maykut, G. and M. McPhee, 1995. Solar heating of the Arctic mixed layer. J. Geophys. Res., 100, 24691-24703.

McPhee, M., 1992. Turbulent heat flux in the upper ocean under sea ice. J. Geophys. Res., 97, 5365-5379.

Murphy, J. M., D. M. H. Sexton, D. N. Barnett, G. S. Jones, M. J. Webb, M. Collins, and D. A. Stainforth, 2004. Quantification of modelling uncertainties in a large ensemble of climate change simulations. Nature, 430, 768-772.

Oki, T. and Y. C. Sud, 1998: Design of Total Runoff Integrating Pathways (TRIP) - A global river channel network. Earth Interactions, 2.

Pacanowski, R. C. and S. M. Griffies, 1998. MOM 3.0 Manual, NOAA/Geophysical Fluid Dynamics Laboratory, Princeton, USA 08542.

Peters, H., M. C. Gregg, and J. M. Toole, 1988. On the parameterization of equatorial turbulence, J. Geophys. Res. , 93 , 1199-1218.

Pope VD, Gallani ML, Rowntree PR and Stratton RA, 2000. The impact of new physical parametrizations in the Hadley Centre climate model: HadAM3. Clim Dyn 16: 123-146.

Rahmstorf, S., 1993. A fast and complete convection scheme for ocean models. Ocean Modelling, 101, 9-11.

Randel, W.J. and Wu, F., 1999. A stratospheric ozone trends dataset for global modeling studies. Geophys. Res. Lett., 26, 3089-3092.

Randel, W.J. Stolarski, R.S., Cunnold, D.M., Logan, J.A., Newchurch, M.J., and Zawodny, J.M., 1999. Atmosphere-Trends in the vertical distribution of ozone. Science, 285, 1689-1692.

Rayner, N., D. Parker, E. Horton, C. Folland, L. Alexander, D. Rowell, E. Kent and A. Kaplan, 2003. Global analyses of sea surface temperature, sea ice, and night marine air temperature since the late nineteenth century. J. Geophys. Res., 108, 4407, doi:10.1029/2002JD002670.

Rickard, G. J. , 2004. Ocean models and the implementation of vertical diffusion and vertical mixing, Technical report, Unified Model Documentation Paper UMDP59, Met Office.

Roberts, D. L. and Jones, A., 2004. Climate sensitivity to black carbon aerosol from fossil fuel combustion. J. Geophys. Res., 109, doi: 10.1029/2004JD004676.

Roberts, M.J., 2004. The ocean component of HadGEM1. GMR Report Annex IV.D.3, Met Office.

Roberts, M.J., H. Banks, N. Gedney, J. Gregory, R. Hill, S. Mullerworth, A. Pardaens, G. Rickard, R. Thorpe and R. Wood, 2004. Impact of an eddy permitting ocean resolution on control and climate change simulations with a global coupled GCM, J. Climate 17, 3-20.

Roberts, M. J., 2004a. The Gent and McWilliams parameterisation scheme, including Visbeck and biharmonic GM schemes, Technical report, Unified Model Documentation Paper UMDP54, Met Office.

Roberts, M. J., 2004b. Isopycnal diffusion schemes, Technical report, Unified Model Documentation Paper UMDP51, Met Office.

Roberts, M. J. and D. Marshall, 1998. Do we require adiabatic dissipation schemes in eddy-resolving ocean models? J. Phys. Oceanog. , 28 , 2050-2063.

Roberts, M. J. and G. J. Rickard, 2004. Ocean model free surface, Technical report, Unfied Model Documentation Paper UMDP62.

Roether, W., V. M. Roussenov and R. Well, 1994. A tracer study of thethermohaline circulation of the eastern Mediterranean. In: Malanotte-Rizzoli P, Robinson AR (eds) Ocean processes in climate dynamics: global and Mediterranean example. Kluwer Academic Press, Dordrecht, pp 371-394.

Rothrock, D., 1975. The energetics of the plastic deformation of pack ice by ridging. J. Geophys. Res., 80, 4514-4519.

Sato, M., J.E. Hansen, M.P. McCormick, and J.B.Pollack, 1993. Stratospheric aerosol optical depth, 1850-1990. J. Geophys. Res. 98, 22987-22994.

Semtner, A., 1976. A model for the thermodynamic growth of sea ice in numerical investigations of climate. J. Phys. Oceanogr., 6, 379-389.

Semtner, A., 1987. A numerical study of sea ice and ocean circulation in the Arctic. J. Phys. Oceanogr., 17, 1077-1099.

Senior C and Mitchell J F B, 1993. CO2 and climate: The impact of cloud parametrization. J. Clim. 6: 393-418.

Shirasawa, K. and R. Ingram, 1991. Characteristics of the turbulent oceanic boundary layer under sea ice. Part 1: A review of the ice-ocean boundary layer. J. Mar. Syst., 2, 153-160.

Smith R N B, 1990. A scheme for predicting layer clouds and their water content in a general circulation model. Q J R Meteorol Soc 116: 435-460.

Smith R N B, 1993. Experience and developments with the layer cloud and boundary layer mixing schemes in the UK Meteorological Office Unified Model. In Proceedings of the ECMWF/GCSS workshop on parametrization of the cloud-topped boundary layer, 8-11 June 1993, ECMWF, Reading, England.

Smith, R.N.B., Gregory, D., Wilson, C.A., Bushell, A.C. and Cusack, S. 1999. Calculation of saturated specific humidity and large-scale cloud. UM Documentation Paper No. 29.

Smith, W. H. F. and D. Sandwell, 1997. Global seafloor topography from satellite altimetry and ship depth soundings, Science , 277 , 1956-1962.

Solanki, S.K. and Krivova, N. A., 2003. Can solar variability explain global warming since 1970? J. Geophys. Res., 108(A5), 1200, doi:10.1029/2002JA009753.

Spencer, H., R. T. Sutton, J. M. Slingo, M. Roberts and E. Black, 2004. Indian Ocean climate and dipole variability in Hadley Centre coupled GCMs. Submitted to J. Clim.

Staniforth, A., A. White, N.Wood, J. Thuburn, M.Zerroukat and E. Cordero, 2003. Unified Model Documentation Paper No 15: Joy of UM5.4 – Model Formulation. Available at http://www.metoffice.com/research/nwp/publications/papers/unified_model/index.html.

Thorndike, A., D. Rothrock, G. Maykut and R. Colony, 1975. The thickness distribution of sea ice. J. Geophys. Res., 80, 4501-4513.

Turner, A. G., P. M. Inness and J. M. Slingo, 2004. The Role of the Basic State in Monsoon Prediction. Q. J. R. Meteorol. Soc., accepted.

UNESCO, 1981. Tenth report of the joint panel on oceanographic tables and standards, Technical Papers in Marine Sci 36, UNESCO, Paris.

Visbeck, M., J. Marshall, T. Haine, and M. Spall, 1997. On the specification of eddy transfer coefficients in coarse resolution ocean circulation models., J. Phys. Oceanogr. , 27, 381-402.

Warn-Varnas, A. C., G. M. Dawson and P. J. Martin, 1981. Forecast and studies of the oceanic mixed layer during the MILE Experiment. Geophys. Astrophys. Fluid Dyn., 17, 63-85.

Webb, M., Senior, C., Bony, S., and Morcrette, J.-J., 2001. Combining ERBE and ISCCP data to assess clouds in the Hadley Centre, ECMWF and LMD atmospheric climate models. Clim. Dyn. 17: 905-922.

Webster, S., Brown, A.R., Cameron, D.R., Jones, C.P., 2003. Improvements to the representation of orography in the Met Office Unified Model. Q. J. Royal Meteorol. Soc. 129: 1989-2010

Whitworth, T., W. D. Nowlin, and S. J. Worley, 1982. The net transport of the Antarctic Circumpolar Current through Drake Passage, J. Phys. Oceanogr. ,12, 960-971.

Wijffels, S. E., N. Bray, S. Hautala, G. Meyers, and W. M. L. Morawitz, 1996. The WOCE Indonesian Throughflow repeat hydrography sections: I10 and IR6. Int. WOCE Newsl., 24, 25-28.

Wilson, D.R. and S.P. Ballard, 1999. A microphysically based precipitation scheme for the Meteorological Office Unified Model. Quart. J. Royal Meteorol. Soc., 125 1607-1636.

Woodage, M., Davison, P. and Roberts, D. L., 2003. Aerosol processes. Unified Model documentation paper No. 20.

Zhang, Y-C., W. B. Rossow, A. A. Lacis, V. Oinas and M. I. Mishchenko, 2004. Calculation of radiative flux profiles from the surface to top-of-atmosphere based on ISCCP and other global datasets: Refinements of the radiative transfer model and the input data. J. Geophys. Res. (submitted).

Appendix A: Description of the sea ice component of HadGEM1

A.1 The sea ice sub-model

The sea ice model solves for the evolution of the ice thickness distribution (ITD) in time and space. The evolution is determined by advection, thermodynamic growth or melt and mechanical distribution (e.g. ridging), which is expressed as

$$\frac{\partial g}{\partial t} = -\nabla \cdot (g\mathbf{u}) - \frac{\partial}{\partial h}(fg) + \psi \qquad \text{(A.1)}$$

(Thorndike *et al.* ,1975) where g is the ice thickness distribution function, $\mathbf{u}$ is the horizontal velocity, $\nabla = \left(\frac{\partial}{\partial x}, \frac{\partial}{\partial y} \right)$, f is the thermodynamic ice growth rate and ψ is the ridging redistribution function. $g(\mathbf{x}, h, t)dh$ is defined as the fractional area of ice in the thickness range $(h, h + dh)$ at a given time and location.

The ITD is modelled by dividing the ice pack at each grid point into a number of discrete thickness categories. HadGEM1 uses 5 ice categories and 1 open water category, which is sufficient for climate modeling (Bitz et al., 2001). The categories are bound by higher and lower limits which are shown in Table A1. The boundaries are defined to give higher resolution for thin ice. The thickest category has no upper limit.

Category	Lower limit	Upper limit
1	0	0.6
2	0.6	1.4
3	1.4	2.5
4	2.5	4.6
5	4.6	-

Table A1: Ice category thickness limits (in metres, to 1 d.p.)

The remainder of this report details the atmosphere and ocean components of the sea ice model. The sea ice parameters used in HadGEM1 are documented in the appendix.

A.2 The atmosphere component

A.2.1 State variables

The sea ice state variables in the atmosphere component are:

- the fractional ice areas or concentrations for each ice category and the open water category
- the equivalent ice depth (h_e) for each ice category as defined as

$$h_e = h_i + \frac{\kappa_i}{\kappa_s} h_s \qquad (2)$$

where h_i is the ice thickness, h_s is the snow thickness, and κ_i and κ_s are the thermal conductivities of ice and snow respectively

- the snow thickness for each category in units of water equivalent (kg m^{-2})
- the surface temperature (T) for each category.

A.2.2 Albedo

The sea ice albedo parameterization in HadGEM1 is designed to capture the albedo annual cycle, with the albedo rapidly declining in the summer when surface melting of the snow commences. Once the snow has melted, the bare ice (albedo ~ 0.6) develops lower albedo (~0.25) melt ponds, which cover some 15-45% of the ice surface. This provides an albedo feedback increasing the rate of surface melt. The ponds refreeze once the temperature falls in the autumn. Fresh snow cover restores the albedo back to a constant value.

In the model, ice albedo is a combination of the bare ice albedo and that of the overlying snow cover, if snow is present. Both components are functions of the surface temperature. The albedo is calculated for the average ice properties (not per category), therefore the surface temperature averaged over all the categories (the aggregate temperature, T^{agg}) is used.

A.2.2.1 Bare ice albedo

When the ice is close to melting, the albedo is reduced to account for melt ponds. In the model, the surface temperature is constrained never to rise above the melting temperature (T_{melt}), so a parameter ($\Delta T_{icemelt}$) is used to determine whether the albedo should be decreased due to ponding. The ice albedo (α_i^*) is calculated using

$$\alpha_i^* = \begin{cases} \alpha_{bare}, & \text{if } T^{agg} < T_{melt} - \Delta T_{icemelt} \\ \alpha_{bare} - (T_{melt} - T^{agg})\Delta\alpha, & \text{if } T^{agg} \geq T_{melt} - \Delta T_{icemelt} \end{cases} \qquad (3)$$

where α_{bare} is the bare ice albedo (with no ponding) and $\Delta\alpha$ is a parameter determining the decrease in ice albedo due to melt.

An adjustment is then made to compensate for the zero-layer structure of the ice model (which is described in section 4.4). In reality, a fraction of the incident light (f) passes through the ice rather than be used to warm the surface layer. Some of this light (β), is back-scattered by inclusions in the ice centre. Semtner (1987) suggested factoring in an additional component of the surface albedo, to improve the lag in surface heating which would otherwise lead to a too early onset of ponding in the zero-layer model. Hence, the final ice albedo (α_i) is given by,

$$\alpha_i = \alpha_i^* + \beta(1-\alpha_i^*)\, f \,. \qquad (4)$$

A.2.2.2 Snow albedo

The snow albedo (α_s) is given by

$$\alpha_s = \begin{cases} \alpha_{cold}, & \text{if } T^{agg} < T_{melt} - \Delta T_{snowmelt} \\ \alpha_{melt} + \dfrac{(T_{melt} - T^{agg})(\alpha_{cold} - \alpha_{melt})}{\Delta T_{snowmelt}}, & \text{if } T^{agg} \geq T_{melt} - \Delta T_{snowmelt} \end{cases} \qquad (5)$$

where α_{cold} and α_{melt} are the albedos of cold and melting snow respectively, and $\Delta T_{snowmelt}$ is the temperature range which determines melting. A reduction in $\Delta T_{snowmelt}$ will delay the onset of summer melt pond formation, as it will take longer for the snow to melt.

A.2.2.3 Final sea ice albedo

The final sea ice albedo (α) adjusts the bare ice albedo for the aggregate snow depth (h_s^{agg}),

$$\alpha = \alpha_i + (\alpha_s - \alpha_i)(1 - \exp(-d_{mask} h_s^{agg})) . \qquad (6)$$

Surface snow cover will only partially obscure the underlying albedo due to snow drifting. Therefore, a masking depth (d_{mask}) is used to reduce the snow depth used to calculate the albedo.

A.2.3 Radiative and turbulent fluxes

The radiative and turbulent fluxes are calculated separately for the portions of a grid box covered by ice and leads. Grid box mean fluxes are then calculated by weighting the fluxes by the ice and leads fractions. The exception is the calculation of the radiative flux caused by multiple reflections between the snow/ice surface and the base of clouds visible from the surface, which uses the grid box mean albedo. The multiple ice category scheme does not impact on the surface flux calculations. In the boundary layer scheme, the grid box mean calculations use the aggregate ice temperature to evaluate the surface temperature associated fluxes.

A.2.4 Ice heat fluxes and ice temperature

The zero-layer thermodynamics model of Semtner (1976) is used in HadGEM1. The temperature gradient through the snow and ice is assumed to be piecewise linear, with a change of gradient at the ice/snow interface (because of the lower thermal conductivity of snow). The temperature of the lower surface of ice must be the freezing temperature of sea water (T_f ,which is set to a constant -1.8°C).

The governing equation for the surface temperature for each category is,

$$c_{s*} \frac{dT}{dt} = F_a - F_{botmelt} \qquad (7)$$

where c_{s*} is an effective surface heat capacity and F_a is the new downward atmosphere heat flux at the ice (or snow) surface. $F_{botmelt}$ is the downward diffusive heat flux through the ice and snow for each category, defined as,

$$F_{botmelt} = \kappa_i \frac{(T - T_f)}{h_e}. \qquad (8)$$

The surface heat capacity term in equation (7) is not part of Semtner's zero layer model, which neglects the heat storage in the ice. This term was introduced to the Unified Model to improve the simulation of the surface temperature diurnal cycle (Gordon and Bottomley, 1984).

The freezing temperature of the surface of ice (or snow, if present) is taken to be the freezing point of fresh water (0°C). The surface is taken to be fresh for two reasons. Firstly, the snow falling on the ice will be fresh. Secondly, the salt within the ice gradually percolates downwards, so that the upper ice surface also has a low salinity. When the surface temperature rises above the freezing point, the temperature is held at 0°C, and the excess heat flux for each category ($F_{topmelt}$) is stored and used by the ocean model to melt the surface snow and ice.

A.2.5 Coupling to ocean

The ice diffusive heat flux and the ice surface heat flux due to melting (for each category) are averaged over the atmosphere day, and these daily mean fields are passed to the ocean via the coupler. Similarly, the daily mean snowfall and sublimation rates (which are not category dependent) are also passed into the coupler. The fluxes are transferred as grid box mean values to conserve energy. So for example, the ice diffusive heat flux is multiplied by the fractional ice area to compute the grid box mean value.

Within the coupler, the fluxes are transferred on to the ocean grid. Within the ocean model, the grid box mean ice fluxes are converted back to local fluxes (i.e. per unit ice area) by dividing them by the fractional ice area.

A.3 The ocean component

A.3.1 State variables

The sea ice state variables in the ocean component are:

- the fractional ice areas or concentrations for each ice category and the open water category
- the ice volume per unit area or grid box mean ice thickness for each ice category; this is equal to the product of the local ice thickness and ice concentration
- the snow volume per unit area or grid box mean snow thickness for each ice category (in metres); this is equal to the product of the local snow thickness and ice concentration).

A.3.2 Solving the ice thickness distribution evolution equation

The ocean component solves for the evolution of the ice thickness distribution (ITD) in time and space as expressed in equation (1). The ITD equation is solved in the following order. First, the ice velocities are computed and then the ice is advected. The next process is ice ridging, followed by the ice thermodynamics. Each of these processes are next discussed in turn.

A.3.3 Dynamics

A.3.3.1 Ice velocities

The elastic-viscous-plastic (EVP) dynamical model of Hunke and Dukowicz (1997) is used to determine the ice velocities. The model is based on the standard viscous-plastic (VP) model for sea ice dynamics (Hibler, 1979). At timescales associated with the wind forcing, the EVP model reduces to the VP model. But at shorter timescales, the adjustment process occurs by a numerically more efficient elastic wave mechanism. This allows a fully explicit numerical scheme, which improves the model's computational efficiency.

The ice momentum equation used in HadGEM1 is

$$m\frac{\partial \mathbf{u}}{\partial t} = a\boldsymbol{\tau}_{\mathbf{a}} + a\boldsymbol{\tau}_{w} + \hat{k} \times mf\mathbf{u} + \nabla \cdot \sigma \qquad (9)$$

where m is the combined mass of ice and snow per unit grid box area, a is the total ice concentration, $\boldsymbol{\tau}_{\mathbf{a}}$ and $\boldsymbol{\tau}_{w}$ are the grid box mean wind and ocean stresses, f is the Coriolis parameter, and $\nabla \cdot \sigma$ represents the internal forces exerted by the ice. The momentum equation is solved together with an equation for the ice internal stress, which relates the ice stress to the strain rates using EVP rheology. The EVP code is based in the Los Alamos Laboratory CICE model (Hunke and Lipscomb, 2004).

The ice strength (P) is parameterized following Hibler (1979) as

$$P = p^{*} h_i e^{-c^{*}(1-a)} \qquad (10)$$

where p^* and c^* are the rheological parameters which set the maximum compressive strength (per unit thickness) of ice and the rate at which the ice strength decreases with decreasing concentration, respectively. The ice strength parameterization differs from the parameterization used in the CICE model. This is because we were unable to use the more physically based Rothrock (1975) ice strength parameterization due to numerical instability problems around the North Pole. The ice strength is smoothed in the longitudinal direction in the two rows next to the North Pole as a safety precaution against instability in the ice in this region.

A.3.3.2 Ice velocity filtering

The ice velocities in the Arctic are filtered, using the same filtering scheme as used in the ocean. This filtering removes noise in the velocity fields, which can lead to excessive ridging and a build up of ice at the North Pole.

The noisy velocity fields are due to residual elastic waves remaining in the EVP final solution as the latitudinal resolution increases towards the pole. The noise could also be removed by reducing the EVP subtimestep, but this can be computationally expensive and filtering offers a cheaper but less accurate solution.

A.3.3.3 Advection

The ice is advected using an upwind advection scheme as in HadCM3. The ice concentration, ice thickness and snow thickness for each category are advected. There is an additional scheme in HadGEM1 which allows ice to be advected across the North Polar island (which exists in the ocean model to avoid the polar singularity in the spherical co-ordinate system). The scheme is based on the atmosphere model and is documented in Cresswell (2002).

A.3.4 Ridging

The mechanical redistribution (or ridging) scheme in HadGEM1 is that of the CICE model (Hunke and Lipscomb, 2004). The scheme is based on work by Thorndike et al. (1975), Hibler (1980) and Flato and Hibler (1995). The ridging process converts thinner ice to thicker ice and creates open water. The scheme ensures that the ice area never exceeds the grid cell area when ice is converging.

The CICE ridging scheme has the following key components:

- a participation function which specifies the distribution of ice deformed by ridging following Thorndike et al. (1975). The function favours the ridging of thin ice and closing of open water over the ridging of thicker ice.
- a redistribution scheme which determines the distribution of ridged ice. Following Hibler (1980), the ridged ice has a uniform distribution between twice the thickness of the ridging ice and a specified maximum thickness.
- an expression for deriving the area of ice ridging, along with leads opening and closing, based on the strain rates in the grid cell. The equation of Flato and Hibler (1995) is used, in which divergence increases the open water area; convergence removes open water and creates ridges; and shear acts as a combination of divergence and convergence.

Snow volume is moved between categories in the same way as ice during ridging, except that a fraction of snow is allowed to fall into the ocean instead of being added to the new ridge.

A.3.5 Thermodynamics

A.3.5.1 Growth/melt rates

The rate at which the local snow thickness changes due to thermodynamics for each category is determined by,

$$\rho_s \frac{dh_s}{dt} = S_{fall} - S_{sub} - \frac{F_{topmelt}}{L} \qquad (11)$$

where ρ_s is the density of snow, S_{fall} is the snowfall rate, S_{sub} is the sublimation rate, $F_{topmelt}$ is the category surface melting heat flux and L is the latent heat of freezing water. Any surplus heat (F_{excess}) due to the snow completely melting in a particular category is used to melt ice in that category.

The rate of local ice thickness growth for each category is given by,

$$L\rho_i \frac{dh_i}{dt} = -F_{excess} - F_{botmelt} - F_{o-i} \qquad (12)$$

where ρ_i is the ice density and $F_{botmelt}$ is the category diffusive heat flux through the snow and ice.

F_{o-i} is the ocean to ice heat flux which is parameterized following McPhee (1992) as

$$F_{o-i} = \rho_w c_w c_h u_* (T_w - T_f) \qquad (13)$$

where ρ_w is the seawater density, c_w is the specific heat of seawater, c_h is the heat transfer coefficient, $u_* = \sqrt{|\boldsymbol{\tau}_w| / \rho_w}$ is the friction velocity and T_w is the sea surface temperature. A minimum u_* value is specified to maintain an ocean to ice heat flux even when the ocean and ice velocities are very similar.

In the marginal ice zone, the ocean to ice heat flux is increased in a crude attempt to capture the effect of enhanced lateral melting and waves washing water over the ice. When the ice concentration drops below a specified value (a_{mizfry}), the ocean to ice heat flux becomes,

$$F_{o-i} = \rho_w c_w c_h u_* (T_w - T_f) \frac{a_{mizfry}}{a}. \qquad (14)$$

In the ocean model, if the sea surface temperature drops below the freezing point, the temperature is reset to T_f , and the implied heat flux ($F_{caryheat}$) is used to grow new sea ice. The new ice is grown in the leads fraction to a specified minimum thickness and is added to the first category. If however, there are no leads, or there is more new ice than will fit into the first category, the new ice is spread uniformly over all the categories.

A.3.5.2 Linear remapping scheme

Thermodynamic growth and melt can be viewed as ice transport in thickness space. Once the growth rates of ice and snow for each category have been calculated, it is necessary to calculate how much ice must move between categories. This represents the 2nd term on the right hand side of equation (1).

HadGEM1 uses the remapping scheme of Lipscomb (2001). In this scheme, the thickness categories are represented as Lagrangian grid cells, whose boundaries are projected forward

in time using the calculated growth rates. The thickness distribution is assumed to be linear in each displaced category, and ice area and volume are transferred between categories so that the original boundaries can be restored. Snow volume is transferred in proportion to the ice volume transfers.

A.3.5.3 White ice formation

White ice forms at the snow/ice interface when the weight of snow on top of the ice is sufficient to push the interface under water. Water then enters the snow and tends to freeze creating white ice. This process is included in HadGEM1. The snow/ice interface will coincide with the water surface when

$$\rho_i h_i + \rho_s h_s = \rho_w h_i \qquad (15)$$

(from Archimedes' principle). Thus, white ice is created when

$$h^* \equiv h_s - \frac{(\rho_w - \rho_i)h_i}{\rho_s} > 0 \qquad (16)$$

and sufficient snow is converted into ice such that $h^* = 0$.

A.3.5.4 Salinity and freshwater fluxes

The growth and melt of snow and ice create fluxes of salt and freshwater in and out of the ocean. In HadGEM1, a freshwater flux is passed from the ice to the ocean for use in the ocean's free surface calculation. Additionally, an ice-ocean salinity flux is also passed to the ocean, which combines both the salt and freshwater changes associated with the changing snow and ice volumes. This salinity flux is used in the ocean to update the sea surface salinity.

A.3.5.5 Minimum ice values

Minimum ice concentration values are set for each category. If the ice concentration drops below these values, the ice is removed and the associated energy, freshwater and salt are passed to the ocean. There is a minimum ice thickness for the thinnest ice category, to keep the thermodynamics stable. If the thickness goes below this value, the ice is reshaped (i.e. the concentration reduced, while maintaining the ice volume) so that the thickness equals the minimum thickness value.

A.3.6 Coupling to atmosphere

At the end of an ocean day, the grid box mean ice and snow thicknesses and ice concentration for all categories are passed into the coupler. After the fields have been transferred to the atmosphere grid, the effective ice thickness (as defined in section 4.1) is calculated ready for use in the atmosphere model. The aggregate (summed over all categories) ice quantities are also computed in the coupler and passed to the atmosphere model.

A.4 Initial conditions

The ice concentration and ice thickness are initialized using different methods in each hemisphere for the starting month of September. In the northern hemisphere, the total ice volume in each grid box is based on the Hadley Centre Global Sea Ice and Sea Surface Temperature (HadISST) climatology (Rayner et al., 2003) and ice thickness data provided by M. Serreze (2000, personal communication). The ice volume is distributed between the 5 ice categories, by specifying the maximum ice concentration in each category. h_i for each category is set to be the mid-point between the lower and upper category bounds.

In the southern hemisphere, the ice concentration and thickness are taken from HadCM3 due to a lack of thickness observations in this region. The ice is not distributed between categories. Instead it is all placed in the appropriate thickness category, because the ice is mainly in the first two categories in the Antarctic.

The ice is initialized with no snow on top and starts at rest. The ice surface temperature is set to HadCM3 values.

Table A2 : Sea ice parameter values used in HadGEM1

Parameter definition	Parameter value	Comments
Albedo of bare ice (α_{bare})	0.57	Ranges from 0.5 for first year ice and 0.61 for multi year ice (Curry et al., 2001)
Temperature range to determine ice melting in albedo calculation ($\Delta T_{icemelt}$)	1.0 K	Curry et al., 2001
Change in ice albedo due to melt ($\Delta\alpha$)	-0.075	Curry et al., 2001
Fraction of penetrating incident light used in albedo calculation (f)	0.17	Ranges from 0.1 for first year ice and 0.2 for multi year ice (Semtner, 1987)
Back-scattered light fraction using in albedo calculation (β)	0.4	Ranges from 0.3 for first year ice and 0.6 for multi year ice (Semtner, 1987)
Albedo of melting deep snow on sea ice (α_{melt})	0.65	Ranges from 0.65 to 0.77 (Curry et al., 2001)
Albedo of cold deep snow on sea ice (α_{cold})	0.8	Ranges from 0.78 to 0.85 (Curry et al., 2001)
Temperature range to determine snow melting in albedo calculation ($\Delta T_{snowmelt}$)	2 K	Ranges from 0.3 to 2 (Curry et al., 2001)
Snow masking depth used in albedo calculation (d_{mask})	0.2 m^2 kg^{-1}	This results in half surface cover with 3 mm of snow. This value is also used for snow on land. (Semtner, 1987)
Reciprocal of effective surface heat capacity ($1/c_{s*}$)	4.8 x 10^{-6} K m^2 J^{-1}	Corresponds to the heat capacity of a depth of ice proportional to the e-folding depth of the diurnal temperature wave (about 20cm)
Sea ice roughness length	0.5 mm	Ranges from <0.01 to 110mm for different sea ice types (Guest and Davidson, 1991). This value is typical for very smooth ice.
Thermal conductivity of ice	2.09 W m^{-1} K^{-1}	
Thermal conductivity of snow	0.32 W m^{-1} K^{-1}	
Density of sea ice	900 kg m^{-3}	
Density of snow	300 kg m^{-3}	
Density of seawater	1026 kg m^{-3}	
McPhee ocean-ice heat transfer coefficient	0.006	McPhee (1992), Maykut and McPhee (1995)
McPhee ocean-ice heat transfer minimum friction velocity	0.005 m s^{-1}	Same as CICE model
Marginal ice concentration for ocean-ice heat flux (a_{mizfry})	0.05	Same as HadCM4
Salinity of sea ice	6 psu	

Minimum ice depth of 1st category	0.01 m	Same as CICE model
Number of sea ice categories	5	Sufficient for climate models (Bitz et al, 2001)
Minimum local ice depth of newly formed frazil ice	0.05 m	Same as CICE model
Minimum local snow depth	$1x10^{-5}$ m	Same as CICE model
Minimum ice category concentration	$5x10^{-6}$ ($1x10^{-6}$ for leads fraction)	Same as CICE model
Ice strength, p*	20,000 N m^{-2}	Values in literature vary from 5000 N m^{-2} to 27,500 N m^{-2}
Ice strength, c*	20	Used by Hibler (1979)
Ratio of shear strength to compressive strength	2	Hunke and Dukowicz (1997)
EVP subcycling timestep	30 s	
Elastic damping timescale as fraction of forcing step	0.3	
Ice-ocean drag coefficient	$15x10^{-3}$	Values range from $1x10^{-3}$ to $35x10^{-3}$ (Shirasawa and Ingram, 1991)
Thinnest percentage of ice that ridges	0.15	Value suggested by Thorndike et al. (1975)
Factor determining the mean thickness of ice ridges	100 m	Value used by Flato and Hibler (1995), based on first year ridge measurements. This implies that the ridge peak thickness is 20 times the square root of the ridging ice thickness.
Fraction of shear energy contributing to ridging (c_s)	0.5	$0 < c_s < 1$. Current observations are insufficient to determine best value. See discussion in Flato and Hibler (1995).
Fraction of snow that survives ridging	0.05	Same as CICE model